

## Abstract

# Atom Interferometer-Based Gravity Gradiometer Measurements

Jeffrey B. Fixler

2003

A cold source, Cesium atomic fountain instrument was constructed to measure gravitational gradients based on atomic interference techniques. Our instrument is one of the first gradiometers that is absolute. The defining ruler in our apparatus is the wavelength of the cesium ground-state hyperfine splitting, which has an accuracy of  $\leq 1$  part per thousand determined by the oscillators used in our clocks. The gradiometer is based on the light pulse atom interferometer technique employing a  $\pi/2 - \pi - \pi/2$  pulse sequence on two identical ensembles of cesium atoms. We have achieved a differential acceleration sensitivity of  $4 \times 10^{-9} \text{g}/\sqrt{\text{Hz}}$  with an accuracy of  $\leq 1 \times 10^{-9} \text{g}$  in a vertical gravity gradiometer configuration. A detection system was implemented to suppress sensitivity to laser amplitude and frequency noise. Immunity to vibration-induced acceleration noise was implemented with a data analysis technique not requiring the use of an active vibration isolation system. The gravity gradiometer was characterized against systematic environmental effects including reference platform tilt and vibration.

The accuracy of the gradiometer was characterized through a measurement of the Newtonian gravitational constant,  $G$ . The change in the gravitational field along one dimension was measured when a well-characterized lead, Pb, mass is displaced. A value of  $G = (6.693 \pm 0.027 \pm 0.021) \times 10^{-11} \text{ m}^3/(\text{kg} \cdot \text{s}^2)$  is reported with the two errors representing statistics and systematics, respectively. The experiment introduces a new class of precision measurement experiments to determine  $G$  through the

quantum mechanical description of atom-photon interactions, vastly different from existing methods with their unresolved systematics. Straightforward enhancements to our technique could lead to an absolute uncertainty in  $G$  that reaches or exceeds that of the best current measurements.

As a proof of principle we performed a demonstration of an atom interferometer based horizontal gravity gradiometer measuring the  $T_{z,x}$  component of the gravitational gradient tensor was performed. The horizontal configuration is maximally sensitive to angular accelerations of the platform. A proof of principle angular acceleration sensitivity of  $2 \times 10^{-6} \frac{rad}{s} / \sqrt{Hz}$  is observed for a  $T = 15ms$  interferometer time. A  $T_{z,x}$  has the potential to aid in inertial navigation, especially on the long term time scale where the atomic gyroscope suffers from drift.

# Atom Interferometer-Based Gravity Gradiometer Measurements

A Dissertation  
Presented to the Faculty of the Graduate School  
of  
Yale University  
in Candidacy for the Degree of  
Doctor of Philosophy

by  
Jeffrey B. Fixler

Dissertation Director: Mark A. Kasevich

December 2003

Copyright © 2003 by Jeffrey B. Fixler

All rights reserved.

# Contents

<b>Acknowledgements</b>	<b>ix</b>
<b>1 Introduction</b>	<b>1</b>
1.1 Gravity Gradiometry . . . . .	1
1.1.1 Accelerometers and Gradiometers . . . . .	2
1.1.2 Light Pulse Matter Wave Interferometry . . . . .	4
<b>2 Gravity Gradiometry</b>	<b>6</b>
2.1 Gravity Gradients . . . . .	6
2.2 Applications . . . . .	8
2.2.1 Inertial Navigation . . . . .	8
2.2.2 Covert Navigation . . . . .	9
2.2.3 Resource Exploration . . . . .	9
2.2.4 Newton's Constant . . . . .	10
2.3 Instrumentation . . . . .	11
<b>3 Laser Cooling and Trapping</b>	<b>14</b>
3.1 Atomic structure . . . . .	14
3.2 Two-Level Atoms . . . . .	15
3.3 Laser Cooling and Trapping . . . . .	18

3.3.1	Doppler Cooling . . . . .	18
3.3.2	Polarization Gradient Cooling . . . . .	19
3.4	Magneto Optical Trapping . . . . .	20
3.4.1	Atomic Fountains . . . . .	21
3.5	Velocity Selective Cooling . . . . .	23
3.6	Detection . . . . .	25
<b>4</b>	<b>Atom Interferometry</b>	<b>27</b>
4.1	Introduction . . . . .	27
4.2	Classical Analogy . . . . .	27
4.3	Interferometer . . . . .	29
4.4	Path Integral Approach . . . . .	31
4.4.1	Quantum Propagator . . . . .	32
4.4.2	Quadratic Lagrangians . . . . .	33
4.4.3	Perturbations . . . . .	34
4.4.4	Atom-Laser Interaction Phase . . . . .	34
4.5	Free Particle with Gravity Example . . . . .	35
4.5.1	Gravity Gradients . . . . .	37
4.6	Cylindrical Potential Phase Shift . . . . .	38
4.6.1	Lead Cylindrical Potential . . . . .	38
<b>5</b>	<b>Apparatus</b>	<b>40</b>
5.1	Apparatus Overview . . . . .	40
5.2	Vacuum Chamber . . . . .	40
5.3	Laser Cooled Atomic Sources . . . . .	42
5.4	State Preparation . . . . .	46
5.4.1	Microwave Generation . . . . .	47

5.4.2	Composite Pulse Techniques . . . . .	48
5.4.3	Enhanced Optical Pumping . . . . .	49
5.5	Atom Interferometer . . . . .	50
5.5.1	Raman Lasers . . . . .	50
5.5.2	Raman Beam Delivery . . . . .	52
5.5.3	Raman Beam Parameters . . . . .	54
5.5.4	Interferometer Operation . . . . .	56
5.6	Vibration Isolation Subsystem . . . . .	56
5.6.1	Mechanical Design . . . . .	56
5.6.2	DSP Servo System . . . . .	57
<b>6</b>	<b>Instrument Readout and Performance</b>	<b>59</b>
6.1	Introduction . . . . .	59
6.2	Detection System . . . . .	61
6.2.1	Detection Noise Analysis . . . . .	63
6.3	Signal Extraction . . . . .	65
6.3.1	Interference Fringe Fitting . . . . .	65
6.3.2	Magnetic Phase Shifting . . . . .	66
6.3.3	High Phase Noise Regimes . . . . .	67
6.4	Shot-Noise Limited Detection . . . . .	69
6.5	Direct Balanced FM . . . . .	71
6.6	Sensitivity to Environmental Noise . . . . .	72
6.6.1	Acceleration . . . . .	72
6.6.2	Tilts . . . . .	73
6.6.3	Test Mass Effects . . . . .	75
6.7	Conclusion . . . . .	75

<b>7</b>	<b>Ellipse-Specific Data Fitting and Analysis</b>	<b>77</b>
7.1	Introduction . . . . .	77
7.2	Ellipse-Specific Fitting . . . . .	78
7.3	Accuracy Test . . . . .	81
7.4	Sensitivity Test . . . . .	82
7.5	Geometric Ellipse Fitting Techniques . . . . .	84
7.6	Conclusion . . . . .	85
<b>8</b>	<b>BIG G - Newton's Constant</b>	<b>86</b>
8.1	Introduction . . . . .	86
8.2	Experimental Setup . . . . .	87
8.3	Procedure . . . . .	89
8.3.1	Data Acquisition . . . . .	89
8.3.2	Environmental Background . . . . .	89
8.3.3	Data Weighting and Fitting . . . . .	91
8.3.4	Fit Results . . . . .	91
8.3.5	Long Term Statistics . . . . .	94
8.4	Systematics . . . . .	97
8.4.1	Atomic Ensemble Localization . . . . .	97
8.4.2	Source Mass Density (Homogeneity) . . . . .	98
8.4.3	Source Mass Radial/Vertical Displacement . . . . .	99
8.4.4	Magnetic Field Gradients . . . . .	100
8.4.5	Coriolis Phase Shift . . . . .	102
8.4.6	Detection Aperturing . . . . .	104
8.4.7	Cold Atom Collisions . . . . .	105
8.4.8	Interferometer and State Selection Parameters . . . . .	106



8.4.9	Detection Normalization Coefficients . . . . .	108
8.4.10	Deviation from Quadratic Lagrangian . . . . .	111
8.4.11	Systematics Results . . . . .	113
8.5	Conclusion . . . . .	114
<b>9</b>	<b>Horizontal (<math>T_{x,z}</math>) Gradiometer</b>	<b>116</b>
9.1	Horizontal Gradiometry . . . . .	116
9.1.1	Setup . . . . .	117
<b>10</b>	<b>Conclusion</b>	<b>123</b>
10.1	Summary . . . . .	123
10.2	Future Improvements . . . . .	124
10.3	Future Measurements . . . . .	124
10.4	Next Generation . . . . .	125
<b>A</b>	<b>Cs Properties</b>	<b>126</b>
<b>B</b>	<b>Optics Layout and Laser Frequencies</b>	<b>127</b>
	<b>Bibliography</b>	<b>131</b>

# List of Figures

1.1	Gravity Gradient Diagram . . . . .	2
3.1	1 dimensional MOT diagram. . . . .	20
3.2	Atomic fountain configuration. . . . .	22
3.3	Raman level scheme. . . . .	23
4.1	Interferometer classical analogue . . . . .	28
4.2	Interferometer recoil diagram. . . . .	30
4.3	Pb source mass diagram. . . . .	39
5.1	Gradiometer Apparatus Diagram. . . . .	43
5.2	Scan of the 2 photon Raman frequency. . . . .	55
6.1	Detection Setup. . . . .	61
6.2	Detection modulation transfer signal. . . . .	64
6.3	Gaussian elimination with high phase noise. . . . .	68
6.4	Vibration isolation servo. . . . .	69
6.5	Shot noise limited detection. . . . .	70
6.6	Immunity to vertical acceleration. . . . .	73
6.7	Sensitivity to tilt rotation rates. . . . .	74
6.8	Gradiometer signal Allan variance. . . . .	75

7.1	Ellipse fitting example. . . . .	80
7.2	Gravimeter ellipse fitting detection. . . . .	82
7.3	Magnetic phase shift verification of ellipse-specific fitting. . . . .	83
8.1	Schematic of the gradiometer experiment. . . . .	88
8.2	Typical Pb gravitational phase shift. . . . .	90
8.3	Picture of the Pb apparatus. . . . .	93
8.4	G data. . . . .	94
8.5	World's G data. . . . .	95
8.6	Allan variance figure. . . . .	96
8.7	Pb density measurements. . . . .	99
8.8	Pb phase shift radial displacement dependence. . . . .	100
8.9	Magnetic field gradient interferometer phase. . . . .	103
8.10	Transverse launch velocity phase shifts. . . . .	104
8.11	$m_f=0$ detection aperture. . . . .	105
8.12	Pb phase shift vs parameter offsets. . . . .	109
8.13	G data run Histogram distribution. . . . .	110
8.14	Dependence on Detection Normalization. . . . .	111
9.1	Horizontal Tzx gradiometer configuration. . . . .	118
9.2	70ms Tzx interferometer fringes. . . . .	119
9.3	Tzx noise. . . . .	121
9.4	Tzx rotational sensitivity. . . . .	122
B.1	Cs level diagram. . . . .	128
B.2	Trapping and detection optics layout. . . . .	129
B.3	Raman optics layout. . . . .	130

# List of Tables

4.1	Atom-Laser interaction propagator matrix element. . . . .	34
8.1	Uncertainty Limits. . . . .	114
A.1	Table of Cesium properties. . . . .	126

# Acknowledgements

I am thankful to have had the opportunity to work in Mark Kasevich's lab. His knowledge and vision of the experiment are unparalleled and I have learned a lot through his teachings. Throughout my studies, I have been blessed to work alongside with some very gifted and great colleagues. It was a pleasure to work with Greg Foster, the last post-doctorate on the experiment. Together we learned the nitty gritty details of the apparatus in understanding and characterizing its sensitivity and accuracy. I am grateful for everything that I have learned from him. Jeff McGuirk and Mike Snadden first introduced me to the project. Mike, a former postdoc, and Jeff, a former graduate student, would always find the time to teach me the essential skills useful in the laboratory and for understanding the experiment. Jeff's work ethic was characteristic of the group and I am happy to have learned from it. I would like to thank people from other projects of Mark's. The numerous conversations with Ari Tuchman, Todd Gustavson, Chad Orzel, Yoav Shaham, and Arnaud Landragin were invaluable. My years at Yale would not have been as enjoyable if not for my great friends, Adam, George, Tolya, and Mike, and from my family. Last, and not least, I am eternally grateful for the love and support from Dita.

# Chapter 1

## Introduction

### 1.1 Gravity Gradiometry

Gravity gradiometry is the measure of the change in the force of gravity over space. Typical large gradient signals are observed from sources characterized by a large differential mass distribution. Examples of such sources include underground oil or mineral deposits that are spread out over a large area, or conversely a concentration of clusters of diamonds, characterized by an accumulation of heavy metals in the ground called kimberlite pipes, which have a significantly different density profile as compared to the surrounding soil. A mountain within the ocean provides a large gradient signal, useful for passive navigation of a submarine in a poorly mapped terrain.

The measurement of changes in the gravitational field is performed with a gravity gradiometer. The instrumentation used to measure gravity is varied, but typically relies on observing the gravitational influence on a test mass. Our instrument measures gravity's influence on the atomic wavefunction of a collection of laser cooled

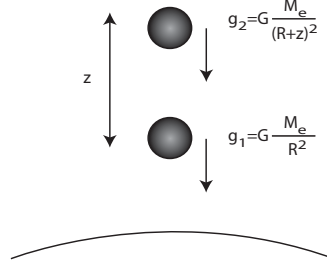


Figure 1.1: Diagram of the Earth's gravitational gradient.

Cs atoms, as a phase shift, with a precision of  $4 \times 10^{-9}/s^2$  over  $10\text{m}^1$ . The accuracy was demonstrated at  $0.09/s^{-2}$  (over  $10\text{m}$ ) through a precision measurement test of the Newtonian gravitational constant,  $G$ .

### 1.1.1 Accelerometers and Gradiometers

Traditional measurements of gravity often involved the use of a mass-spring accelerometer system or a torsion balance. The former infers acceleration from the displacement of a source mass attached to a spring while the latter measures the twisting action of a source mass balanced at the end of a long fiber. The fundamental challenge of gravimetry has been the indistinguishability of the accelerometer platform vibration from true acceleration signal. This is a consequence of Einstein's equivalence principle, which states that an acceleration measured in a laboratory freely falling under the influence of uniform gravity can not be distinguished from the same measurement with the reference frame moving at same acceleration in no gravitational field. In other words, reference platform accelerations in gravimeters mimic, and are indistinguishable from, true gravitational signals.

Gravity gradiometry is not limited by the equivalence principle since the measurements are non-local. False gravity signals from reference platform motion are

---

<sup>1</sup>The unit of a gravity gradient is the Eotvos,  $E$ .  $1E = 10^{-9}/s^2$  and is typically quoted for a baseline of  $10\text{m}$

coupled in a common-mode manner between the two accelerometers. Rigidly connected accelerometers will reject, to some degree, vibrational acceleration noise in the difference signal. The degree of rejection is dependent on the method and type of structural support, and hence the baseline separation distance. The instrument presented in this work is immune to vibration noise along the measurement axis while maintaining excellent short and long term stability and accuracy. The measurement process involves laser light that is common to both gravimeters. Vibration induced noise is therefore common-mode and cancels within the gradient difference.

A further limitation applies to relative gravimeters when the instrumental accuracy drifts, requiring calibration from a known gravity signal or an absolute gravimeter. Our gravity gradiometer measurement process is referenced to the phase of the optical light used in the interferometer, the wavelength of which is stabilized to a well known microwave transition, making the device both absolute and highly sensitive.

Our gradiometer differs fundamentally from previous instruments through the use of laser-cooled atoms in a matter wave interferometer. Laser cooling of atomic species has had a rich history over the past 20 years. The first observation of light induced slowing of atoms occurred in 1982, after much theoretical work beginning in the previous decade. Soon afterwards, in 1985, the “optical molasses” effect[1–3] was demonstrated, in which atomic motion was damped in all directions by laser induced forces. The lasers were Doppler shifted below a resonance, so when the atoms moved toward the light they were Doppler shifted into resonance and uniformly scattered photons. The net effect dampened the atomic motion in a region of space, creating an analogue to “molasses”. As kinetic energy dissipated to the optical field, the atoms were subsequently cooled, achieving  $\mu\text{K}$  temperatures. The introduction of magnetic fields allowed confinement, creating a magneto-optical trap, MOT.



### 1.1.2 Light Pulse Matter Wave Interferometry

Laser cooling and magnetic trapping has become a versatile laboratory tool for producing large numbers of atoms at very low temperatures. With the advent of optical over microwave transitions, internal degrees of freedom, i.e. atomic energy, are correlated in a 1:1 manner with an external degree of freedom, i.e. momentum. Atom-photon interactions can be used to create closed path separations within phase space. The fundamental length scale of interference is given by the atomic deBroglie wavelength. A relative atomic phase difference accrues due to inertial effects on the wavefunction over the paths. Thus, atom interferometry becomes an excellent tool for measuring inertial forces with precision competitive with that of traditional techniques. The exceptional precision of an atom interferometer gravity gradiometer makes it a valuable tool for use in inertial navigation, oil and mineral exploration, study of geologic features, and fundamental tests of gravity.

Atom interferometry provides an absolute measurement of gravitational accelerations since the gravity phase is referenced to a laser phase frequency stabilized to an atomic hyperfine transition. A gravimeter, similar to our gradiometer, measured the local Earth acceleration,  $g$ , with an absolute uncertainty of  $3 \times 10^{-9}g$  [4]. Our gravity gradiometer measured the Earth gradient and demonstrated a differential acceleration sensitivity of  $4 \times 10^{-9}g/Hz^{1/2}$  to gravity gradients [5]. Similar techniques have been used to demonstrate an atom gyroscope with a record short term sensitivity of  $6 \times 10^{-10}(\text{rad/s})/Hz^{1/2}$  [6] and measure the fine structure constant,  $\alpha$ , at 3.1 ppb [7]. We have used our gradiometer to make a proof of principle measurement of the Newtonian gravitational constant to 4 parts per thousand (ppt) with a systematic uncertainty of 3 ppt, the latter limited by vacuum chamber optical access. Atom interferometer based sensors are poised to make significant contributions in navigation

and remote sensing applications along with precision measurements.

# Chapter 2

## Gravity Gradiometry

This chapter will give a basic overview of gravity gradiometry, consisting of theory and methods of measurement. Gravity gradiometry devices will be briefly discussed and compared. Physical measurements involving gravity gradiometers will be mentioned, both industrial and scientific in application.

### 2.1 Gravity Gradients

The Newtonian definition of gravity is that of a conservative force whose associated scalar field,  $\Phi$ , is the gravitational potential:

$$\Phi(x) = -G \int \frac{\rho(x') dV}{|x - x'|} \quad (2.1)$$

where  $\rho$  is the mass density over volume  $V$  and  $G$  is the the gravitational constant, otherwise known as Newton's constant. The latter variable describes the characteristic strength of gravitational interactions and is the weakest of the fundamental forces. It is for this reason that gravity measurement are difficult in comparison, say, to measurements of electricity and magnetism.

The gravitational acceleration,  $\mathbf{g}$ , is given as the gradient of the scalar field and, hence, is a vector. The gravity gradient,  $\mathbf{\Gamma}$ , is the spatial derivative of  $\mathbf{g}$ :

$$\mathbf{g} = -\nabla\Phi = \left[\frac{\partial\Phi}{\partial x}, \frac{\partial\Phi}{\partial y}, \frac{\partial\Phi}{\partial z}\right] \quad (2.2)$$

$$\Gamma_{i,j} = -\nabla_i g_j = \nabla_i \nabla_j \Phi \quad (2.3)$$

The gravitational gradient is a second rank tensor, i.e. a matrix, whose components represent change along  $i^{th}$  axis of the  $j^{th}$  component of gravity. For example,  $\Gamma_{z,z}$  represents the vertical change of the vertical gravitational component of  $\mathbf{g}$  and, likewise,  $\Gamma_{x,y}$ , is the horizontal change, along x, of the y-horizontal component of  $\mathbf{g}$ .

The gravitational gradient tensor is symmetric:

$$\Gamma_{i,j} = \Gamma_{j,i} \quad (2.4)$$

Furthermore, as a consequence of the conservative nature of the gravitational field, the sum of the diagonal components of the gravity gradient tensor is null:

$$\sum_i \Gamma_{i,i} = \Gamma_{x,x} + \Gamma_{y,y} + \Gamma_{z,z} = 0 \quad (2.5)$$

This implies that in order to determine the components of the gravitational gradient tensor, in cartesian coordinates, only 5 components are necessary: Two diagonal and 3 off axis ( $i > j$  or  $j > i$ ) components.

The gravitational gradient tensor above is defined in the cartesian coordinate system. A transformation to another coordinate system will change the values of the elements of the gravity gradient tensor. In profiling the gradient field of an object it is useful to obtain information without reference to a specific coordinate system. There are a few properties of the gradient tensor that can be exploited to obtain invariant

combinations of the cartesian gradient components. These combinations are invariant under arbitrary rotations. For example, the differential curvature magnitude

$$|\Gamma_c| = \sqrt{4\Gamma_{x,y}^2 + (\Gamma_{y,y} - \Gamma_{x,x})^2} \quad (2.6)$$

is invariant under rotations about the vertical [8, 9]. The determinant and subdeterminants of the gradient tensor are invariant to arbitrary rotations as well

## 2.2 Applications

Any application that requires knowledge of the presence of or the effects of a gravitational body is suited for a gravity gradiometer. The scale of the mass required is typically large, as the current limit for gradient measurements is on the order of  $1 \times 10^{-10} g/m$  ( $1g=9.8m/s^2$ ). The unit of gradiometry is the Eötvös unit,  $1E= \times 10^{-9}/s^2$ . As an example, the Earth's change in gravity over 1m is on the order of 3000E.

### 2.2.1 Inertial Navigation

Inertial navigation relies on measuring the rotational and gravitational effects on a moving body and altering the trajectory accordingly. Instruments involved include gyroscopes, to measure rotation rates, and accelerometers, to measure changes in velocity. A further aid involves the use of a global positioning system, GPS. However, GPS is not completely reliable as it is relatively easy to jam its signal. Gravitational effects on inertial navigation include gyroscope definitions of a platform being skewed by gravitationally large massive bodies. A gravity gradiometer could correct for the gravitational anomaly affecting  $\mathbf{g}$ . For instance, the accuracy of a missile hitting

its target can be strongly influenced by the gravitational gradients at the launch point. GPS positioning would be aided by onboard gravimeters to account for inhomogeneities in the Earth's field and therefore perform onboard orbital adjustments.

### **2.2.2 Covert Navigation**

Covert navigation is by necessity a passive only process. Onboard a submarine, for example, use of sonar is an active form of navigation that broadcasts position information. Gradiometers offer a mass detection method to aid in navigation through poorly mapped underwater terrains, i.e. detection of mountain ranges and trenches without simultaneously providing a localizable signal.

### **2.2.3 Resource Exploration**

Nonuniform underground densities affect the local value of the gravitational acceleration and the gravity gradient. There are various such features that produce a sizeable signal detectable by gradiometer instruments. Large underground pockets, or tunnels, have been mapped with a gradiometer [10]. Gradiometers have been used to mapped oil fields within the Gulf of Mexico. Kimberlite pipes, indicating the presence of diamonds, can be measured with a gravity gradiometer and such measurements are competitive with traditional magnetometry measurements.

Geologic surveys use gravimeters to map out the vertical acceleration field,  $g_z$ , of a region of interest. A large underground mineral or oil deposit will change the local gravity signal. This data is often used to interpolate the gravitational gradient,  $\nabla g$ . The resulting signal has features more reflective of the underground deposit, such as boundaries. The interpolated signal emphasizes the sharpness and resolvability of anomalies more clearly than pure gravitational data. However, the interpolation is

just is just that – a mathematical estimate – and can result in noisy measurements. A direct gravity gradient measurement could potentially combine the strengths of both approaches – the accuracy of pure gravitational data with the detail of interpolation, while minimizing the pitfalls.

## 2.2.4 Newton’s Constant

The weak coupling of gravity compared to other forces makes precision gravity experiments difficult. This is manifested in the relatively poor knowledge of the Newtonian gravitational constant,  $G$ , compared to other fundamental constants [11]. The traditional torsion pendulum method for measuring  $G$  involves a well characterized moving source mass producing a torque on a test mass attached to a long fiber. Measurement of the test mass displacement, coupled with knowledge of the mechanics of the pendulum and of the source-test mass gravitational force determines  $G$ . Other recent methods make use of a Fabry-Perot optical cavity [12], a flexure-strip balance [13], and a falling corner-cube gravimeter [14]. Since the first precision measurement of  $G$  in 1895 [15], the standard precision has not improved beyond the fraction of a part per thousand (ppt) level. Recently a few key experiments have reached to  $<100$  parts per million (ppm) [16–18]. The most sensitive measurements of the gravitational constant, performed by Gundlach and Quinn, achieved a level of 14 ppm and 41 ppm, respectively.

The accuracy of the value for  $G$  has recently come into question. An 83 ppm measurement in 1996 by Michaelis [18] using a dynamic fiberless torsion balance differed by 42 standard deviations from the CODATA value of  $G$  at the time. Questions have been raised about the accuracy of other experiments as well. Taking into account the 1996 discrepancy, fiber twist anelasticity [19], and the historical measurement difficulties, in 1998 CODATA published a value for  $G$  increasing the statistical un-

certainty by a factor of 12 from the previously published 1986 value. The subsequent precision measurements of Gundlach and Quinn do not corroborate the result of Michaelis, but still disagree with the previous norm by 200 ppm. The possibility of unknown systematic errors make it important to measure  $G$  with independent methods. Our approach is distinguished from previous techniques in that we sense gravity with laser cooled Cs atoms as opposed to a macroscopic test mass. Furthermore, our approach is the first  $G$  measurement to depend on quantum mechanics.

Atom interferometry permits precise absolute measurements of inertial forces on atoms. Devices based upon this technology meet and exceed other state of the art instruments in gravimetry [4], gradiometry [5], and rotation sensing [6]. A precision experiment, for example, has measured the fine structure constant,  $\alpha$ , at 7.4 ppb [20]. We have used our gradiometer to make a proof of principle measurement of the Newtonian gravitational constant to 4 parts per thousand (ppt) with a systematic uncertainty of 3 ppt, the latter limited by vacuum chamber optical access. We measured the differential acceleration of a 540 kg lead, Pb, source mass precisely positioned at two locations between two vertically separated gravimeters. With accurate knowledge of the atomic trajectories, Pb geometry and composition, we calculated the gravitationally induced phase shift in our atom interferometer and extracted a value for  $G$ . The accuracy was characterized with a thorough study of systematics that might influence our measurement.

## 2.3 Instrumentation

There are currently only a few different types of instruments that measure spatial changes in gravity. These instruments are all based on techniques to measure the acceleration produced by a source mass on a macroscopic test mass.



One of the earliest commercial devices measures acceleration via the displacement of a mass attached to a spring. Originally developed by Bell Aerospace Textron and later acquired by Lockheed Martin [21], this accelerometer design paired into a gradiometer configuration. Sensitivity is reported to be within the range of  $2 - 20\text{E}/\sqrt{Hz}$  with an accuracy of approximately  $10\text{E}$  [22]. The BHP company made use of the Lockheed Martin gradiometer to search for subsurface oil and minerals [23]. Uses have also included detection of underground structures [10] and as an aid to passive navigation onboard a Trident class submarine [24].

The most sensitive gravity gradiometer is the superconducting gradiometer developed at the University of Maryland[25]. This gradiometer also works on the principle of measuring accelerations via the displacement of a mass attached to a spring. The concept here uses a superconducting proof mass and a SQUID (superconducting quantum interference device) amplifier to measure changes in the current through a superconducting sensing coil. The superconducting gravity gradiometer (SGG) couples two proof mass-spring systems coupled together by superconducting circuits, with the proof masses constrained to motion along one common degree of freedom. This coupling of mechanical motion to electrical activity permits extremely sensitive measurements of accelerations. The short term sensitivity is reported at  $0.07\text{E}/\sqrt{Hz}$  for short time. However, the instrument suffers from  $1/f$  noise preventing long term integration.

A 3-axis SGG has been used in a test of short scale deviation of Gauss' law for gravity [26]. For a Yukawa gravitational potential of the form  $\phi = -GM/r(1 + \alpha e^{-r/\lambda})$ , this group measured  $\alpha = (0.9 \pm 4.6) \times 10^{-4}$  for  $\lambda = 1.5\text{m}$ . The same experiment also presented a measurement of the sum of the diagonal of the gravity gradient tensor, extrapolating out the finite baseline. Their result of  $(0.58 \pm 3.10) \times 10^{-4}\text{E}$  was a null test of the inverse-square law for gravity.

A gravitational sensor that does not rely on the mass spring effect is the corner-cube gravimeter[27]. Here, a corner-cube retroreflector is dropped in free fall within a vacuum chamber while a laser tracks the position in a Michelson interferometer setup relative to an active-stabilized reference . The gravimeter has demonstrated acceleration sensitivity of  $15\mu\text{Gal}$  with an accuracy of  $2\mu\text{Gal}$ <sup>1</sup>. The corner-cube gradiometer uses two such gravimeters but with a common reference laser source. The reported sensitivity of the corner-cube gradiometer is  $400\text{E}/\sqrt{Hz}$ [28].

Recently, the corner-cube gravimeter was used in a precision measurement of the gravitational constant,  $G$ [14]. The measurement was performed by measuring the change in acceleration of the corner-cube test mass as a Tungsten source mass was vertically displaced around the vertical axis of the gravimeter. Their result of  $G=(6.6873 \pm 0.0094) \times 10^{-11}m^3kg^{-1}s^{-2}$  agreed with the 1998 CODATA value for  $G$ [11].

---

<sup>1</sup>A Gal is a unit of acceleration.  $1\text{ Gal} = 10^{-2}\text{m/s}^2$ .

# Chapter 3

## Laser Cooling and Trapping

This chapter describes the theory behind atom-photon interactions as they apply to the techniques we have taken advantage of in order to measure changes in gravity using atom interferometry. The technique of magneto-optical trapping of atoms is presented followed by schemes used to cool the trapped ensemble of atoms. Next, a treatment of two-photon interactions is detailed describing the atom-photon interactions involved in the atom interferometer. For a more detailed discussion of laser cooling and trapping see [29, 30].

### 3.1 Atomic structure

This work is based on the Cesium (Cs) atom, a member of the alkali series. The basic ground state nuclear structure consists of a closed inner shell and one valence electron in the S-state. The nuclear spin has the value  $I = 7/2$ , and the total electronic spin is  $S = 1/2$ . In the ground state, this gives two possible combinations for the total spin,  $F = I + S$ ,  $F = 3$  or  $F = 4$ . These are the two hyperfine ground states for Cs, with the energy difference being exactly 9.192631770GHz. The ground state hyperfine transition in Cs is well characterized and in fact provides the current

basis for the definition of the second.

For all alkali atoms, transitions to the next lying states from the ground state are known as  $D_1$  and  $D_2$  transitions, respectively. In Cs, the next two excited states are the  $6P_{1/2}$  and  $6P_{3/2}$  states. We use  $D_2$  transitions. The  $6P_{3/2}$  state has a total electronic spin  $J = 3/2$ , giving a total hyperfine spin range of  $F' = 2, F' = 3, F' = 4, F' = 5$ . In the absence of a magnetic field, each hyperfine level is  $2F + 1$  degenerate with magnetic Zeeman sublevels.

## 3.2 Two-Level Atoms

The idea of Rabi flopping and pulse area are presented here and will form an introduction to the Cs transitions used within our experiment. The simplest transition involves approximating Cs as a two level atom interacting with a monochromatic light field. This Hamiltonian is written as:

$$\hat{H} = \hbar\omega_g|g\rangle\langle g| + \hbar\omega_e|e\rangle\langle e| - \mathbf{d} \cdot \mathbf{E} . \quad (3.1)$$

The first two terms represent the two internal state energy levels, expressed in the ground and excited basis states,  $|g\rangle$  and  $|e\rangle$ , respectively. The last term represents the atom-laser interaction between the atomic dipole,  $\mathbf{d}$  and the electric field of amplitude,  $E_0$ , and phase,  $\phi$ :

$$\mathbf{E} = \mathbf{E}_0 \cos(\omega t + \phi) . \quad (3.2)$$

The dipole interaction couples off axis elements, with a characteristic Rabi frequency:

$$\Omega_{eg} \equiv \frac{\langle e | \mathbf{d} \cdot \mathbf{E} | g \rangle}{\hbar} . \quad (3.3)$$

describing oscillations between the ground and excited states for resonant,  $\omega = \omega_e - \omega_g$ , light.

The time-dependent Schrödinger equation is applied to the above Hamiltonian to solve for the wavefunction of the two level atom. Applying a suitable coordinate transformation and the rotating wave approximation<sup>1</sup>, a relatively simple solution is obtained. The probability that the atom to be in the excited state is a sinusoidal function of the Rabi frequency:

$$P_e(\tau) = \frac{1}{2}[1 - \cos(\Omega_{eg}\tau)] . \quad (3.4)$$

Introducing a detuning from resonance,  $\Delta = \omega - (\omega_e - \omega_g)$ , the generalized Rabi frequency is  $\Omega'_r = \sqrt{\Omega_{eg}^2 + \Delta^2}$ , giving

$$P_e(\tau) = \frac{1}{2}\left[1 - \frac{\Omega_{eg}^2}{\Omega_r'^2} \cos(\Omega_{eg}\tau)\right] . \quad (3.5)$$

Furthermore, the energy levels are shifted in value due to the atom-laser interaction. This AC Stark shift is given by:

$$\Delta E_g = -\Delta E_e \simeq \frac{\hbar \Omega_{eg}^2}{4\Delta} , \quad (3.6)$$

valid in the limit of large detuning.

From Equation 3.5, if an atom initially in the ground (excited) state is illuminated with resonant light of duration  $\tau = \pi/\Omega_r$  the atom will be transferred to

---

<sup>1</sup>Solution of the two level atom yields two frequency terms:  $\omega_{dif} = \omega_e - \omega_g$  and  $\omega_{sum} = \omega_e + \omega_g$ . The summation term oscillates the wavefunction at a much larger frequency than the difference term, so that it may be ignored on the time scale of the latter term.

the excited (ground) state with 100% probability. This pulse duration is called a  $\pi$  pulse. Likewise, a  $\pi/2$  pulse with  $\tau = \pi/2\Omega_r$  creates an equal superposition of ground and excited state,  $(|e\rangle + |g\rangle)/\sqrt{2}$  for an atom initially in either state. Often the case involves dephasing effects such as spontaneous emission and inhomogeneous broadening, creating non unity transfer efficiency.

The finite natural lifetime,  $\tau_n$ , of an atomic state is the inverse of the natural linewidth,  $\tau_n = 2\pi/\Gamma$ . The scattering rate is proportional to the natural linewidth and inversely proportional to the transfer probability. For Cesium,  $\Gamma_n = 2\pi \times 5.18\text{MHz}$ , the natural lifetime is  $\tau_n = 30.70\text{ns}$  [30].

The steady-state solution of the two level atom in a driving laser field gives:

$$P_e = \frac{1}{2} \frac{I/I_{sat}}{1 + I/I_{sat} + 4(\Delta/\Gamma)^2} , \quad (3.7)$$

where  $I_{sat}$  is the saturation intensity. Given the natural lifetime, an atom irradiated with incoherent light can spend at most half the time in the excited state after a saturation point of intensity. The saturation intensity is defined such that the probability that the atom is in the excited state equals 1/4.

$$\frac{I}{I_{sat}} = 8 \frac{|\Omega_{eg}|^2}{\Gamma^2} , \quad I_{sat} = \frac{\hbar\omega\Gamma_n k^2}{12\pi} . \quad (3.8)$$

For the Cs  $F = 4 \rightarrow F' = 5$  transition,  $I_{sat} = 1.12 \text{ mW/cm}^2$ .

When an atom absorbs a photon with a laser propagation  $\mathbf{k}$ -vector, it absorbs a momentum,  $\hbar\mathbf{k}$ . However, the subsequent spontaneous emission scatters photons in a random direction. The net effect is a momentum change along the absorbed photon's  $\mathbf{k}$ -vector, with a force given by the net momentum transfer over the scattering time:

$$\mathbf{F}_{scat} = \frac{\hbar\mathbf{k}}{\tau_{scat}} = \frac{\hbar\mathbf{k}\Gamma_n}{2} \frac{I/I_{sat}}{1 + I/I_{sat} + 4(\delta/\Gamma)^2} . \quad (3.9)$$

This is a dissipative force, with the atom coupling to the vacuum field through spontaneous emission. Through this mechanism, we can cool the center of mass motion of the atoms.

## 3.3 Laser Cooling and Trapping

### 3.3.1 Doppler Cooling

Consider an atom, moving with velocity  $\mathbf{v}$  interacting with a monochromatic laser source with a specific  $\mathbf{k}$ -vector and detuned below resonance, i.e. red detuned. From the atomic reference frame, the laser frequency is Doppler shifted to  $\Delta - \mathbf{k} \cdot \mathbf{v}$ . If  $\mathbf{v}$  is counterpropagating with  $\mathbf{k}$ , then the light is Doppler shifted into resonance with the atom. The effect causes a net momentum to be imparted to the atom along the direction of  $\mathbf{k}$ . Now introduce a second laser, with the same red detuning, but with opposing propagation as compared to the first laser. The atom is now opposed by laser-induced momentum in either direction. The dissipation of energy to the vacuum and atomic confinement by the above process is called Doppler cooling.

Doppler cooling can be generalized to three dimensions through three pairs of intersecting counterpropagating red-detuned laser light. Motion of the atom in the intersection is viscously damped, creating an "optical molasses". The temperature limit to this cooling mechanism is given by:

$$T_D = \frac{\hbar\Gamma}{2k_B} . \quad (3.10)$$

For Cesium,  $T_D \sim 125\mu\text{K}$ . Doppler cooling is limited by the diffusive random-walk caused by the spontaneous emission.

### 3.3.2 Polarization Gradient Cooling

Sub-Doppler cooling can be achieved through the use of polarized trapping light and the effects of AC Stark shifts [31]. Counterpropagating light of crossed circular polarization ( $\sigma^+ - \sigma^-$ ), or crossed linear polarization (lin  $\perp$  lin), create a spatially varying light field. For the latter configuration, a light field of spatially varying polarization is created. It changes from linear to circular to orthogonal linear to opposite circular over half a wavelength ( $\lambda/2$ ), to linear polarization, rotating spatially with a period of  $\lambda/4$ . This spatial variation creates a spatial variation in the AC Stark shift. When an atom moves non-adiabatically through this field, the population distribution of magnetic sublevels has insufficient time to redistribute to the lowest energy configuration. This causes the atom to decay to a lower energy state, via coupling of photons to the vacuum field. The atom is continually moving into a field where it has a greater potential energy than the lowest available state. The limit of this polarization gradient cooling is confined to a few photon recoils:

$$T_{rec} \sim \frac{(\hbar k)^2}{2k_B m} . \quad (3.11)$$

The ( $\sigma^+ - \sigma^-$ ) cooling configuration is not based on the spatially varying AC Stark shift. The polarization of the light field produces linearly polarized light rotating in polarization by an angle of  $2\pi$  every optical wavelength,  $\lambda$ , producing a constant Stark shift as a function of position. Atoms in the  $m_f = 0$  sublevel will be more populated than the  $m_f = \pm 1$  sublevels. As the atoms move diabatically through the light field they experience a constant rotating quantization axis, creating a ground state distribution that lags the appropriate steady-state distribution for the instantaneous (local) light field polarization direction. For atoms moving toward  $\sigma^+$  light, say, the atoms are more likely to be populated in the  $m_f = +1$  state than the  $m_f = -1$ .



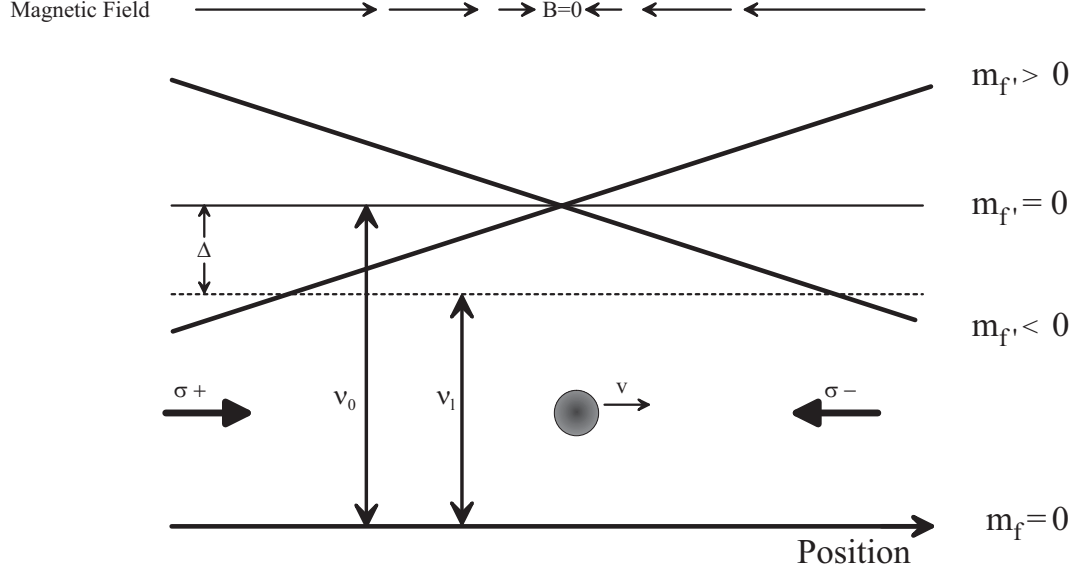


Figure 3.1: Illustration of the Zeeman shifted magnetic sublevels for an atom moving in a 1 dimensional MOT.  $\Delta$  is the detuning of the trapping light,  $\nu_l$ , from the zero field atomic resonance,  $\nu_0$ .

The Clebsch-Gordan coefficients for the Cs cooling transition,  $F=4 \rightarrow 5'$ , describes a larger scattering rate for the atoms populated in  $m_f = +1$  than  $m_f = -1$  when interacting with  $\sigma^+$  light, thereby producing a restoring force. Likewise for atoms moving toward the  $\sigma^-$  light.

The polarization gradient cooling limit for Cs is  $\sim 2\mu\text{K}$ .

### 3.4 Magneto Optical Trapping

In the previous cooling schemes, the atoms are cooled but not confined. Diffusive random walks cause the atoms to eventually leak out of the trapping region. This is due to the absence of a field minimum, or a restoring force, to localize the atoms. An applied magnetic field with a gradient such that there exists a field minimum in the center of the molasses will create such a restoring force due to the lifted degeneracy of the Zeeman sublevels.

A quadrupole field configuration is used, consisting of two identical circular coils separated by their diameter, with the trap in between, and counter propagating current. This is known as an anti-Helmholtz configuration. The Zeeman shift is proportional to the distance from the center of the trapping region, thereby changing the effective detuning as seen by the atom. Consider red detuned light and an atom moving in a direction such that the negative Zeeman sublevels decreases in energy, and hence increases in detuning, with a velocity against  $\sigma^-$  light. Clebsch-Gordon coefficients giving the relative transition strengths imply that  $\sigma^-$  light will be preferentially absorbed and scattered by the atoms rather than scattering from  $\sigma^+$  light as the  $m_f = -1$  level is shifted closer to resonance and the  $m_f = +1$  level is shifted out of resonance. The same is true for an atom moving toward the other sign of the field gradient with velocity against  $\sigma^-$  light.

The above trapping scheme is called a magneto-optical trap (MOT) and is the trap used in this experiment. Figure 3.2b depicts the laser-cooling geometry of our experimental setup.

### 3.4.1 Atomic Fountains

MOTS are a very useful tool in studying the properties of ultracold atoms. In the absence of trapping magnetic fields, the lifetime of the trapped atoms is limited. Without trapping lasers, the atoms are free to fall under gravity. To extend the interrogation time, the atoms can be launched vertically into a parabolic trajectory.

The atomic fountain is formed in a similar manner to that used in creating an optical molasses. Consider a 1-D molasses with the downward propagating beams red detuned and the upward propagating beams less detuned or detuned above resonance, called blue detuned. The atoms are cooled into the moving frame of the light with

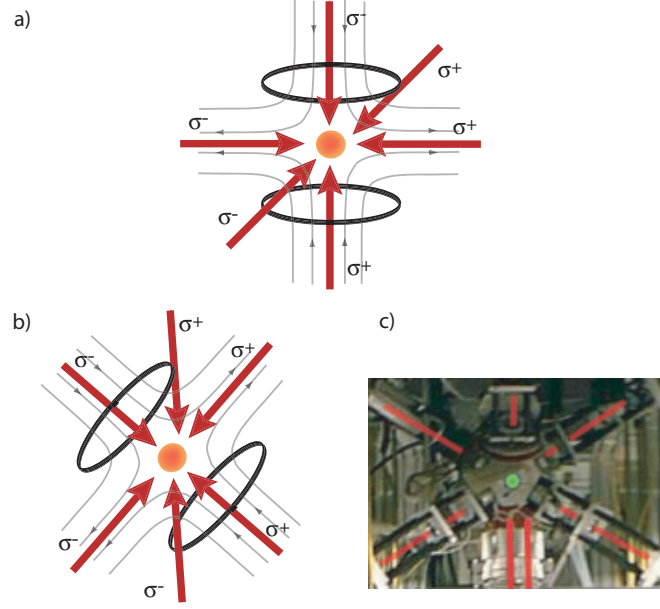


Figure 3.2: Beam geometries for a three dimensional MOT. Shown are the quadrupole coils with the trapping fields and molasses light with  $\sigma^+ - \sigma^-$  orientations for polarization gradient cooling. a) A (1,0,0) configuration where the vertical beams only launch the atoms. b) The (1,1,1) configuration used in our experiment. c) Picture of one of the gravimeters in our gradiometer. Depicted are the molasses light, with interferometer light propagating vertical through the MOT.

a velocity

$$v = \frac{\delta\omega}{k} , \quad (3.12)$$

with the relative frequency difference of the detuned trapping light,  $\delta\omega$ , and wavevector,  $\mathbf{k}$ . Our launch uses the six molasses beams, with the three upward propagating beams less detuned from resonance than the upward propagating beams. Here, the velocity is:

$$v = \frac{\delta\omega}{k \sin(\pi/3)} . \quad (3.13)$$

For example, in the vertical gradiometer configuration, the downward propagating trapping light was detuned 1.06MHz to the red while the upward propagating light was detuned 1.06MHz to the blue. Experimentally, this frequency difference produces a launch velocity of approximately 1.54 m/s for both chambers, resulting in a 12cm

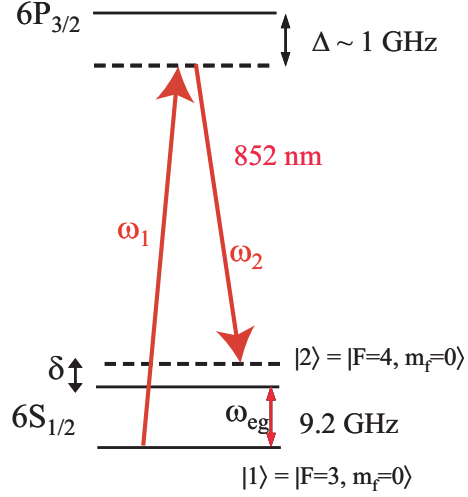


Figure 3.3: Raman level scheme

fountain height.

### 3.5 Velocity Selective Cooling

Our interferometer requires ultracold atoms with a narrow velocity distribution. Two-photon stimulated Raman transitions are used both for velocity selection of cold atoms and state manipulation within the interferometer. Figure 3.3 depicts the Cs level scheme involving a two-photon transition between the two hyperfine  $6S_{1/2}$  states and the  $6P_{3/2}$  manifold. This three level atom is illuminated with two frequencies,  $\omega_1$  and  $\omega_2$  detuned from the state  $|i\rangle$  by  $\Delta$  and  $\omega_1 - \omega_2 = \omega_{eg} + \delta$ . With a large  $\Delta$ , spontaneous emission from  $|i\rangle$  is negligible and  $|i\rangle$  can be adiabatically eliminated. This allows a two level atom approach to solving the problem with the Schrödinger equation.

The two light fields can be describe as:

$$\mathbf{E} = \mathbf{E}_1 \cos(\mathbf{k}_1 \cdot \mathbf{x} = \omega_1 t + \phi_1) + \mathbf{E}_2 \cos(\mathbf{k}_2 \cdot \mathbf{x} = \omega_2 t + \phi_2) , \quad (3.14)$$

with the effective phase and wavevector defined, respectively:

$$\phi_{eff} \equiv \phi_1 - \phi_2 \quad , \quad \mathbf{k}_{eff} \equiv \hbar(\mathbf{k}_1 - \mathbf{k}_2) \quad . \quad (3.15)$$

Note that  $\mathbf{k}_{eff}$  is  $\sim 2k_1$  for counterpropagating lasers and is  $\sim 0$  for co-propagating lasers. In the counterpropagating case, the two photon process imparts a momentum of  $2\hbar\mathbf{k}_1$  to the atom. This recoil velocity for Cs is  $\sim 7\text{mm/s}$ . This momentum change to atoms changing hyperfine states via the above two-photon process allows a 1-1 correspondence between an external degree of freedom, momentum, and an internal degree of freedom, the internal energy state. For example, an atom initially in the excited state with momentum  $\mathbf{p}$  can be mapped accordingly with a  $\pi$ -pulse as:

$$|e, \mathbf{p}\rangle \rightarrow |g, \mathbf{p} - \hbar\mathbf{k}_{eff}\rangle \quad . \quad (3.16)$$

It is this property of Cesium quantum mechanical behavior that underlies our atom interferometer. our interferometer.

A wavefunction solution has the form:

$$|\Psi(t)\rangle = c_{e,\mathbf{p}+\hbar\mathbf{k}_{eff}}(t)e^{-i(\omega_e + \frac{|\mathbf{p}+\hbar\mathbf{k}_{eff}|^2}{2m\hbar})t}|e, \mathbf{p}+\hbar\mathbf{k}_{eff}\rangle + c_{g,\mathbf{p}}(t)e^{-i(\omega_g + \frac{|\mathbf{p}|^2}{2m\hbar})t}|g, \mathbf{p}\rangle \quad . \quad (3.17)$$

For a Raman pulse of constant amplitude with duration  $\tau$  in the limit of zero two-photon detuning, the state coefficients are:

$$\begin{pmatrix} c_{e,\mathbf{p}+\hbar\mathbf{k}_{eff}}(t_0 + \tau) \\ c_{g,\mathbf{p}}(t_0 + \tau) \end{pmatrix} = \begin{pmatrix} \cos(\Omega_{eff}\tau/2) & -i\sin(\Omega_{eff}\tau/2)e^{i\phi} \\ -i\sin(\Omega_{eff}\tau/2)e^{-i\phi} & \cos(\Omega_{eff}\tau/2) \end{pmatrix} \cdot \begin{pmatrix} c_{e,\mathbf{p}+\hbar\mathbf{k}_{eff}}(t_0) \\ c_{g,\mathbf{p}}(t_0) \end{pmatrix} \quad (3.18)$$

Here, the two-photon Rabi frequency is

$$\Omega_{eff} = \frac{\Omega_{gi}\Omega_{ie}}{\Delta_{eg}} , \quad (3.19)$$

where  $\Omega_{ki}$  are the single photon Rabi frequencies between the hyperfine states  $k = |e\rangle, |g\rangle$  and  $|i\rangle$ . The two photon detuning is now a function of the frequency difference of the light and the difference from the hyperfine splitting, the total Doppler shift, the two-photon scattering recoil frequency shift, and the AC Stark shift. The two photon detuning is given by,

$$\Delta_{eg} = \omega_1 - \omega_2 - \left[ \omega_{hf} + v(k_1 - k_2) + \hbar \frac{(k_1 - k_2)^2}{2m} + \Omega_{AC} \right] . \quad (3.20)$$

The AC Stark shift is the sum of the individual single photon AC Stark shifts:

$$\Omega_{AC} = \sum_{j=e,g} \frac{\Omega_{ji}^2}{2\Delta_{ji}} . \quad (3.21)$$

The detunings are opposite in sign for the two transitions, allowing a cancellation of the two-photon AC Stark shift by balancing the single-photon AC Stark shifts. This can be accomplished by adjusting the intensity balance of the two beams.

## 3.6 Detection

We detected the atoms in both hyperfine states after the interferometer using a balanced detection with a modulation-transfer technique [32]. This permits high signal to noise detection of the cold atom signal in the presence of background atom vapor, and inference of the total atom number to allow normalization of atom number fluctuations associated with MOT loading.

A pump beam detuned from the cooling transition and modulated near 5 MHz creates a modulation in the index of refraction of the atoms. A probe beam of the same detuning is simultaneously sent through the ensemble. The modulating index of refraction created a modulation in the absorption of the probe beam which was detected on a balanced detector setup. This detection method is explained in detail in chapter 6.

# Chapter 4

## Atom Interferometry

### 4.1 Introduction

This chapter introduces the theory of atom interferometry using a path integral formalism. Inertial effects on the relative phase between the atomic wavefunctions of two ensembles is presented with this formalism. Application to our gravity gradiometer is described.

### 4.2 Classical Analogy

The method of how inertial information enters as a relative phase shift in the wavefunction of Cs atoms is detailed below. This phase shift, for a uniform acceleration field,  $\mathbf{g}$ , is

$$\phi = \mathbf{k}_{eff} \cdot \mathbf{g}T^2 . \quad (4.1)$$

The three variables are the effective wavelength of the two-photon transition (the Cs hyperfine splitting), the acceleration field (i.e. gravity), and the spacing between interferometer laser pulses,  $T$ . In a classical sense, our measurement is analogous to



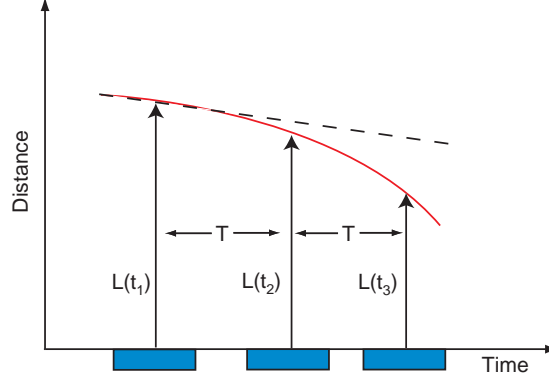


Figure 4.1: A classical determination of the average acceleration through measurement of a particles position at three points in time.

measuring the distance of a particle in free fall at three equally spaced points in time, Fig. 9.1.

In the free fall example, two position measurements yield an average value for the velocity. Three measurements of position give an average value for the acceleration:

$$a = \frac{z_1 - 2z_2 + z_3}{T^2} . \quad (4.2)$$

If we use light of a well defined frequency as our ruler and count fringes between the reference platform and the object, i.e. count phase  $\phi_i = k_{eff}z_i$ , then

$$a = \frac{\phi_1 - 2\phi_2 + \phi_3}{k_{eff}T^2} = \frac{\Delta\phi}{k_{eff}T^2} . \quad (4.3)$$

For a more semiclassical analogy, consider a deBroglie wave traveling vertically along  $\mathbf{g}$ , aligned with the interferometer light. The interferometer sequence creates a superposition of two states, one with a greater velocity. Halfway through the interferometer, light transfers the previous gain in momentum to the other wave. The end of the interferometer consists of light to readout the phase of one of the interfering deBroglie waves. A recoil space diagram is depicted in Fig. 4.2.

The deBroglie wavelength is given as  $\lambda_d = \hbar/p$ , and the phase over a distance,  $z$ , is  $\phi = \lambda_d/z$ . In freefall,  $z(t) = v_0 t + 1/2 g t^2$ . Adding the phase along path I and path II, and taking the relative phase difference gives:

$$\phi_d^I - \phi_d^{II} = k_{eff} g T^2 . \quad (4.4)$$

### 4.3 Interferometer

Our gravity gradiometer consists of two gravimeters that operate by the light pulse atom interferometry technique [33] on laser cooled Cesium ensembles within each gravimeter. The momentum recoil from the emission or absorption of a photon by a Cs atom is used to coherently split and deflect the atomic wave-packets. A  $\pi/2$  "splitter" pulse places an atom initially in the ground state with momentum  $p$  into a superposition of ground and excited states,  $|g, p\rangle \rightarrow (|g, p\rangle + |e, p + \hbar k\rangle)/\sqrt{2}$ , with the excited state gaining a photon recoil  $\hbar k$  relative to the ground state part of the wave-packet ( $k=2\pi/\lambda$ ). A "mirror"  $\pi$ -pulse drives an atom from the ground to the excited state,  $|g, p\rangle \rightarrow |e, p + \hbar k\rangle$  imparting a photon recoil kick, or vice versa causing a stimulated emission of a photon and reduction of momentum. We apply a  $\pi/2 - \pi - \pi/2$  interferometer sequence with a pulse separation  $T$  (see Fig. 4.2). The initial  $\pi/2$ -pulse separates the two wave-packets due to the difference in their momentum. The  $\pi$ -pulse redirects the wave-packet momentum, causing the two components to overlap again at time  $2T$ , when the final  $\pi/2$  interferes them. Momentum recoil creates different trajectories for the wave-packets which acquire a relative gravitationally induced atomic phase shift during the interferometer, resulting in a sensitivity to accelerations. The total phase shift  $\Delta\phi_{Tot}$  is the sum of three components: The interaction of the atom with the light pulse,  $\Delta\phi_{laser}$ , the quantum propagation phase

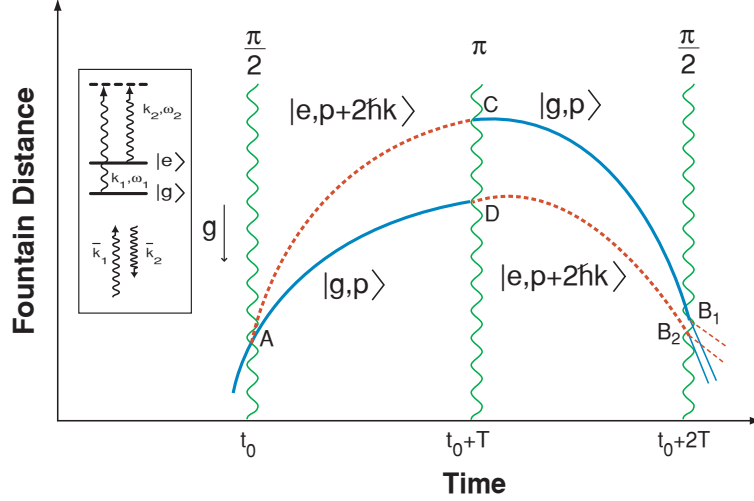


Figure 4.2: Recoil space diagram of the atoms through the interferometer showing the separation (exaggerated) of the atomic wavepackets. The area enclosed by the two paths is proportional to the mean value of acceleration over the path,  $g$ .

accrued by each wave packet over its trajectory,  $\phi_{path}$ , and the wave-packet overlap,  $\Delta\phi_{sep}$  [34, 35].

The interferometer pulses drive Doppler-sensitive two-photon optical ( $\lambda = 852\text{nm}$ ) Raman transitions[36] between the  $F = 3$  and  $F = 4$  hyperfine ground states. The counter-propagating beams have a frequency difference equal to the 9.2 GHz hyperfine splitting and are detuned from the  $6P_{3/2}$ ,  $F = 5$  excited state by  $\sim 1\text{GHz}$ . The two Raman interferometer beams are derived from a pair of high power diode lasers injection locked from the same high frequency acousto-optic modulator source and external cavity diode laser [37]. This allows precise control of the phase and frequency of the Raman beams. The use of a two-photon transition doubles the effective photon momentum recoil ( $k_{eff} = k_1 - k_2 \approx 2k_1$ ).

At the end of the interferometer the probability that atoms will be in the  $F = 4$  ground state for each gravimeter follows:[33]

$$P_{|4\rangle} = \frac{1}{2}[1 - \cos(\phi_0 + \Delta\phi)] \quad (4.5)$$

where  $\Delta\phi$  contains the gravitationally induced phase shift. Acousto-optic modulators in the Raman path are used to phase scan the fringe (equation 4.5) by changing  $\phi_0$ . We could reverse the effective propagation direction by rotating the polarization of the Raman beams with a Pockell's cell. Beam reversal takes  $k_{eff} \rightarrow -k_{eff}$ , changing the sign of the interferometer gravitational phase shift. Phase shifts that do not depend upon the Raman k-vector, e.g. second order Zeeman shifts or AC Stark shifts, can be rejected by alternating measurements between a positive and negative propagation direction, then taking the difference of the two.

## 4.4 Path Integral Approach

The relative atomic phase accrued in the interferometer can be derived using the path integral approach as presented in [35]. This approach derives the phase shift using the quantum propagator to evaluate the final wavefunction over the classical path,  $\Gamma_{cl}$ , while assuming a plane wave initial wavefunction. Perturbations to the Lagrangian describing the classical equations of motion can be evaluated over the unperturbed path as well to obtain the relative phase shift.

Three components contribute to the relative atomic phase shift from the interferometer: a path dependent term, an atom-laser interaction term, and a wavepacket overlap term

$$\Delta\phi_{Tot} = \Delta\phi_{Laser} + \Delta\phi_{Path} + \Delta\phi_{Sep} . \quad (4.6)$$

The atom-laser interaction phase shift comes from solution of the Schrödinger equation:

$$|3\rangle \rightarrow ie^{i\phi(t)}|4\rangle|4\rangle \rightarrow ie^{-i\phi(t)}|3\rangle , \quad (4.7)$$

where  $\phi(t) = \mathbf{k}_{\text{eff}} \cdot \mathbf{r}(t) + \phi_0(t)$  is the phase of the driving field at the mean position  $\mathbf{r}$  of the wavepacket at the time  $t$  of the interferometer pulse. The interferometer sequence results in

$$\Delta\phi_{laser} = \mathbf{k} \cdot (\mathbf{r}_A - \mathbf{r}_C - \mathbf{r}_D + \mathbf{r}_B) = \mathbf{k} \cdot \mathbf{g} T^2 + \phi_0 + O(\nabla \cdot \mathbf{g}) , \quad (4.8)$$

with  $\phi_0 = \phi_0^{\frac{\pi}{2}} - 2\phi_0^\pi + \phi_0^{\frac{\pi}{2}}$  the cumulative initial laser phases. The atomic wavefunctions also acquire a phase as they propagate:

$$\Psi(\mathbf{r}(t), \mathbf{v}(t)) = \Psi(\mathbf{r}(t_0), \mathbf{v}(t_0)) e^{\frac{i}{\hbar} S_{cl}[\mathbf{r}(t)\mathbf{v}(t), \mathbf{r}(t_0)\mathbf{v}(t_0)]} . \quad (4.9)$$

The path integral phase shift is determined by calculating the classical action,  $S_{cl,path} = \int L[\mathbf{r}(t), \mathbf{v}(t)] dt$  by integrating the Lagrangian  $L$  over their trajectories. The relative phase shift between the two interferometer arms is then given by

$$\Delta\phi_{path} = \frac{1}{\hbar} (S_{cl,ACB_1} - S_{cl,ADB_2}) . \quad (4.10)$$

A path separation phase shift,

$$\Delta\phi_{sep} = \frac{m\mathbf{v} \cdot \Delta\mathbf{r}_{sep}}{\hbar} , \quad (4.11)$$

where  $m$  and  $\mathbf{v}$  are the respective Cs mass and velocity, arises from the physical separation,  $\Delta\mathbf{r}_{sep}$ , of the wavepackets at the final interferometer pulse (due to the presence of a gravity gradient)

#### 4.4.1 Quantum Propagator

In the Feynman path integral approach to quantum mechanics [38], the evolution of a wavefunction from space-time point  $(z_a, t_a)$  to  $(z_b, t_b)$  is determined by the quantum

propagator,  $K(z_b, t_b, z_a, t_a)$ :

$$\Psi(z_b, t_b) = \int dz_a K(z_b, t_b, z_a, t_a) \Psi(z_a, t_a) \quad (4.12)$$

The path integral considers the contribution from all possible paths between the two space-time points. The quantum propagator can thus be expressed as the sum of all these contributions:

$$K(z_b, t_b, z_a, t_a) = N \sum_{\Gamma} e^{\frac{i}{\hbar} S_{\Gamma}} = \int_a^b Dz(t) e^{i S_{\Gamma}/\hbar} \quad (4.13)$$

where  $N$  is a normalization constant. When the path,  $\Gamma$ , is far from the classical path,  $S_{\Gamma} \gg \hbar$  representing the classical limit, the phase term causes large oscillations. These large oscillations create a destructive interference between different paths. Only near the classical path does the phase term cause constructive interference between neighboring paths due to the extremal nature of the action near  $\Gamma_{cl}$ . In this way, quantum mechanics reduces to classical mechanics for  $\hbar \rightarrow 0$ .

#### 4.4.2 Quadratic Lagrangians

The problem simplifies under the assumption of a quadratic lagrangian:

$$L = a(t)\dot{z}^2 + b(t)\dot{z}z + c(t)z^2 + d(t)\dot{z} + e(t)z + f(t) \quad (4.14)$$

Since only points near paths near the classical path,  $\overline{z(t)}$  coherently contribute to the propagator, the expansion  $z(t) = \overline{z(t)} + \xi(t)$  can be used. This results in a propagator of the form:

$$K(z_b, t_b, z_a, t_a) = F(z_b, t_b, z_a, t_a) e^{i S_{cl}/\hbar} \quad (4.15)$$

	$ g\rangle$	$ e\rangle$
$ g\rangle$	$U_{g,g}$	$U_{e,g}e^{i(k_L z_1 - \omega_L t_1 - \phi)}$
$ e\rangle$	$U_{g,e}e^{-i(k_L z_1 - \omega_L t_1 - \phi)}$	$U_{e,e}$

Table 4.1: Atom-Laser interaction propagator matrix element.

where  $F$  is only a function of the initial and final points.

### 4.4.3 Perturbations

The path integral approach can also be solved by considering perturbations to the Lagrangian,  $L = L_0 + \epsilon L_1$ . It is still assumed the Lagrangian is quadratic; it is also required that  $\epsilon \ll 1$ . The phase of the final wavefunction is then found to be proportional to the integral of the perturbing Lagrangian over the classical path of the unperturbed Lagrangian. For a closed interferometer,

$$\delta\phi = \frac{\epsilon}{\hbar} \oint L_1 dt . \quad (4.16)$$

### 4.4.4 Atom-Laser Interaction Phase

The interaction between the atom and laser is next considered. A two level structure is assumed with a ground and excited state,  $|g\rangle$  and  $|e\rangle$ , respectively. The short pulse limit is used such that the transverse propagation through the beam can be neglected. Any interaction where the atom changes state is associated with a change of momentum,  $\pm\hbar k$ . After interaction with the light, the atomic wavefunction is modified by a multiplying factor (Table 4.1).

Here,  $k_L$ ,  $\omega_L$ , and  $\phi$  are the light wavevector, frequency and phase, respectively.  $U_{i,j}$  is the transition amplitude from state  $j$  to state  $i$ .

## 4.5 Free Particle with Gravity Example

A free particle in a gravitational field has a Lagrangian

$$L(z, \dot{z}) = \frac{1}{2}M\dot{z}^2 - Mgz . \quad (4.17)$$

The action from space-time point  $z_a, t_a \rightarrow z_b, t_b$  is formed using the classical equations of motion. In the case of our interferometer setup the action is evaluated for each path segment. With reference to Fig. 4.2, the propagation phase shift between the paths is found from the combination

$$\delta\phi_{path} = S_{cl}(AC) + S_{cl}(CB) - [S_{cl}(AD) + S_{cl}(DB)] = 0 . \quad (4.18)$$

In a uniform gravitational field the two wavepackets overlap at the end of the interferometer, therefore a relative phase shift associated with wavepacket separation is zero. For plane waves, this term is generally expressed as  $\delta\phi_{diff} = p_0\Delta x/\hbar$ .

The final term to consider is the phase evolution from the interactions of the wavepackets with the interferometer light. Along the path given by ACB, the laser interaction contribution is

$$U_{e,e}U_{e,g}e^{i[k(z_{C0}-\frac{1}{2}gT^2)-\omega T-\phi_2]}U_{g,g} , \quad (4.19)$$

while the contribution from path ADB is

$$U_{e,g}e^{i[k(z_{B0}-2gT^2)-2\omega T-\phi_3]}U_{g,e}e^{i[k(z_{D0}-\frac{1}{2}gT^2)-\omega T-\phi_2]}U_{e,g}e^{i[kz_{A0}-\phi_1]} . \quad (4.20)$$

Counterpropagating beams are used where  $k = k_1 - k_2, \omega = \omega_1 - \omega_2, \phi = \phi_1 - \phi_2$ <sup>1</sup>.

---

<sup>1</sup>Phase shifts arising from the interaction amplitude terms can be neglected as they are inde-



The position subscript denotes a gravity free path position. Using the geometry of the paths,

$$\delta\phi_{laser} = kgT^2 + \phi_1 - 2\phi_2 + \phi_3 \quad . \quad (4.21)$$

The total phase difference between the two interferometer arms is

$$\delta\phi_{tot} = \delta\phi_{path} + \delta\phi_{diff} + \delta\phi_{laser} = kgT^2 + \phi_1 - 2\phi_2 + \phi_3 \quad . \quad (4.22)$$

This solution can also be derived using the perturbative approach discussed above. Here, gravity is treated as a perturbation to the free particle Lagrangian. Giving  $g = 0$ , the laser phase term is

$$\delta\phi_{laser}^0 = \phi_1 - 2\phi_2 + \phi_3 \quad , \quad (4.23)$$

while  $\delta\phi_{diff}^0 = 0$  again, as the two path arms form a closed interferometer in the absence of gravity. Eq. 4.16 is used to obtain the path integral component of the phase shift:

$$\delta\phi_{path}^0 = -\frac{Mg}{\hbar} \oint_{A_0 C_0 B_0 D_0 A_0} z(t) dt = -\frac{Mg}{\hbar} \left( -\frac{\hbar k}{M} T^2 \right) = kgT^2 \quad . \quad (4.24)$$

Therefore, the total relative phase shift is  $\delta\phi_{tot} = \delta\phi_{path} + \delta\phi_{laser} = kgT^2 + \phi_1 - 2\phi_2 + \phi_3$ , which agrees with the above result (4.22).

---

pendent of  $g$  and the laser phases.

### 4.5.1 Gravity Gradients

When gravitational gradients are included, the three contributing terms of Eq (4.6) are nonzero. The Lagrangian describing this system is written as

$$L(z, \dot{z}) = \frac{1}{2}M\dot{z}^2 - mgz + \frac{1}{2}m\alpha z^2 . \quad (4.25)$$

Here,  $\alpha$  is the gravitational gradient at the surface of the Earth. In an expansion of the Earth potential, the linear gradient term is  $\alpha \sim 1.5 \times 10^{-7}g/m$ . This amounts to a change on the order of  $10^{-8}g$  through the fountain of a single atom interferometer accelerometer. The zero order phase shift from gravity is on the order of  $10^6$  radians, while the gravitational gradient contribution is approximately 0.01 radians for our typical interferometer time of  $T = 150ms$ .

The above influence of gravity gradients suggests that when using the perturbative approach, the gravity gradient is to be treated as a perturbation to the Lagrangian of a particle in a uniform gravity field

$$L_0(z, \dot{z}) = \frac{1}{2}M\dot{z}^2 - mgz \quad (4.26)$$

$$L_1(z) = \frac{1}{2}m\alpha z^2 . \quad (4.27)$$

In this approach,  $\delta\phi_{laser}$  is taken over the unperturbed trajectory and is given by Eq. 4.21. The path component of the phase shift is evaluated by integrating the perturbing Lagrangian,  $L_1$ , over the trajectory which includes the uniform gravitational field,  $g$  [34]:

$$\delta\phi_{path} = \frac{M\alpha}{2\hbar} \oint_{\Gamma_g} z(t)^2 dt = \alpha k T^2 \left( \frac{7}{12} g T^2 - \dot{z}_0 T - z_0 \right) . \quad (4.28)$$

Accounting for the finite separation of the plane waves at the end of the interferometer contributes a term:

$$\delta\phi_{diff} = -\frac{\hbar^2}{2m}T \ , \quad (4.29)$$

derived by integrating the acceleration of the two wavepackets over their respective paths while including the effect of the gravity gradient. The resulting path separation is used to obtain the above expression. The total relative phase is then:

$$\delta\phi_{tot} = kgT^2 + \alpha kT^2\left(\frac{7}{12}gT^2 - \dot{z}_0T - z_0 - \frac{\hbar^2}{2m}T\right) \ . \quad (4.30)$$

The full path integral approach can be used and solved analytically. Taylor expanding the full solution to first order in  $\alpha$  gives an expression identical to the perturbative answer obtained above.

## 4.6 Cylindrical Potential Phase Shift

Chapter 8 details the measurement of the Newtonian gravitational constant,  $G$ . Detailed below is the path integral theory applied to the source mass potential used in the experiment. Phase shift measurements were performed and combined with data on the geometry of the source mass and source-test mass dimensions, a fit on the remaining free parameter determined the gravitational constant.

### 4.6.1 Lead Cylindrical Potential

The longitudinal axis of the lead source mass cylindrical potential was colinear with the interferometer propagation axis. Axial symmetry allowed us to ignore contributions from the transverse components of the potential. The remaining on axis

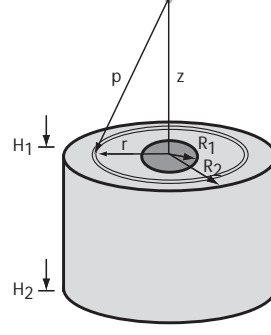


Figure 4.3: Pb source mass diagram.

contribution can be expressed by

$$U_z = -G \frac{dm}{\varrho} = -2\pi G \rho \int_{H_1-z(t)}^{H_2-z(t)} \int_{R_1}^{R_2} \frac{z(t)}{\sqrt{z^2 + r^2}} dz dr , \quad (4.31)$$

obtained by integrating over the cylindrical disc of mass density,  $d\rho$ , over the height of the cylinder,  $H_2 - H_1$  and the radial thickness,  $R_2 - R_1$ . The position of the test mass is a function of time,  $z(t)$ , since the atoms are launched in a fountain.

The full action of the Cs test mass is written as:

$$S_{path} = \frac{1}{\hbar} \int_{t_a}^{t_b} \left[ \frac{1}{2} m \dot{z}(t)^2 - mgz(t) + \frac{mg}{R_E} (z(t) - R_E)^2 + 2\pi G \rho \int_{H_1-z(t)}^{H_2-z(t)} \int_{R_1}^{R_2} \frac{z(t)}{\sqrt{z^2 + r^2}} dz dr \right] dt , \quad (4.32)$$

where  $R_E$  is the radius of the Earth and the action is integrated over a path segment,  $\bar{ab}$  from time  $t_a$  to  $t_b$ .

The resultant path integral phase shift is then determined by following Eq. 4.10. The atom-light interaction phase shift is found using Table 4.1 with the position determined from the full equations of motion. The separation phase shift of the wavepackets at the end of the interferometer is negligible in comparison to the other two phase shifts.

# Chapter 5

## Apparatus

### 5.1 Apparatus Overview

The apparatus described here is that in Ref. [39], but several changes have been made in order to achieve the current sensitivity. The gradiometer consists of two laser cooled and trapped sources of Cs atoms. The atoms are launched on ballistic trajectories and prepared in the  $m_f = 0$  first order magnetic insensitive state with optical and microwave techniques before the interferometer sequence. Following the interferometer sequence, atoms are detected in a low noise configuration using a normalizing detection method with a modulation transfer technique.

### 5.2 Vacuum Chamber

Preparation of the vacuum chambers is described in detail in [22], with the key components detailed here. Two identical vacuum chambers are used in the gradiometer, one for each gravimeter, continually pumped by ion pumps at a base pressure of  $\sim 10^{-9}$  torr.

The vacuum chambers were machined completely out of aluminum in 4 parts, all

joined by brazing. The main interaction zone is a 14-sided polyhedron, each with a machined through hole. Two aluminum tubes were brazed on opposing viewports to accommodate launching of the atoms. Six of the viewports are used for delivery of the molasses trapping light. A long aluminum tube is brazed onto a single face leading to the vacuum pumping station. The remaining viewports are used for optical access and delivery of microwave fields, detection light, and cesium atoms. Each viewport has a dimension of 1.5", with the exception of the raman ports at 3".

A cesium reservoir is attached to each chamber, consisting of a 5 g ampoule. The cesium station is attached to the chamber as follows. The ampoule is placed inside a metal tube that is attached to a glass tube. Before the cesium ampoule is broken open, this assembly is pumped down with a turbo molecular pump and baked at  $\sim 200^\circ \text{C}$  to desorb gasses from the walls. After pumping, the assembly is sealed off and the ampoule is broken. The glass cell is temperature controlled to  $\sim -30^\circ \text{C}$ , forming a cold finger, while the rest of the assembly is heated forcing the cesium atoms to accumulate in the cold finger. This process lasts for a few days, at which point all of the atoms have accumulated in the cold finger. The Cs cold finger is then valved off and attached to the vacuum chamber.

Initially, we had placed the cesium source near the ion pump, far from the central chamber, to help limit the amount of background cesium vapor contaminating the experiment. However, the proximity to the ion pump decreased the pump's lifetime to about six months. Now, the cesium source is attached to one of the viewports on the main chamber, increasing the lifetime of the pumps. To further increase the pump lifetime, the long aluminum tube connecting the pump to the main chamber was coated with graphite to adsorb Cs atoms.

The chamber is first evacuated with a turbo-molecular pumping station near the end of the long aluminum tube. The aluminum parts of the chamber are heated

at  $\sim 100^\circ \text{ C}$ , below the  $\sim 160^\circ \text{ C}$  melting point of the indium seal used on the viewport windows, while the steel parts are heated at  $\sim 250^\circ$  for about one week to desorb elements from the chamber walls. This bakeout occurs during the pump down process. Following the bakeout process, the ion pump is activated. The ion pumps are 25  $l/s$  noble diode pumps (Varian 9115050), attached to the end of the long aluminum tube. The base pressure will drop to about  $5 \times 10^{-10}$  torr, according to the ion pump current<sup>1</sup>. A steady state base pressure of  $\sim 1 \times 10^{-9}$  torr is reached over several weeks, with the rise due to gases, i.e. helium, permeating through the aluminum walls and glass windows.

The cold finger is brought to  $\sim 10^\circ \text{ C}$  and valved open to the chamber. The Cs partial pressure builds for about a day while adsorbing into a monolayer on the chamber wall. Adjustments of the Cs partial pressure are controlled by way of a valve between the vacuum chamber and the Cs cold finger.

### 5.3 Laser Cooled Atomic Sources

Each gravimeter consists of an ultra-high vacuum system with a Cs source which maintains a  $10^{-9}$  torr Cs vapor pressure for a magneto-optical trap (MOT). The lasers are delivered to the vacuum chambers via optical fibers from a common high-power, frequency stable laser system. The trapping laser beams are configured in the six beam [1,1,1] geometry (3 mutually orthogonal pairs) which allows clear access for the Raman interferometer and detection pump beams along the the vertical axis.

In order to obtain good interferometer signal-to-noise ratios (SNRs), it is critical to load atoms quickly into the MOTs in such a way as to minimize atom number fluctuations during the loading process. A grating stabilized diode laser (New Focus

---

<sup>1</sup>Ion pump currents are not a reliable measure of pressure below  $10^{-9}$  torr

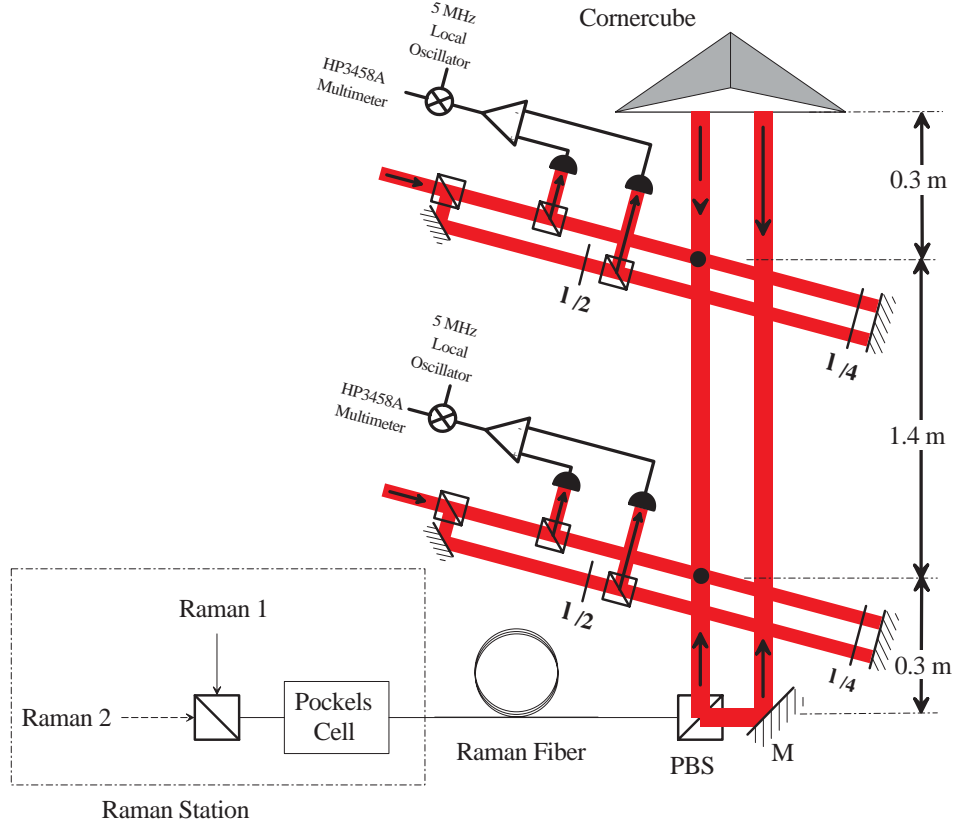


Figure 5.1: Schematic of the gravity gradiometer. Shown are the propagation paths for the detection pump beam (vertical through the chambers) and probe beams (nearly orthogonal to the pump beam). The Raman beam bath is collinear to the pump beam. A corner-cube retroreflector is used to create a racetrack configuration for the Raman light: The on-axis light contains the near resonant Raman 2 photon  $\sigma^+ - \sigma^-$  light while the off-axis contains the far detuned orientation.

Vortex) serves as the master laser for the trapping system. The extended cavity of the Vortex laser gives it an intrinsic linewidth of approximately 300 kHz. The Vortex laser is locked to the Cs  $F = 4 \rightarrow F' = 3/5 + 60\text{MHz}$  transition via standard saturation spectroscopy techniques in a Cs cell. The locked laser has a stability of 1 kHz/Hz<sup>1/2</sup>. The more stable master laser reduces frequency induced noise and the shot-to-shot root mean square (rms) atom number fluctuations of the MOTs by a factor of five to a SNR of 200:1 as compared to a previously used distributed Bragg reflector (100mW SDL-5712) laser locked to the same transition. The typical free



running linewidth of the DBR laser was 3MHz.

The master laser light originated from a lock setup located in a neighboring laboratory, stabilized 60 MHz to the blue of the  $F=3 \rightarrow F'=3/5$  transition, and then delivered to our experiment by a 20m optical fiber. This light was then frequency shifted down by 30 MHz before injection locking a 150mW laser (SDL 5422-H1) [40, 41]. The output of the slave laser carries the frequency stability of its master laser. This light is then split into two acousto-optic modulators (AOM's) in a double pass configuration. These AOM's are used for frequency shifting the light used in the polarization gradient cooling and atomic launch. The double pass configuration allows frequency tuning without deflection of the laser light. After the AOM double pass stage, each light injection locks a corresponding slave laser diode.

At this point, the output of each of the two secondary slave lasers passes through an AOM used to frequency shift the light to within 10 MHz to the red of the cooling  $F=4 \rightarrow F'=5$  transition it is then delivered to the vacuum chamber by way of polarization maintaining optical fibers. The two lasers comprise the upward and downward propagating molasses light for a single gravimeter chamber. The same light for the other gravimeter chamber is derived from optical isolator rejection light from each of the two secondary slave lasers, respectively injection locking another slave laser.

In a previous version of this experiment the master laser injection locked two amplifier lasers which then seeded two 500 mW tapered amplifier lasers (SDL 8630E). Each tapered amplifier laser was split into six equal outputs to provide the twelve trapping beams for the two MOTs. However, the tapered amplifiers suffered from pointing instability, causing intensity fluctuations of as much as 10% of the laser power at the MOT over a 1 day period, along with a typical lifetime of  $\sim 6$  months.

In the current setup fiberoptic splitting is accomplished using robust and compact

free-space fiber optic beamsplitters (Optics for Research FiberBench). The stability of the fiber mounts maintains the splitting ratio to greater than 1% over many months with no adjustment, with a fiber to fiber coupling efficiency of  $\sim 75\%$ .

The fibers are polarization maintaining with an extinction ratio of greater than 30 dB. Polarization stability is further maintained with the use of clean-up polarizing optics at the output of the fibers (converting polarization drift in the fiber to negligible intensity fluctuations). The intensity and polarization stability of the MOT trapping beams contribute greatly to the reduction of trapped atom number fluctuations. The trapping beams from the twelve fibers propagate uncollimated to the two MOTs. By not collimating the beams, we are able to circumvent the windows aperturing the beam size at the center of the trap. Larger beam waists in the loading region lead to higher atom loading rates. The approximate beam waist at the trapping position is 2.5 cm ( $1/e^2$ ), and the intensity is about  $1.2 I_{sat}$  per beam ( $I_{sat} = 1.12 \text{ mW/cm}^2$  for the Cs cooling transition). In this configuration, each MOT loads approximately  $2 \times 10^8$  atoms in 1 s.

After loading the MOTs from a thermal vapor for 1.0688s, the cold atoms are launched in ballistic, atomic fountain trajectories. The launch is initiated by continuously increasing the detuning of the MOT beams from -10 MHz to -20 MHz from the cooling transition. Next, the trapping quadrupole magnetic fields are turned off, and the atoms are held in the far detuned optical molasses for at least 30 ms while the eddy currents from the field switching damp out<sup>2</sup>. A controlled ramp down of the magnetic quadrupole field reduces the effect of eddy currents. For each MOT, following this holding period, the frequency of the upper three molasses beams is acousto-optically ramped down by 1 MHz over 5 ms while the frequency of the lower

---

<sup>2</sup>The vacuum chambers were made of aluminum, to reduce the presence of static magnetic field gradients. Aluminum has a much higher electrical susceptibility than stainless steel. Titanium or all glass quartz or Zerodur are other potential alternatives to steel.

three beams is ramped up by an equal amount. This frequency ramp smoothly transfers the atoms to an optical molasses moving vertically at  $\sim 1.5$  m/s. After this ramp, the mean frequency of the trapping beams is ramped down to -40 MHz detuned (still in a moving molasses) over 5 ms, and then the intensity is ramped down to half intensity in 1 ms, held for 0.5 ms, and ramped completely off in an additional 0.5 ms. These ramps cool the atoms to  $\sim 2.3$   $\mu$ K, as measured from the widths of velocity selective stimulated Raman transitions between  $F=3$  and  $F=4$ . The frequency and intensity ramps are accomplished using digitally synthesized waveforms from Hewlett Packard HP8770A arbitrary waveform generators (AWGs).

Following this launching and cooling phase, the cold atoms move in a 320 ms, 12 cm high fountain during which they are prepared in the  $m_f = 0$  state and then interrogated by the interferometer sequence. In a subsequent experiment (Chapter 5) the atoms were launched in a 140ms, 3cm tall, fountain.

## 5.4 State Preparation

Before the atom interference pulse sequence is initiated, a state selection sequence prepares the atoms in the magnetically insensitive  $m_f = 0$  sublevel and velocity selects an atomic ensemble with a velocity spread of temperature  $\sim 2.3\mu$ K (or  $\sim 2$ cm/s) which is matched to the velocity selectivity of the Raman pulse sequence. This state selection, which is accomplished with a sequence of microwave and optical pulses, is important for obtaining high fringe contrast. The details associated with this state selection are discussed below.

Following their launch, atoms are initially distributed among the magnetic sublevels of the  $F = 4$  ground state. Three orthogonal pairs of magnetic field coils, roughly in a Helmholtz configuration, zero the Earth's magnetic field and apply a

vertical bias field of  $\sim 100$  mG, causing a first order Zeeman shift<sup>3</sup>[42] of

$$\Delta\nu = m_f \times 700.8 \text{ kHz/G} . \quad (5.1)$$

This bias allows selective addressing of individual  $F = 3$  to  $F = 4$  ground state magnetic sublevel hyperfine transitions (i.e.  $|3, 0\rangle \leftrightarrow |4, 0\rangle$ ) with a 9.2 GHz microwave field (delivered to the atoms through a Narda 640 X-band gain horn).

First, a microwave composite  $\pi$  pulse[43] transfers atoms from the  $F = 4, m_f = 0$  to the  $F = 3, m_f = 0$  sublevel. Composite pulse sequences accomplish the population transfer associated with ideal  $\pi$  in an experimentally robust way, as described in the subsection below. Next, a near-resonant pulse from the upper trapping beams tuned slightly above the  $6S_{1/2}, F=4 \rightarrow 6P_{3/2}, F'=5$  transition clears atoms in the remaining  $F = 4$  sublevels (via the scattering force). Another composite microwave  $\pi$  pulse then returns  $F = 3, m_f = 0$  atoms to  $F = 4, m_f = 0$ . An optical velocity selective Raman  $\pi$  pulse is then applied which transfers  $F = 4, m_f = 0$  atoms within the velocity range encompassed by the Raman pulse envelope to  $F = 3, m_f = 0$ . Finally, a second, near resonant, blue detuned pulse clears away the remaining  $F = 4$  atoms. At this point, the state prepared atoms are ready for use in the interferometer.

A considerable fraction of atoms are eliminated from the initial ensemble in this process:  $\sim 8/9$  from the internal state selection and another  $\sim 2/3$  in velocity selection, leaving roughly 4% for the interferometer.

#### 5.4.1 Microwave Generation

The generation and delivery of the 9.2 GHz microwave field is briefly described here. The microwave field is coupled to the atoms through radio-frequency (RF) horns

---

<sup>3</sup>The  $m_f = 0$  second order Zeeman shift is  $\Delta\nu^{(2)} = 427.5 \text{ Hz/G}^2$ .

attached to viewports on the MOT chambers. The microwave frequency is tied to a 10 MHz reference, temperature stabilized, master crystal oscillator (Oscilloquartz OCXO, stability of  $1.4 \times 10^{-13}$  in 1 s). The reference oscillator drives a 100 MHz phase locked oscillator (PLO, Wenzel 500-0732) which is the input to a Microlambda (MLPE 1162) 9.2 GHz PLO. The RF is mixed in a single sideband mixer with an  $\sim 7.4$  MHz signal from an arbitrary waveform generator (AWG) which is also phase locked to the reference oscillator. The AWG is used to scan the RF frequency and phase. The mixer output is amplified up to  $\sim 1$  W and sent to the horns. The RF power is controlled by the AWG output, and the relative power to the two chambers can be adjusted with appropriate attenuation in the two paths.

We perform a microwave  $\pi/2$  -  $\pi/2$  clock experiment as a diagnostic to check the phase noise performance of our oscillators and the noise performance of our detection system. We have shown that we can detect microwave clock fringes with 1000:1 SNR using our normalized detection [32]. This SNR is at the atom shot noise limit for our fountain with no velocity selection ( $\sim 10^6$  atoms/shot).

### 5.4.2 Composite Pulse Techniques

The state preparation methods work best with efficient coherent population transfer between  $F = 3$  and  $F = 4$  states. Less than unit transfer efficiency during a standard  $\pi$  pulse between the ground states can result from an inhomogeneous Rabi frequency of the microwave or optical pulse seen by the atoms, as well as by detunings due to the velocity spread of the atoms. In the gradiometer, the microwave  $\pi$  pulses are typically only 80% efficient due to inhomogeneous field strengths across the atom clouds<sup>4</sup>. Furthermore, the state selection and optical pumping require a series of one optical and four microwave  $\pi$  pulses in the two separate chambers. With the current

---

<sup>4</sup>The microwave transitions are driven with horns located outside the vacuum chamber

system of a single microwave source split between the two chambers, it is difficult to match the pulse conditions for all pairs of pulses due to different microwave intensity gradients in each chamber.

In composite pulse sequences[43], a standard  $\pi$  pulse is replaced with a sequence of pulses with variable area and relative phase. In our work, we employ a consecutive  $\pi/2 - \pi_{90^\circ} - \pi/2$  pulse sequence in place of a  $\pi$  pulse. The subscript  $90^\circ$  indicates that the phase of the center  $\pi$  pulse is shifted  $90^\circ$  relative to the  $\pi/2$  pulses. The use of this sequence increases the transfer efficiency of a pulse for inhomogeneous distributions of Rabi frequency and detuning across the atomic ensemble. Employing these pulses for the microwave state preparation pulses increases the transfer efficiency from 80% with a regular  $\pi$  pulse to 95%.

Composite pulses may be applied to optical pulses as well. However, at our detuning from the  $6^2P_{3/2}$  manifold, the increased exposure to Raman light increases spontaneous emission and hence results in a loss of contrast.

### 5.4.3 Enhanced Optical Pumping

In order to increase the  $m_f = 0$  population, an enhanced optical pumping scheme was briefly utilized. This method recycled atoms which were not initially in the  $m_f = 0$  target state via an optical pumping sequence. In practice we have seen as much as a factor of 3 improvement in usable atoms with this method, with typical conditions at  $\times 1.5$ -2 improvement.

First, a composite microwave  $\pi$  pulse is applied to drive atoms from the  $F = 4$ ,  $m_f = 0$  to the  $F = 3$ ,  $m_f = 0$  state as before. Then a de-pumping beam tuned to the  $F = 4$  to  $F' = 4$  transition is applied to optically pump the remaining atoms from  $F' = 4$ , all  $m_f$ , to  $F = 3$ . The de-pumping process redistributes the atomic population, with approximately  $1/7$  of the remaining atoms ending up in  $m_f = 0$ . The process is

then reversed with a composite microwave  $\pi$  pulse transferring  $F = 3, m_f = 0$  to  $F = 4, m_f = 0$ . A repumping beam is then applied to the  $F = 3$  to  $F' = 4$  transition. In principle, this entire sequence could be repeated many times, resulting pumping efficiency approaching 100%.

In practice, inefficiency of the microwave pulses, heating due to spontaneous emission in the pumping sequence, and the availability of only a finite amount of time to execute the sequence limit the process efficiency.

For vapor cell loaded traps, the overall efficiency is also limited by the presence of the background atomic vapor. In this case, the de-pumping photons can excite atoms in the background vapor which then emit light at the repumping frequency. These rescattered photons then redistribute atoms in the  $F = 3, m_f = 0$  state to other  $m_f \neq 0$  states substantially increasing shot-to-shot atom number fluctuations (from 200:1 to 60:1). Thus there is a trade-off between background vapor pressure (which sets the loading rate) and the overall efficiency of the scheme (which works best at low vapor pressure).

## 5.5 Atom Interferometer

Following its launch and state preparation each atom ensemble is subject to the  $\pi/2 - \pi - \pi/2$  interferometer pulse sequence. Experimental details of Raman laser frequency control and delivery is presented. The detection system is presented later in Chapter 6.

### 5.5.1 Raman Lasers

In order to achieve high frequency stability of the Raman laser beams, a second Vortex (external cavity, grating stabilized) laser is used as the master laser for the

Raman laser system. This laser is locked to the  $6S_{1/2}$ ,  $F = 3 \rightarrow 6P_{3/2}$ ,  $F' = 2$  crossover resonance (via modulation transfer spectroscopy) using several AOMs to offset the frequency to obtain the desired detuning. The lock was maintained through the use of a digital signal processor (DSP, Spectrum Signal Indy TMS320C32). The DSP processes the lock error signal through a highpass and lowpass channel, each operating at a sampling rate of 25 kHz. The high and low frequency channels provide feedback to the laser current and to the cavity piezo element respectively. Due to the presence of long term drift in the piezo element a third, very low frequency channel is provided through a GPIB command to the laser controller. The measured stability of the laser is comparable to that of the master laser used for the optical molasses (and is primarily limited by a 5 kHz resonance of the laser's piezo-electric transducer). This was later replaced with a proportional and integral electronic feedback circuit, identical to that used in the molasses Vortex laser lock. The frequency stability was also similar to that obtained with the molasses lock.

The Vortex laser directly injection locks a 150 mW slave diode laser. This laser is then shifted up and down in frequency by 4.756 GHz (HP83711A)(160 MHz above half the Cs clock frequency) with a high frequency AOM (Brimrose GPF-4600-300-X, 0.1% efficiency). The  $\pm 1$  diffracted orders then injection lock two more 150 mW slave laser diodes at a frequency 688.2 MHz red detuned from the  $F = 3 \rightarrow F' = 4$  and  $F = 4 \rightarrow F' = 4$  transitions, respectively [37]. The frequency noise on the master Raman laser exists on both the slave lasers, but their frequency separation remains fixed at the Cs ground state hyperfine transition. The detuning from the  $6^2P_{3/2}$  hyperfine levels reduces the effect of spontaneous emission due to off-resonant single photon excitations from each Raman beam.

In our excitation geometry, the two ensembles are separated by  $\sim 1.4$  m. The Raman fields propagate in an asymmetric way to these ensembles. To see this,



consider the propagation paths of the optical fields following the beam dividing optic which separates the two Raman fields. The beam of frequency  $\nu_1$  propagates roughly  $x_1^1 \approx 0.3$  m before it passes through the first ensemble of atoms, while it propagates roughly  $x_1^2 \approx 1.7$  m before it passes through the second ensemble. On the other hand, the beam of frequency  $\nu_2$  propagates  $x_2^1 \approx 3.7$  m before it passes through the first ensemble, while it propagates  $x_2^2 \approx 2.3$  m before it passes through the second ensemble.

If the frequency of the lasers drifts on a time scale short compared to the interrogation time  $T$  between pulses, this can cause an asymmetric phase shift to be read into the atomic coherences due to this path asymmetry. For example, suppose the laser frequency jitter is  $\delta\nu$ , while the differential path length travelled by the Raman lasers for the two ensembles is  $\ell \equiv (\text{effective path to ensemble 1}) - (\text{effective path to ensemble 2}) = (x_2^1 - x_1^1) - (x_2^2 - x_1^2) \simeq 2.8$  m. This leads to a differential phase noise of  $\delta\phi_{laser} \sim (k\ell)(\delta\nu/\nu)$ . For a target interference SNR of 1000:1,  $\delta\phi_{laser} \leq 1$  mrad. For our parameters, this implies a requirement of  $\delta\nu \leq 20$  kHz, which is satisfied by the Vortex lock.

## 5.5.2 Raman Beam Delivery

The Raman beams are delivered to the vacuum chambers with a polarization maintaining optical fiber in order to increase the pointing stability of the Raman beams as well as to spatially filter them. Prior to coupling into the fiber, the two Raman beams are double-passed through 80 MHz AOMs. These AOMs are controlled by another HP8770 AWG which allows dynamic frequency, phase, and intensity tuning of the Raman beams during the interferometer pulse sequence. During the interferometer, the frequency of the Raman lasers must be phase continuously chirped in order to maintain a resonance condition with the accelerating, Doppler shifting,

atoms.

The two Raman beams are overlapped with orthogonal linear polarizations on a polarizing beamsplitting cube and passed through a Pockel's cell polarization modulator (ConOptics 350-50) after the double-passed AOMs. The Pockel's cell is used to reverse the effective Raman laser propagation direction. A technique to reduce many systematic interferometer phase shifts involves reversing the effective Raman propagation vector  $\mathbf{k}_{\text{eff}} = \mathbf{k}_1 - \mathbf{k}_2$ . Because the gravitational phase shift is proportional to  $\mathbf{k}_{\text{eff}} \cdot \mathbf{g}$ , reversing the sign of  $\mathbf{k}_{\text{eff}}$  changes the sign of the gravitational phase shift. However, several systematic phase shifts, such as second-order Zeeman shifts from magnetic fields and any residual AC Stark shifts, have no dependence on the Raman wavevector direction. Subtracting the phases obtained from consecutive experimental cycles using two reversed propagation directions gives twice the gravitational phase shift, but removes these systematic shifts. The propagation reversal is accomplished with the Pockel's cell (ConOptics 350-50). The Pockel's cell rotates the polarization of both Raman beams by  $90^\circ$  when activated with a high voltage source. This rotation causes the direction the Raman beams take through the racetrack to switch, *i.e.*  $\mathbf{k}_{\text{eff}} \rightarrow -\mathbf{k}_{\text{eff}}$ . A potassium dideuterium phosphate crystal comprises the optical element in the Pockel's cell with a half-wave voltage of  $757\text{V}$ <sup>5</sup>. The cell provides a 700:1 extinction ratio.

The Raman beams then are coupled into a polarization maintaining fiber with 75% efficiency and sent to the gradiometer. For wavefront quality, after the fiber the Raman beams are collimated from the fiber output with a 1.1 cm focal length aspheric lens (Thorlabs F220FC-B) and a high surface quality 50 cm focal length spherical lens (CVI PLCX-50.8-257.5-C). This lens combination results in a uniform

---

<sup>5</sup>The half-wave voltage is the required potential to cause a  $\pi/2$  rotation in the polarization direction of the laser beam.

phase front for the Raman beams. After collimation the Raman beams have a 1.0 cm (1/e) beam waist. All optics in the Raman beams' propagation path after the optical fiber are of high surface figure ( $\lambda/10$  or better) in order to preserve the phase front homogeneity of the Raman beams. Phase front quality was measured with a Melles-Griot (09SPM005) shear plate to within  $\lambda/10$ .

After collimation, the Raman beams enter a racetrack geometry, enabling us to obtain counterpropagating beams for the Raman interaction. The racetrack configuration starts with a polarizing beamsplitter cube that separates the two orthogonally polarized Raman beams. The two Raman beams then parallel propagate vertically through the vacuum chambers with one beam passing through the axis of the atom ensembles and the other 2 cm off-axis. After the two Raman beams have passed through both chambers, a corner cube retroreflector (Edmund-Scientific A46-187  $0.24\lambda$ ) redirects the off-axis Raman beam to counterpropagate with the on-axis Raman beam, resulting in two counterpropagating beams. The use of the corner cube decreases the tilt sensitivity of the apparatus, to within 1 arc-second, by keeping the Raman beam propagation axis constant as the cube is subjected to spurious tilts. In this racetrack, standing waves are eliminated, which ensures overall intensity stability by suppressing etalon effects from the Raman beams. Also, spontaneous emission is reduced by half in a corner cube system as compared to a system using collinear retroreflected beams.

### 5.5.3 Raman Beam Parameters

A finite Raman beam has a Gaussian profile, causing a spatially inhomogeneous Rabi frequency across the atom cloud. Similarly, the velocity spread of the atoms along the Raman beams causes inhomogeneous broadening due to differential Doppler shifts across the atom ensemble. This results in dephasing during the fountain leading

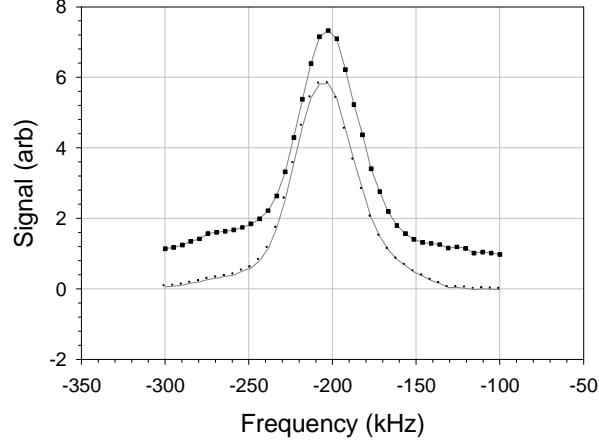


Figure 5.2: Typical scan over the two photon Raman transition used in the velocity selection sequence. Shown are the traces for each chamber. The horizontal axis is an artifact of frequency offset from the hyperfine transition of the applied RF from the waveform generator.

to a limit on the interferometer contrast. Typical Rabi frequencies are around 30 kHz, and the initial width of the thermal spread of the atom ensemble is about 45 kHz. For the finite beam size and the initial atomic velocity distribution function we found an optimal 35% contrast limit for our operational Raman beam waist of 1.0 cm radius ( $1/e$ ) and detuning of 939.6 MHz from  $F' = 5$ .

AC Stark shifts from the Raman pulses themselves cause spurious phase shifts and spontaneous emission in the interferometer if unconstrained. However, with a two-photon Raman transition, the AC Stark shift is the difference between the individual AC Stark shifts from each beam and can be zeroed by adjusting the ratio between the two Raman beams. The Stark shift is balanced with a beam intensity ratio of  $\sim 1.6:1$  for the chosen Raman detuning. The Stark shift is balanced by inserting off-resonant Raman pulses within a microwave  $\pi/2 - \pi/2$  interferometer and adjusting the Raman beam intensity balance to zero the optically induced phase shift. The obtained ratio of 1.6:1 for the chosen Raman detuning agrees well with theoretical predictions.

### 5.5.4 Interferometer Operation

The gradiometer is typically operated in its most sensitive configuration with the interferometer pulses at a spacing of  $T = 150$  ms. This time is limited by the vacuum chamber size which constrains the fountain height to 12cm. The center  $\pi$  pulse is offset from the fountain peak by a few ms to avoid driving Doppler free (velocity insensitive) transitions from residual off axis light. Following the three-pulse interferometer sequence, the population distribution of the atoms in each ensemble is measured in a low noise normalized balanced detection scheme. In order to extract the gravitationally-induced phase shift, the phase of the final interferometer pulse is scanned digitally with the AWG controlling the phase and frequency of the RF waveform applied to the low frequency AOMs in the Raman beam paths. This phase scanning is in addition to the frequency chirp applied during the fountain.

## 5.6 Vibration Isolation Subsystem

At the most sensitive gradiometer operation, vibration phase noise is large. A method of data analysis was constructed which inherently suppresses common vibration induced phase noise (Chapter 7). Previously, a vibration isolation system was constructed to remove most of the vibration-induced phase noise from the interference fringes. With this reduction in phase noise, a least squares fit algorithm can be used to analyze the data.

### 5.6.1 Mechanical Design

The primary object in the instrument that must be isolated from vibrations is the Raman beam corner cube. All other optics are positioned so that any vibrations Doppler shift the two Raman beams in a common way, and the Raman difference frequency

remains unchanged. The Raman beam corner cube retroreflector is mounted on a Newport sub-Hertz platform (SHP) which provides the principal vibration isolation. The SHP is guided by a linear air bearing (New Way S4010002) along the vertical axis. The SHP provides isolation in the range of 0.5 Hz - 40 Hz. An accelerometer (Teledyne Geotech S-510) is mounted on the SHP to monitor platform accelerations. The corner cube is attached to the platform by a stack of two pieces of 1 in. thick lead filled acoustic foam separated by a 0.5 in. thick sheet of aluminum. The double stack of acoustic foam reduces vibrations of 30 Hz and higher by more than 20 dB. A linear voice coil actuator provides active feedback to the SHP.

### 5.6.2 DSP Servo System

Here we describe the active servo system for the SHP platform, which is similar to the servo algorithm used in [44]. The active feedback loop begins with the accelerometer to monitor vibrations. The accelerometer output is processed by a DSP (Spectrum Signal Indy TMS320C32), which we use to filter digitally the accelerometer input (as described below) and generate the feedback error signal. The feedback signal, after being buffered by a voltage amplifier, closes the feedback loop by driving the voice coil mounted between the SHP and the platform support. We apply the following digital filters in processing the accelerometer signal. First, a lag filter with a bandwidth of 1 Hz to 80 Hz rolls off the feedback below the accelerometer's 100 Hz high frequency cut-off. Next, a second lag filter with identical bandwidth is used to make the gain roll-off second order. Finally, two lead filters are applied to keep the system from oscillating at low frequency near the closed-loop SHP resonance of 0.03 Hz, which is also close to the internal highpass frequency of the accelerometer. The two lead filters have bandwidths of 38 mHz - 200 Hz and 380 mHz - 200 Hz respectively. The total gain of all four filters is 1600.

Using this servo, we are able to reduce the vibrations to near the noise floor of the accelerometer ( $10^{-8}$  g/Hz<sup>1/2</sup>) over a bandwidth of 40 mHz - 25 Hz. Higher frequencies are passively attenuated by the acoustic foam. With the addition of the vibration isolation system, phase noise from accelerations of the corner cube is reduced to less than 1 rad, and least squares sinusoidal fits may be performed on the fringes for the longest interrogation times.

# Chapter 6

## Instrument Readout and Performance

### 6.1 Introduction

Recent progress in the development of cold atomic fountain instruments indicates their potential scientific and technological impact. Atomic fountain clocks [45], gravimeters [4] and gravity gradiometers [39] now define or compete favorably with the state-of-the-art in their respective measurement classes. The operation of each of these instruments hinges upon low noise detection of ultra-cold atoms. Presented here is a sensitive detection technique based on a combination of balanced detection and modulation transfer spectroscopy [46] which has achieved a signal-to-noise ratio (SNR) of greater than 2000:1 in a cold atomic fountain [32]. This method is immune to laser frequency and amplitude noise and can be used when the cold atom signal competes with spurious signals arising from a thermal background atomic vapor.

Balanced detection makes use of the fact that all of the cold atom fountain experiments listed above require detection of atoms in a coherent superposition of



two internal atomic states following an atom interferometer, *i.e.* detection of population differences. Detection of population differences allows for a common-mode suppression of technical noise sources arising from laser amplitude and frequency noise. In the method described below the two states were spatially separated using light induced forces, which also projected the coherent superposition onto a statistical mixture of atoms in each of the two states. After the spatial separation, the absorption of two near resonant probe beams (each derived from the same laser) was measured on a balanced photodetector (where the photocurrents from two matched photodiodes were subtracted before amplification). In the case of equal populations between the two atomic states, this simultaneous differential detection produced a null signal, with high immunity to frequency or intensity noise from the laser.

In addition, we employed a modulation transfer technique to further suppress technical noise sources. A near resonant FM pump beam and a probe beam were overlapped on the cold atom cloud. The FM pump beam modulated the complex index of refraction of the atoms, which caused a modulated absorption of the probe beam [46, 47] that was detected on a photodetector and mixed down to DC. The pump and probe beams were aligned to be nearly orthogonal. This provided a Doppler selectivity to atoms at or near rest velocity, thus rejecting spurious signals from a background thermal vapor (which were Doppler shifted out of resonance with the pump and/or probe beams). Furthermore, transfer of the residual amplitude modulation (RAM) on the pump beam to the probe beams was a second order effect and should have been reduced to less than  $10^{-10}$ . Any residual signal arising from the thermal vapor signal was rejected by the balanced detection method described in the previous paragraph.

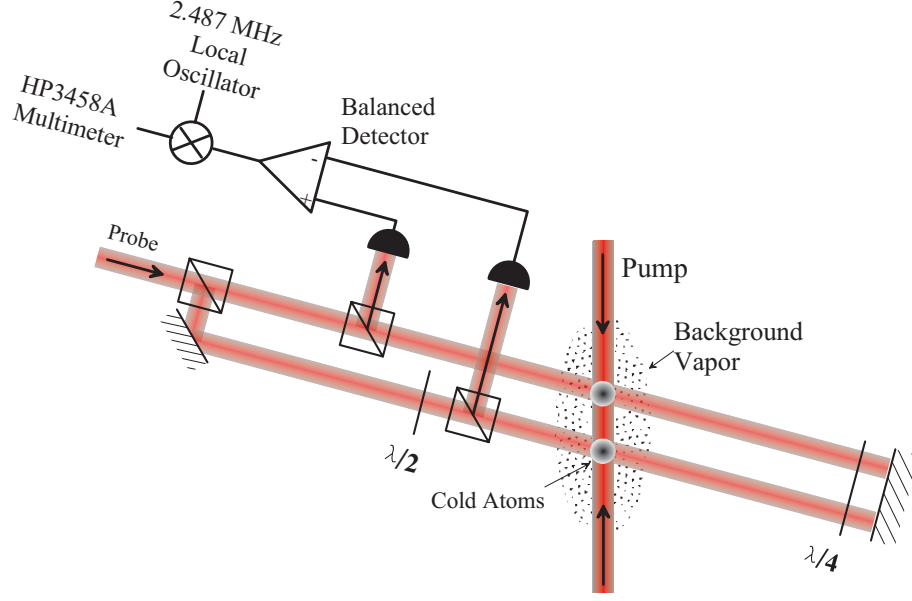


Figure 6.1: Diagram of the detection apparatus with two parallel probe beams for balanced detection and orthogonal pump beam for modulation transfer. The probe beams were detected on a balanced detector, mixed down to DC with a local oscillator (LO) and integrated on a low-noise digital voltmeter (DVM). All cubes are polarizing beamsplitters

## 6.2 Detection System

We demonstrated balanced, modulation transfer detection using our Cs atom interferometer gravity gradiometer apparatus [32]. The pump and probe beams were derived from two free running diode lasers injection locked to a single grating stabilized diode laser, which was locked to a spectral line at 852 nm in a Cs cell with standard FM spectroscopy techniques. The pump beam was modulated using an electro-optic modulator (EOM) placed before the injection-locked laser to reduce residual amplitude modulation. The pump and probe beams were switched into polarization maintaining optical fibers using acousto-optic modulators (AOM) and delivered to the detection region. In order to be matched to the atom cloud size, each beam was collimated to 7 mm diameter ( $1/e^2$ ) with the pump beam propagating vertically through the vacuum chamber collinear with the Raman beam path, orthogonal to

the two vertically separated (by 2.5 cm), horizontally propagating, probe beams (Fig. 6.1). The exact size of the beams was not critical. All beams were retroreflected to avoid driving the cold atoms out of the detection region via light-atom scattering momentum transfer. The pump beam polarization was matched with the Raman light while the probe was linearly polarized.

The modulated absorption of the two probe beams was measured with a balanced homodyne detector (Femto HCA-S), which consists of two matched Si PIN photodiodes, providing 40 dB of common mode noise rejection. Typical absorption levels for the cold atom signal were 0.1% for  $10^6$  atoms, while absorption by the background vapor was 8%. The signal from the balanced photodiode was mixed down to DC using radio-frequency (RF) mixers (Minicircuits) with a local oscillator derived from the applied EOM RF signal. The mixer output was acquired on a HP 3458A low-noise digital voltmeter.

The exact intensity, detuning, modulation, and polarization parameters for the pump and probe beams were chosen after a systematic study of their effect on the modulation transfer signal size (Fig. 6.4). Acousto-optic modulators were used to shift the relative frequency between the pump and probe beams, and the signal size was strongly dependent on the probe detuning and the pump carrier detuning being within 100 kHz of each other. This was far smaller than the transition linewidth ( $\Gamma = 5$  MHz). The optimal intensities of the probe and pump beams were found to be 9 mW/cm<sup>2</sup> and 5 mW/cm<sup>2</sup> respectively, as compared with a saturation intensity of 1.12 mW/cm<sup>2</sup>. These features were indicative of a strongly nonlinear process. Each first order sideband generated on the pump by the EOM contained 20% of the total power. The probe beams and the pump beam carrier were detuned 6.5 MHz red of the  $6S_{1/2}, F=4 \rightarrow 6P_{3/2}, F=5$  transition. The modulation depth was not a critical parameter, nor was the detuning of the probe beam and pump carrier beam so long

as they had the same detuning. A 2.487 MHz modulation frequency was chosen based on theoretical predictions of maximal signal with a modulation frequency of  $\Gamma/2$  [46]. The optimum polarizations for the pump and probe beams were  $\sigma+$  and linear respectively.

The pump and probe beams had a kinetic effect on the cold atoms which could be exploited to obtain long interrogation times. Because the beams were retro-reflected and red detuned, they formed a two-dimensional optical molasses. The molasses slowed and stopped atoms returning from the fountain while confining them along the second axis as well. For this geometry, atoms in the  $6S_{1/2}$ ,  $F=4$  state were optically pumped to the  $6S_{1/2}$ ,  $F=3$  level via off-resonant excitations with a time constant of 4.6 ms. With the addition of a repumping beam, the time constant was extended to 16 ms, here limited by heating of atoms along the unconstrained axis. Alternatively, we were able to constrain motion along all three axes by using frequency modulated molasses beams as the pump beams. In this configuration, we achieved detection times as long as 50 msec. However, in situations where there is significant phase noise, such as in a gravimeter, it is not possible to remain centered on a fringe, and this form of balanced detection with FM molasses beams is not practically useable.

### 6.2.1 Detection Noise Analysis

The amplitude of the modulated absorption signal is quite low at the photodiode, corresponding to a signal size of about 0.8 pW per atom. The detection photodiodes have noise-equivalent powers corresponding to a 60 atom detection sensitivity, while the digital voltmeter readout has a 100 atom noise-floor, in the 4.6 ms measurement window. Because absorption detection is used and the absorption is small, there is a substantial amount of unabsorbed light, with  $> 99\%$  of the incident light striking the

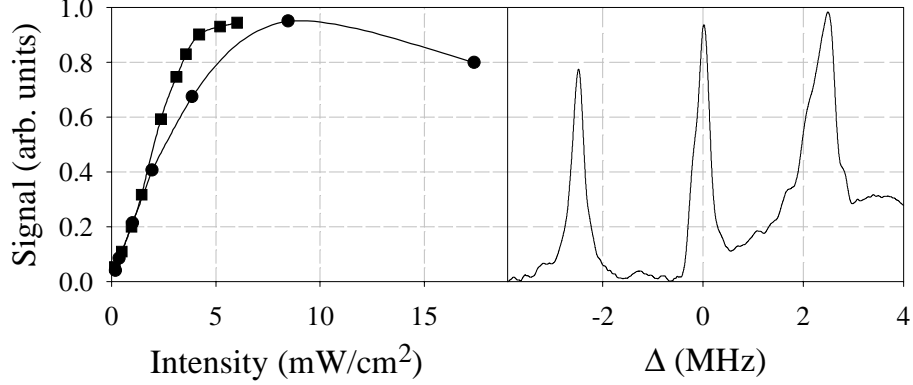


Figure 6.2: (a) Modulation transfer signal size as a function of pump intensity (squares) and probe intensity (circles) using the pump configuration shown in Fig. 1. The two data curves were taken at the probe and pump powers which, respectively, gave optimal signal. (b) Typical frequency lineshapes where  $\Delta$  is the pump detuning from the probe frequency. The three peaks are derived from the correspondence of the probe frequency with the pump carrier and two sidebands. As the detuning becomes positive, one sideband nears resonance, which results in excessive noise.

detector. Shot noise on the number of photons incident on the detector during the integration window is the leading intrinsic noise source, at 0.25 nW, resulting in a minimum detectable signal of  $\sim 300$  atoms. This noise dominates the technical noise sources. Therefore, at greater than  $N = 10^5$  atoms, the noise is no longer photon shot noise dominated but atom shot noise limited  $\sqrt{N}$ .

There is also a noise component of similar size due to a small number of atoms in undesired states which survive the state preparation. Slight changes in laser frequency and selection pulse efficiency during the state preparation cause this number to fluctuate. However, this noise source is common between the two chambers and is also suppressed by the balanced detection method.

The peak performance of the modulation transfer method was exhibited with an ensemble of  $\sim 10^7$  atoms, launched in the  $F=4$  state, but not state selected into the  $m_f = 0$  sub-level. Normalizing the ensemble by detecting it with the two pulse sequence yielded an SNR of 2350:1. Because of laser induced detection noise, we

must correlate noise fluctuations in two simultaneously detected atom ensembles in separate vacuum chambers, as in our gradiometer apparatus, in order to achieve this large SNR without balancing. Balanced mode eliminated the need for this. Without normalization, the shot-to-shot atom number fluctuations limited the SNR to 200:1.

We have measured the common-mode noise rejection ratios for both laser amplitude and frequency noise as well as atom number fluctuations by deliberately inducing these noise sources. Balanced detection rejected these noise sources at the 40 dB, 24 dB and 27 dB levels respectively. The amplitude noise rejection was 40 dB over the detector bandwidth (DC to 10 MHz), which was measured with AM light on the detector. Frequency noise rejection was characterized in two ways. High frequency noise was driven at 2.5 kHz with an AOM during the atom detection (0.27 ms here) in the balanced mode. Low frequencies were studied by making DC changes to the pump and probe detuning together in the balanced mode and measuring how balanced the detection remained. These two measurements gave similar noise rejection levels. With this noise rejection, we inferred that atom shot-noise limited performance could be achieved for atom numbers up to  $10^{10}$  atoms, corresponding to an inferred maximum achievable SNR of  $10^5$ :1. On the other hand, photon shot-noise placed a lower limit on the operating range of  $\sim 10^3$  detected atoms. Below this atom number, the photon shot-noise level was larger than the atom shot-noise limit.

## 6.3 Signal Extraction

### 6.3.1 Interference Fringe Fitting

The original method of extracting gravity gradient information relied on determining the gravitationally induced phase shifts in each atom ensemble by performing

least squares sinusoidal fits on the observed interference fringes. This is possible when vibration-induced phase noise is  $\leq \frac{1}{2}$  rad (about 150ng acceleration noise for  $T=150\text{ms}$ ). The gravity gradient is obtained by subtracting the two phase shifts from each other. Vibrational phase noise and local oscillator phase noise cause the phase extracted by the sine fits to be shifted. However, these noise sources couple to the two accelerometers in a common-mode way. This common-mode behavior results in the two sinusoidal fits being shifted by an identical amount, and any effect of common-mode noise is cancelled in the subtraction used to obtain the gravity gradient. The statistics of the resulting phase differences under static gravity gradient conditions is used to estimate instrument noise.

The distribution of the residual noise contains outlying points, due to non-common phase noise. Eliminating these outlying points increases the SNR by up to a factor of six. The reduction of the number of points is incorporated into the data collection time in determining the sensitivity.

The ratio of the interference fringe amplitude to the standard deviation of the phase difference distributions determines the instrument SNR. The side of a fringe, *i.e.* the linear slope of a sine wave, is most sensitive to phase shifts, with a sensitivity given by  $\delta\phi = 1/\text{SNR}$ . For gravitationally induced phase shifts, the sensitivity to a change in the gravitational acceleration is  $\delta g = \delta\phi/(2kT^2)t^{1/2}$ , where  $t$  is the data acquisition time to achieve the uncertainty  $\delta\phi$ . Dividing by the chamber separation yields the sensitivity to gradients.

### 6.3.2 Magnetic Phase Shifting

When fitting least squares sinusoidal fringes, good common-mode noise suppression requires that the lower and upper chamber fringes be acquired in phase. However, the Earth's gravity gradient of  $\sim 3000 \text{ E}$  will cause a relative phase shift of  $\sim 1.5$

rad between the two chambers. In order to accommodate this shift, a bias magnetic field is pulsed on for 67 ms in the lower chamber during the atom interferometer. This field pulse causes a phase shift due to the second-order Zeeman effect. The amplitude of this pulse is chosen to produce a shift which compensates the shift due to the gravity gradient, allowing both fringes to be acquired in phase.

### 6.3.3 High Phase Noise Regimes

In the case where phase noise is greater than 1 rad, the noise renders it impossible to characterize instrument noise using the least squares fitting. In the most sensitive modes of operation, the vibrations of the reference platform induce phase noise much larger than this level. Two analysis techniques were developed for this regime: Ellipse-specific fitting of the data sets in quadrature and a point-by-point analysis. The former is described in Chapter 7. The latter analysis technique involves performing a normalized detection of  $F=4$  atoms to remove amplitude noise and then a cross-chamber normalization to reject vibration induced phase noise.

After each interferometer cycle (which represents one gradient measurement) two samples are acquired in each accelerometer: signals proportional to the  $F = 4$  population and to the differential population (*i.e.* proportional to the number of atoms in  $F = 4$  minus the number of atoms in  $F = 3$ ). The two samples are combined to infer the total number of atoms present in the interferometer during each experimental cycle. The  $F = 4$  signal is then divided by this total atom number to remove any fluctuations in the amplitude of the  $F = 4$  signal from shot-to-shot atom number fluctuations. We normalize each interferometer with this procedure. To remove common phase noise between the two chambers, a series of experimental cycles is taken, and a least squares minimization (*via* Gaussian elimination) is performed on the quantity  $(S_1 - \alpha S_2 - \beta)^2$  where  $S_1$  and  $S_2$  are the shot-by-shot normalized  $F$



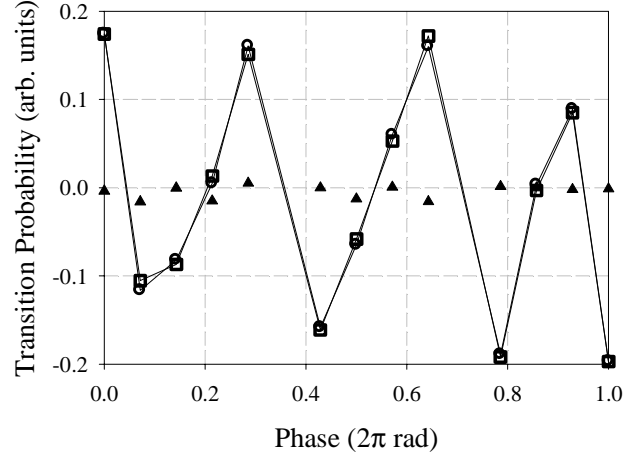


Figure 6.3: Typical gradiometer fringes for  $T=157.5$  ms analyzed using Gaussian elimination. Shown are the normalized fringes for the two interferometers, squares and circles for upper and lower chambers respectively. The residuals are plotted with triangles.

$= 4$  population levels from the two interferometers. The fit constants  $\alpha$  and  $\beta$  are used to compensate for possible differences in interference contrast between the two accelerometers.

For a small phase difference,  $\delta\phi$ , between the accelerometers, the gradient signal is proportional to  $\delta\phi\cos(\Phi)$ . Near the zero crossing of the fringe, where  $\Phi \sim 0$ , the gradient signal is  $\delta\phi$  and therefore proportional to the fit parameter  $\beta$  in the Gaussian elimination. The residuals of the Gaussian elimination procedure are used to estimate instrument noise. This distribution is non-Gaussian, and outlying points are discarded to obtain SNR and short-term sensitivity estimates. This approach is valid when the Raman lasers are given a phase offset so each gravimeter signal is at a fringe zero crossing, necessitating the use of a calibrated magnetic phase shift and vibration isolation.

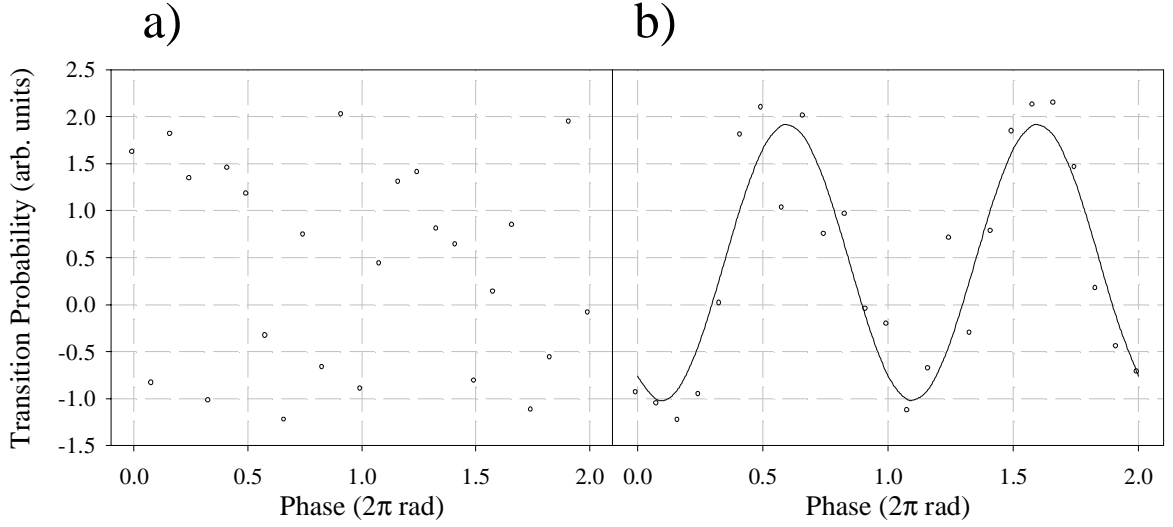


Figure 6.4: Typical gradiometer fringes for  $T=157.5\text{ms}$ . Figure (a) plots an interference fringe from one chamber with no active vibration isolation of the reference corner-cube retroreflector. Figure (b) plots an accelerometer fringe with active vibration isolation of the corner-cube, permitting least-squares sinusoidal fitting.

## 6.4 Shot-Noise Limited Detection

Using the pump configuration shown in Fig. 6.1, we used a two pulse detection sequence in order to measure the total number of atoms as well as the difference signal. We first detected atoms in the  $F=4$  state in the upper probe beam. These atoms were stopped by a 2-D molasses consisting of a vertically oriented pump beam and horizontally oriented probe beam. Atoms in the  $F=3$  state continued to fall. After 7 ms the  $F=3$  atoms were centered in the lower probe beam. A repumper then pumped all atoms to the  $F=4$  state, and the differential signal was detected. This signal consisted of the difference between the original  $F=4$  atoms in the upper probe beam and the repumped  $F=3$  atoms in the lower. We inferred the total atom number from the two detections and then normalized the signal to remove noise from shot-to-shot atom number fluctuations.

Shot-noise limited detection of population differences was achieved with this nor-

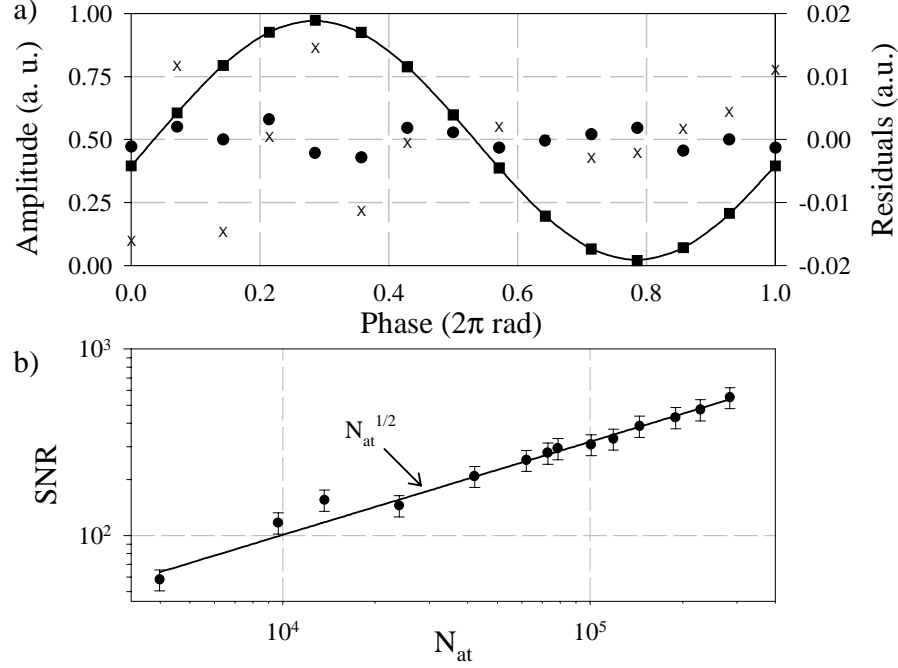


Figure 6.5: a) Normalized Ramsey fringe (squares) showing 1000:1 SNR. The solid line is a least squares fit. The residuals are from the fit for the data before (X) and after (•) normalization. b) SNR detected in balanced mode for various atom numbers  $N_{at}$  using FM molasses beams as pump beams. The solid line represents the shot-noise limit of  $N_{at}^{1/2}$ , in good agreement with the measured SNRs.

malization using  $10^6$  atoms in a microwave clock experiment. Two  $10 \mu\text{s}$  spaced microwave  $\pi/2$  pulses drove a Ramsey clock sequence. The  $F=4$  population level and total number of atoms were detected following the fountain with the two pulse sequence described in the previous paragraph. Scanning the phase of the final microwave  $\pi/2$  pulse generated Ramsey fringes (see Fig. 3a). A sinusoidal least-squares fit was performed on the normalized fringe. Scale factors for the detection signals were fit to account for small differences in detection efficiencies for the two states. The fit gave a SNR of 1000:1, consistent with the shot-noise limit. We defined this SNR as the ratio between the peak-to-peak fringe amplitude divided by the root-mean-square deviations of the residuals of the least-squares fit.

We further studied the sensitivity of this detection method by characterizing

detection noise as a function of atom number. For this study, an ensemble of laser cooled Cs atoms in the  $F=3$ ,  $m_f=0$  state was launched in a 320 ms atomic fountain. A microwave  $\pi/2$  pulse was then used to divide the population equally between the  $F=3$  and  $F=4$ ,  $m_f=0$  states. With the molasses beams modulated as pump beams, the balanced signal was integrated for 33 ms following the fountain. The long integration time was used to minimize the effects of photon shot-noise when detecting small ( $< 10^4$ ) numbers of atoms. With equal populations in the balanced mode a null signal was produced that was free of laser induced noise. The total atom number was varied with a selection sequence of microwave and optical pulses. The SNR was computed for each atom number by comparing the standard deviation of the balanced signal with the peak signal from all the atoms in one state (*i.e.* the maximally imbalanced signal). The measured SNRs agree well with shot-noise limited detection ( $N_{at}^{1/2}$ ) as shown in Fig. 3b.

## 6.5 Direct Balanced FM

To implement a simpler system, we tried detection with FM probe beams without the pump beam. However, RAM at the  $10^{-5}$  level (due to weak etalon effects in the probe beam optical path) limited our observed SNR to 100:1 for  $10^6$  detected atoms (corresponding to 0.1% absorption). If greater numbers of atoms were available for detection (as is the case in Rb atomic fountain clocks) the situation would become more favorable. For example, with  $10^8$  atoms (corresponding to absorption of 10%), the SNR limit due to RAM at the  $10^{-5}$  level is  $10^4$ :1, equal to the atom shot-noise limit.

## 6.6 Sensitivity to Environmental Noise

This section summarizes the prior published results from the gradiometer apparatus. Sensitivity to reference platform vibration and tilt is presented. Measurement of the change in local gravity due to tidal effects provided a characterization of instrument accuracy. Finally, a preliminary measurement of the gravitational phase shift from an arrangement of lead (Pb) bricks is presented.

The atom interferometer gravity gradiometer utilizes the common mode nature of the interferometer light to become insensitive to vertical accelerations of the reference platform. These acceleration noises are indistinguishable from a true gravitational field signal as a consequence of the equivalence principle. Acceleration noise in the form of reference platform rotational tilts, however, do not cause identical gravitationally masked signals in the two accelerometers. An external drive to the reference platform allowed characterization of the sensitivity of the gradiometer to acceleration and tilts by measuring instrument signal to noise ratio (SNR).

### 6.6.1 Acceleration

A voice coil attached to the reference platform containing the corner cube retroreflector provided a means of inducing vertical acceleration noise onto the interferometer Raman light. The corner cube is a common point for both interferometer beams and thus serves as a reference platform site. A sinusoidal drive to the voice coil was triggered simultaneously with the experimental cycle. The gravitational gradient signal was obtained, for  $T = 157.7\text{ms}$ , by collecting data at the most sensitive position at the side of the fringes. A magnetic bias field was used to compensate for the gravitational gradient relative phase offset. A range of drive frequencies was explored, from 1-100Hz. Induced accelerations were measured with a commercial accelerome-

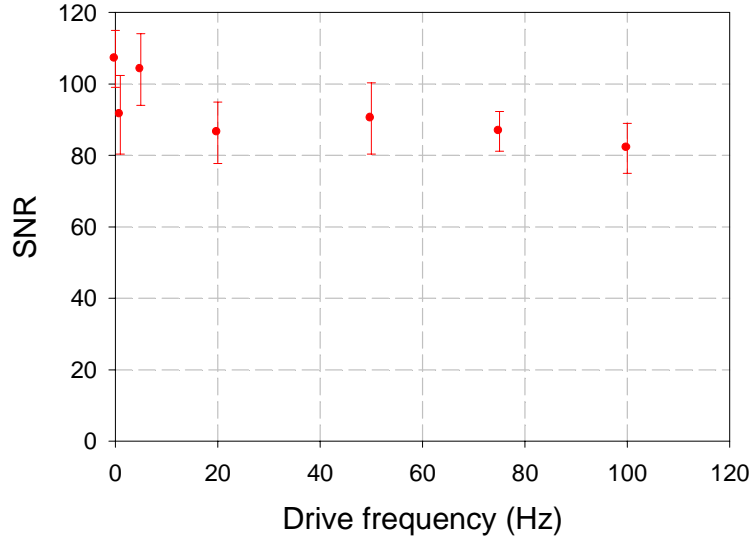


Figure 6.6: Results of an experiment demonstrating vibrational insensitivity of the vertical gravity gradiometer. A voice coil was used to actuate the vibration platform containing the cornercube retroreflector.

ter with an output sensitivity of 500V/g and a bandwidth of approximately DC to 100 Hz (Teledyne Geotech S-510).

Figure 6.6 shows the results of the experiment. No signal degradation was observed within the measurement noise. The maximum drive signal corresponded to an acceleration noise of  $2.5 \times 10^{-2}g$ . Larger accelerations, on the order of 0.1g, are enough to begin Doppler shifting the atoms out of the two-photon Raman resonance. The common-mode rejection ratio is measured to be 140dB, i.e. seven orders of magnitude. This demonstrates the common-mode nature of the gradiometer in rejecting vertical vibration noise of the reference platform.

### 6.6.2 Tilts

Tilts of the reference platform at a rotational rate,  $\Omega$ , produce differential acceleration noise between the two interferometers, as  $\delta R \Omega^2$ , for accelerometer separation  $\delta R$ . For the experimental setup previously described, loss of interference contrast will occur

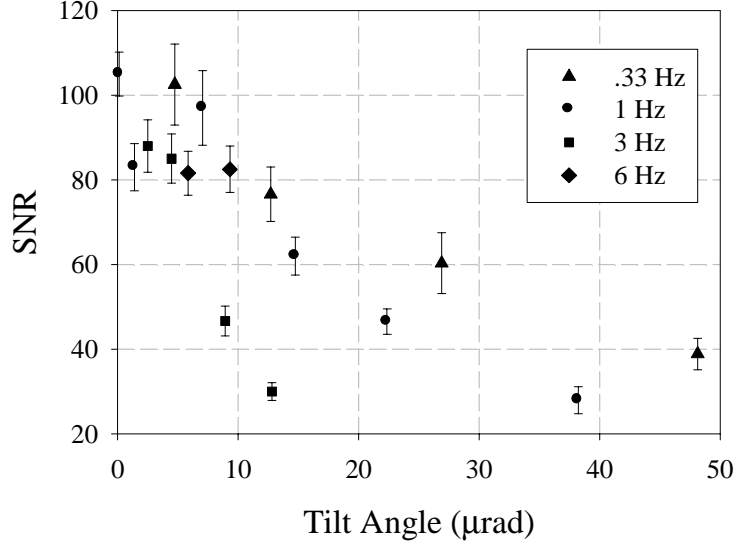


Figure 6.7: Results of an experiment to measure the vertical gravity gradiometer to tilt rates. A voice coil was used to induce sinusoidal tilts of the reference optical table. The falloff corresponds to Coriolis phase shifts decreasing the common-mode rejection between the gravimeters.

at  $\Omega \sim 10^{-3}$  rad/s. The Coriolis force associated with an applied rotation and the transverse velocities,  $\delta v$  of the atoms also lead to phase noise,  $\delta\phi \sim 2k_{eff}\delta v T^2$ . With a source transverse velocity spread of  $\delta v \sim 3$  cm/s,  $\delta\phi = 1$  rad for  $\Omega \sim 10^{-4}$ , resulting in a decrease of SNR.

Figure 6.7 demonstrates the results of an experiment where the reference optical table was tilted at various rates using a driving voice coil. The tilts were characterized with a tilt meter at 20 Hz bandwidth and  $1 \mu\text{rad}$  sensitivity (Applied Geomechanics 755-1129). The rotation rate vector was perpendicular to the propagation axis of the Raman beams, with a 2 m moment arm to the accelerometers. The data agrees with the above prediction. This suggests the possibility of correcting for tilt induced phase shifts and loss of contrast with a closed or open loop feedback from a gyroscope mounted to the reference platform.

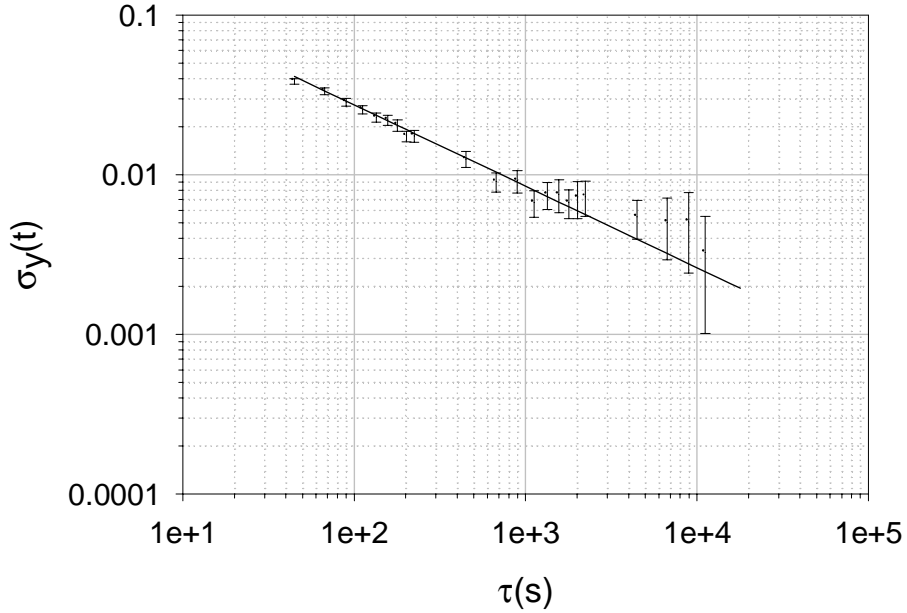


Figure 6.8: Typical Allen variance plot of the Earth gradient over 1.35m with a T=157ms interferometer.

### 6.6.3 Test Mass Effects

The sensitivity of the gradiometer was further demonstrated through the measurement of a stack of 8 lead (Pb) blocks arranged near the lower accelerometer. Each Pb brick had a mass of  $\sim 12.5\text{kg}$  and were stacked symmetrically  $\sim 0.2\text{m}$  from the apex of the lower atomic fountain. A series of gradient phase shifts were measured with the Pb in place and with the Pb removed. Phase readout was performed at the side of the fringe, with a bias field applied to create in phase fringes. The measured signal was  $(8.1 \pm 2.1) \times 10^{-9}\text{g}$ , in agreement with the predicted signal of  $8.2 \times 10^{-9}\text{g}$ .

## 6.7 Conclusion

In conclusion, balanced modulation transfer detection shows promise as a powerful new detection method for cold atomic fountains. In the future, it should be possible



to achieve a SNR in excess of  $10^4:1$  with larger numbers of atoms. This level of signal-to-noise opens prospects of exciting sensitivity gains for precision atomic fountain experiments.

The atom interferometer gravity gradiometer has demonstrated atom shot-noise limited detection using the above methods and demonstrated broad immunity to a number of environmental fluctuations. The detection setup proved to be robust under laser frequency and amplitude noise. The common-mode nature of the gradiometer was proven with shake tests while a platform operational constraint was obtained from the tilt experiments. The following chapters describes further improvements to the above experimental setup, with the goal of a robust and sensitive instrument to be used in a precision measurement experiment.

# Chapter 7

## Ellipse-Specific Data Fitting and Analysis

### 7.1 Introduction

A significant limitation of gravimetry is vibration of the reference platform, appearing as acceleration noise as a consequence of the Equivalence Principle. A gradiometer rejects this noise by taking the difference of two simultaneous acceleration measurements sharing a common reference frame. We have developed and demonstrated an accurate and sensitive gravity gradiometer based upon atom interferometric techniques [5, 39]. Common mode vibrational noise rejection has been demonstrated to a high level, but accurate extraction of small gravitational gradient signals was difficult when the vibrational induced phase noise was larger than  $\pi/2$  rad. This chapter describes the implementation of a technique that is inherently immune to common mode phase noise and allows extraction of accurate gravity gradient phase shifts without the necessity of active vibration isolation of the reference platform.

## 7.2 Ellipse-Specific Fitting

The key idea is that the signals from the two gravimeters are sinusoids which parametrically describe an ellipse. Common phase noise in the two sine signals distributes the data points around the ellipse, but does not change the ellipticity. By fitting an ellipse to the data sets, the phase shift can be rapidly and accurately determined even in the presence of large common phase noise. We detail the application of this technique to our experiment.

The data takes the form of two sinusoidal signals, with a relative phase difference,  $\Delta\phi$ :

$$x = A' \sin(\phi) + B', \quad y = C' \sin(\phi + \Delta\phi) + D' \quad (7.1)$$

In the limit of  $\Delta\phi = \pi/2$  and  $A' = C'$ , the data forms a circle in the x-y plane centered at  $(x,y) = (B', D')$ . In the extreme case of  $\Delta\phi = 0$  (or  $\pi$ ), the data collapses to a line.

The general algebraic form of a conic is:

$$\mathbf{x} \cdot \mathbf{a} = Ax^2 + Bxy + Cy^2 + Dx + Ey + F = 0 \quad (7.2)$$

where  $\mathbf{x}=[x^2, xy, y^2, x, y, 1]$  and  $\mathbf{a} = [A, B, C, D, E, F]^T$ . We can express the phase difference,  $\Delta\phi$ , in terms of the conic parameters:

$$\Delta\phi = \cos^{-1}(-B/2\sqrt{AC}) \quad (7.3)$$

To fit the ellipse parameters, we employ an ellipse-specific fitting routine developed for pattern recognition and vision simulation [48, 49]. This technique finds the algebraic coefficients  $\mathbf{a}$  that minimize the sum of the squared algebraic distances

to the conic for the data points:

$$\min \|\mathbf{D}\mathbf{a}\|^2 \quad (7.4)$$

where  $\mathbf{D} = [\mathbf{x}_1 \ \mathbf{x}_2 \ \dots \ \mathbf{x}_n]^T$  is the  $n \times 6$  design matrix for  $n$  data points. To avoid the trivial solution  $\mathbf{a} = \mathbf{0}$  and keep the system determined, the fit is constrained to be an ellipse through the discriminant:  $B^2 - 4AC < 0$ . We are free to scale the data so that the constraint becomes an equality,  $B^2 - 4AC = -1$ , allowing the minimization problem to be solved through the use of Lagrange multipliers<sup>1</sup>. This reformulates the problem into determining the solutions of a matrix eigenvalue equation with a constraint. The eigenvector with the positive eigenvalue provides real parameters that satisfy the ellipse constraint [48]. It is proven in [48] that the solution of the conic fitting problem admits exactly one elliptical solution. This solution is invariant with respect to rotations and translation of the data.

The conic fitting minimization is biased due to the elliptic constraint. The Lagrange multiplier approach forces solutions away from parabolic conics towards low eccentricity conics. Therefore, for a given elliptical data set, any point far outside the true ellipse will “pull” the elliptic fit to avoid a parabola. However, points within the true ellipse have only a small effect on the elliptic fit.

We have previously shown that the difference phase suppresses common mode vibrations at a level of better than 140 dB for  $\Delta\phi=0$  [5]. In this case, both sinusoids are in phase, and the common-mode performance of the system can be characterized through direct subtraction of appropriately normalized signals using Gaussian elimination. In the absence of vibrations, the relative phase can be directly determined by fitting sinusoids to the data sets. We have previously shown that this technique

---

<sup>1</sup>The constraint reduces the number of unknowns by one in Eq 7.2 to equal the 5 unknowns in Eq 7.1

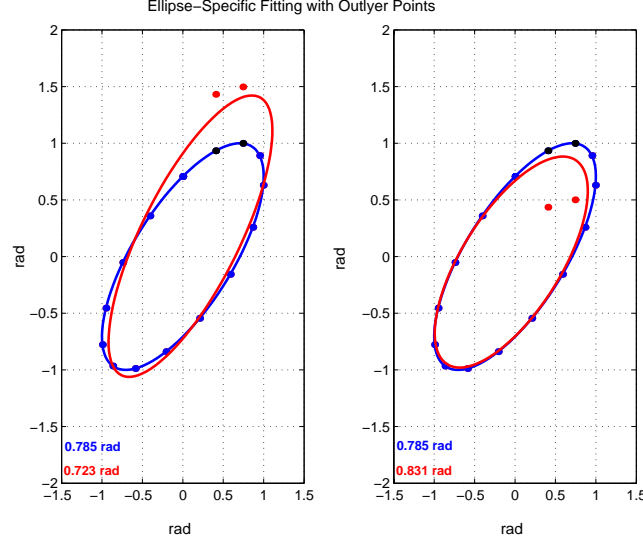


Figure 7.1: Effect of outlying points on ellipse-specific fitting. Outliers exterior to the true ellipse have a larger effect on the fit than interior points. In the simulation above, the black points are equally displaced to create outliers. Visually, the exterior outlier has a greater effect on the ellipse, with a 7.9% deviation in the ellipticity (phase) as compared to 5.5% for the interior outlier.

is also effective at suppressing small common phase noise. In a noisier environment without ellipse fitting parametric data, an active servo is required to keep the system noise in a regime where sinusoids can be fit to the data sets.

Fig. 7.2(a) shows typical signals from the two gravimeters plotted individually for a  $T = 150$  ms Doppler sensitive interferometer where common phase noise dominates (uncorrelated amplitude noise is estimated at the 100:1 level of the detected atom signal). The large phase noise prevents a sinusoidal least-squares fit from producing accurate results. Fig. 7.2(b) reveals the underlying elliptic constraint of the two data sets. The spread of the data around the ellipse is due to the presence of the large amount of phase noise. If no phase noise was present, the data would be bunched closer to the scan phases about the ellipse, as shown with simulated data in Fig. 7.2(c).

### 7.3 Accuracy Test

To validate the accuracy of phase extraction through ellipse fitting, we applied a phase shift that can be independently measured. A magnetic bias pulse which of 66.7ms duration was applied during the first half of the fountain in the lower chamber via Helmholtz coils. The atoms in the fountain are state selected to be  $m_f = 0$ , so they are insensitive to the first order Zeeman shift, but do experience a second order Zeeman shift. This phase shift can be measured independently during the fountain with a  $\pi/2 - \pi/2$  microwave clock experiment instead of the Doppler sensitive interferometer. This independent measurement technique exhibits the same sensitivity to the magnetic bias phase shift as the Doppler sensitive interferometer but is insensitive to accelerations. We least-squares fit a sinusoid to the microwave fringes and calibrate the phase shift for a given applied coil current with the microwave clock. The ellipse fitting algorithm is used to extract the magnetic bias shift applied during Doppler sensitive interferometer sequences. Fig. 7.3 compares the extracted magnetic phase shift with the known applied shift. Over more than  $2\pi$  rad phase shift, there is a close correspondence to at least a part in 100, limited by the statistical uncertainty of the measurements. We have also found the ellipse and least-squares fitting to produce statistically consistent results for the low noise microwave clock fringes.

A small deviation is evident at the applied phases of  $\pi/2$  and  $3\pi/2$ . The inset figure expands the view of the deviation near  $\pi/2$ . We plot the measured bias shift which is determined by subtracting out the Earth's  $\approx \pi/2$  rad gravity gradient phase shift measured with the Doppler sensitive interferometer from  $\Delta\phi$ . At an applied bias phase of  $\pi/2$  rad,  $\Delta\phi \approx 0$ , and the data from the two chambers are in phase and nearly describe a line. The ellipse fitting method cannot accurately fit the phase

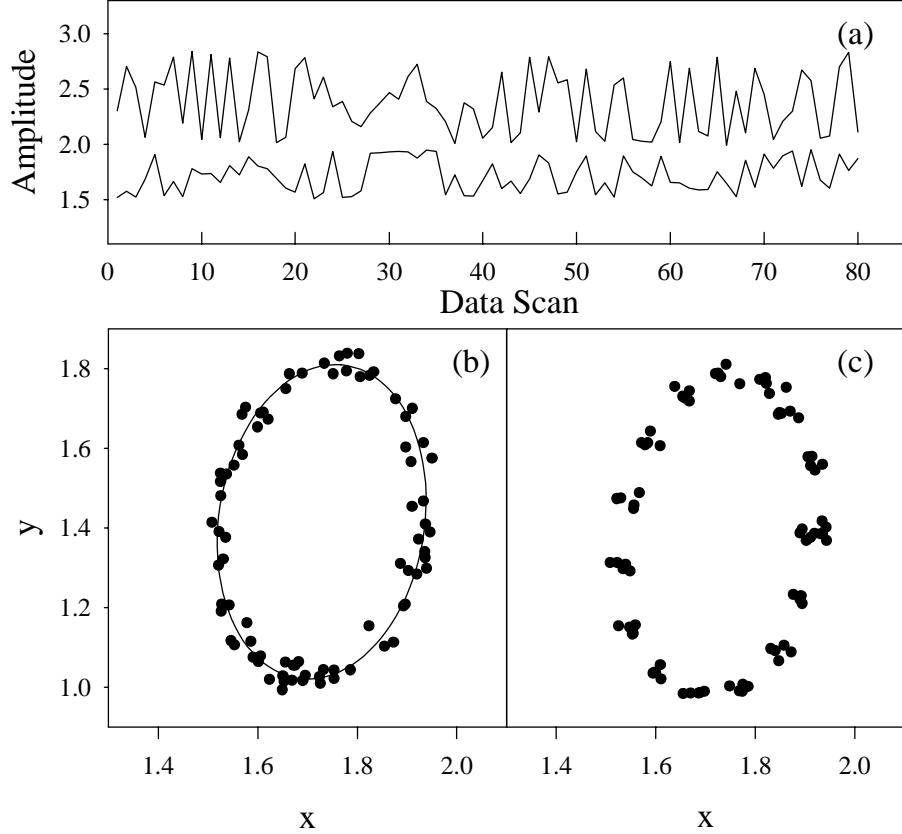


Figure 7.2: Subplot (a) shows the signals from the two gravimeters exhibiting a high level of vibrationally induced phase noise. The phase of each interferometer is scanned over  $2\pi$  every 16 data points. The upper data is offset by one amplitude unit for clarity. Subplot (b) shows the upper trace (y) versus the lower trace (x), demonstrating the elliptic constraint of the data. The solid line is an ellipse fit to the data. Subplot (c) shows simulated scanned data without vibrational phase noise. We have included amplitude noise at the same level as the data.

near  $\Delta\phi = 0 \pmod{\pi}$  when amplitude noise is present. This is well characterized in simulations, and we do not operate near these phases. The magnetic bias pulse can be applied to shift away from these positions if necessary.

## 7.4 Sensitivity Test

The ellipse analysis method has been proven to be immune to the presence of common mode phase noise. In addition to measurement of the Earth's gravitational gradient

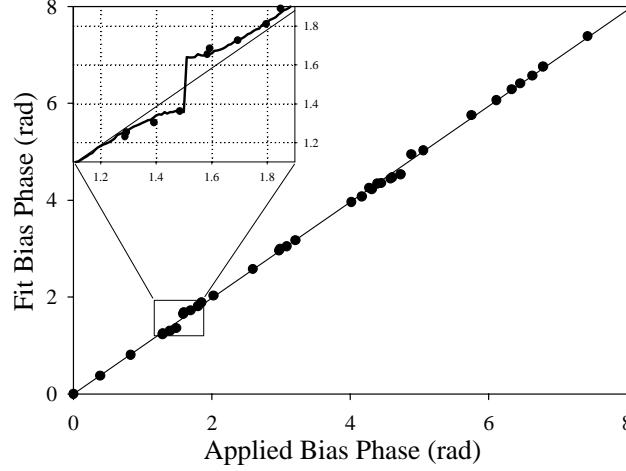


Figure 7.3: The main plot shows the phase extracted using ellipse-fitting of Doppler sensitive data (high phase noise) with a series of increasing applied magnetic bias pulse phase shifts. The inset shows the deviation from linearity of the ellipse-fit phase shift around the applied magnetic shift of  $\pi/2$  rad. The bold curve in the inset shows this behavior in simulations with amplitude noise of a percent. The line is the fit from the entire data set in the main plot.

and magnetic phase shifts, we are using the ellipse technique to measure gravitational phase shifts from a 600 kg Pb test mass, that produces a signal of  $\approx 150$  mrad when moved near to the lower gravimeter. We have calibrated the accuracy of the ellipse fitting technique for detecting small gravitational phase shifts by applying a known magnetic bias pulse phase shift to null the signal from the test mass. We then measure the phase shift produced by the test mass without the nulling bias field, and compare the directly measured phase shift with the inferred shift from the magnetic bias used to null the gravitational signal. The phase shifts agree within the statistical uncertainty of our measurements.

We have tested the ellipse fitting routine with simulated data for a range of amplitude and phase noise levels, including the noise environment of the gravity gradiometer. The results indicated no dependence on common mode phase noise. Simulations show that the phase uncertainty is determined by the level of amplitude noise. The standard deviation of the extracted phase is proportional to the level of



amplitude noise present at up to a RMS level of 20 percent of the signal amplitude. Uncorrelated phase noise significantly affects the extraction of an accurate phase difference by spreading the data points within the limits of the box determined by the ellipse amplitudes. At a noise level of 0.05 rad RMS, the accuracy of the fit begins to deviate at a level larger than the mean uncertainty. This deviation is expected since the ellipse method is contingent upon data which share a definite phase relation. Uncorrelated phase noise in our gradiometer is far below this level.

## 7.5 Geometric Ellipse Fitting Techniques

Ellipse fitting by minimizing the squared algebraic distance to each point is more sensitive to outlying points outside of the ellipse compared to outlying points inside the ellipse. The sensitivity to points outside the ellipse permits easy rejection of these points. For noisy data lying inside the ellipse, a rejection cut can be made based on the ellipse parameters. By requiring minimization of the sum of the squares of the distances to the ellipse, i.e. the geometric distance  $d_i^2 = (\|\mathbf{z} - \mathbf{x}_i\|)^2$  from points  $(\mathbf{x}_i)$  to the ellipse  $(\mathbf{z})$ , this sensitivity may be reduced. The fast algebraic fit is then useful for providing the initial estimates to be used in an iterative, geometric fit. For typical interferometer data, we found that the phase extracted by algebraic fits (Eq. 7.2) as compared to various iterative geometric fits [49] with initial parameters determined from an ellipse specific fit agreed to within the statistical uncertainty of the data. The ellipse fit can also be biased away from the appropriate phase value if the data does not cover the entire ellipse. This can be avoided by fitting larger number of data points or by filtering out data sets which do not meet a distribution requirement. Finally, the geometric criteria provides an effective means for rejecting outlying data points.

## 7.6 Conclusion

The ellipse-fitting method of analyzing data from our gravity gradiometer exhibits immunity to common mode phase noise. It allows fast, accurate extraction of phase shifts without additional vibration isolation. Such a technique may be applicable to a variety of experiments outside of gradiometry. For example, systems with quadrature outputs which share common phase noise, such as in optical interferometers or homodyne detection, could benefit. Another potential role for the ellipse fitting mode of data analysis is in precision measurements to search for changes in the fine structure constant  $\alpha$  via interspecies clock comparisons [50]. It also might be useful in other atom interferometry experiments, such as photon recoil measurements for measurement of  $\hbar/m$  [51].

# Chapter 8

## BIG G - Newton's Constant

### 8.1 Introduction

A measurement of the Newtonian gravitational constant,  $G$ , was performed to characterize the accuracy of the vertical gravity gradiometer and to introduce a new class of measurement of  $G$ . The measurement was performed through the detection of the gravitational gradient induced phase shift from a well defined source mass. The experiment simultaneously explored the limits of the atom interferometer theory. Furthermore, we characterized the systematics of the gradiometer to operating and environmental variables.

As mentioned in the introduction chapter, the gravitational constant is a technically difficult measurement to perform. Most experiments are based on a variation of the torsion pendulum and suffer from similar systematics, both known and hidden. Our measurement uses a proof mass, the cesium atom, that is identical from experiment to experiment and laboratory to laboratory. The process of detecting the gravitational influence is quantum mechanical in nature. Therefore, a number of our systematics are vastly different from prior  $G$  measurements.

The measurement discussed below is based on the developed theory introduced in Chapter 4. However, objects in nature having a purely quadratic potential are rare<sup>1</sup>. Most potentials deviate from quadratic at some level. It is important to realize where the theory breaks down and what errors have to be assigned. Indeed our source mass gravitational potential is not purely quadratic. Deviation from the quadratic requirement was explored and found to not influence our results given the obtained measurement sensitivity.

## 8.2 Experimental Setup

A lead, Pb, source mass consisting of 20 stacked 2.5 cm thick plates with an outer diameter of 35.3 cm and an inner bore of diameter 7.0 cm was used. The source was suspended between the gravimeters on a nonmagnetic stainless steel platform, with a center bore, attached to an aluminum, Al, extrusion support frame (80/20 Inc.). The steel plate was degaussed to remove any residual magnetic fields. A stepper motor translated the Al frame vertically between the gravimeters, guided along a similar frame on frictionless pads. The stepper motor output was sent through a 1:7 gearbox and split into two 1:24 worm gear driven ball-screw jacks. The jacks permitted high movement accuracy and sensitivity, measured at 555 ppm and 31 ppm, respectively.

The Pb density was measured with two independent methods. We used a calibrated scale to determine the mass of each disc and precision calipers to obtain its thickness and diameters. This data provided a density value to each disc. We also used a pycnometer to measure the density using sample pieces cut from the same Pb stock but not used in the experiment. The pycnometer method determines density based on the the volume of liquid displaced upon submersion of the sample. The

---

<sup>1</sup>A uniform gravitational field and a field from a spherical mass in empty space are examples of a quadratic potential.

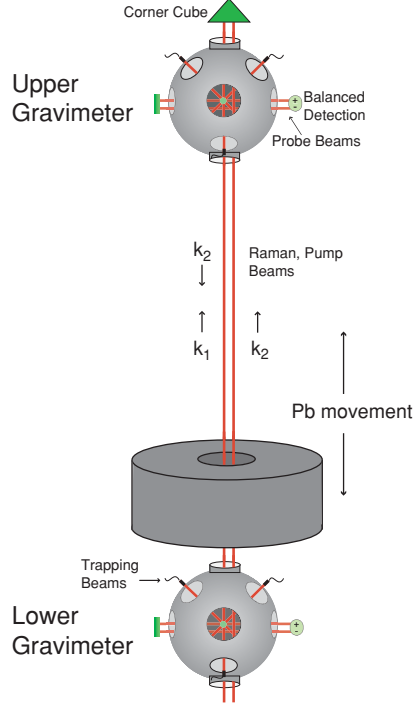


Figure 8.1: Schematic of the vertical gravity gradiometer with the Pb source mass used in the measurement of the gravitational constant. The mass is symmetrically located and translated along the longitudinal axis of the Raman interferometer light.

measurement is calibrated to the density of the liquid. Distilled water was used because of its well characterized density dependence on temperature. The two sets of measurements agreed within statistics. We determined an ensemble density using the mass and volume measurements to be  $11307.8 \cdot (1 \pm 2.6 \times 10^{-4}) \text{ kg/m}^3$ . Individual disc density values were used in the determination of  $G$ .

The Pb discs were formed from melted 99.99% powder Pb cast in a machined mold (Vulcan Lead Inc.). Layers of 1" each on the top and bottom were machined off to eliminate any porosity caused by trapped air in the molten Pb. Trapped air, which would have risen to near the surface during the casting process, creates an inhomogeneous density throughout the disc. Further machining was performed on the inner and outer radii to create a surface of uniform radius.

## 8.3 Procedure

### 8.3.1 Data Acquisition

Our measurement consisted of a series of differential gravity induced atomic phase shift measurements with the Pb source at two positions, near the top of the lower gravimeter and 27.940 cm higher near the center of the gradiometer where the differential phase shift is minimized. The difference in signal intensity at the low and high positions provided a high level of rejection against systematic phase shifts that do not couple to the Pb. These include Raman light induced AC Stark shifts, RF electronic offset drifts, and Coriolis induced phase shifts<sup>2</sup>.

At each position of the source mass a series of 200 data points (experimental shot cycle time of 1.455 seconds) was collected, providing a chopping period shorter than any measured environmental drift. Scanning of the laser phase of the first interferometer  $\pi/2$  pulse,  $\phi_0^{\frac{\pi}{2}}$ , by 16 points was used to map out the sinusoidal interference fringe. The Raman propagation direction was reversed every fringe scan to reject phase shifts not dependent on the Raman propagation wavevector, such as magnetic field induced ( $2^{nd}$  order Zeeman) phase shifts. A single data set typically lasted 7.6 hours, about 1000 data scans, before the timing system had to be restarted due to a loss of contact over GPIB with the Pockel's cell AWG<sup>3</sup>.

### 8.3.2 Environmental Background

Environmental conditions including the gradiometer signal amplitudes, signal contrast, magnetic fields, laser-diode amplitudes, and environment temperature were

---

<sup>2</sup>A Coriolis phase shift arises from a transverse velocity,  $v_t$  to the launch direction, equal to  $k_{eff}\Omega_e v_t T^2$ , where  $\Omega_e$  is the Earth rotation rate.

<sup>3</sup>Pockel's cell rotation of the polarization was consistent over consecutive rotations. This GPIB error does not contribute to any systematic effects on the gradient phase shift.

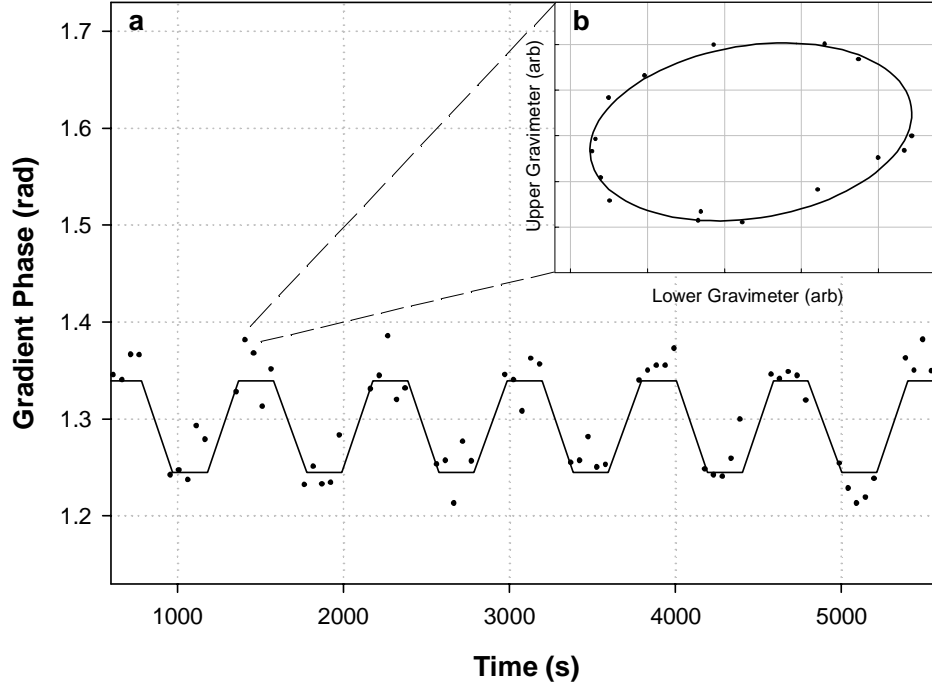


Figure 8.2: Plot (a) is a typical data sequence showing a modulation of the gradiometer phase output as the Pb source mass is displaced 27.940 cm from the top of the lower chamber. Data points are the fit phase of 16 point fringe scans. The single scan scatter was typically 35 mrad. The gravitational force from the Pb caused a  $\sim 30 \times 10^{-9}g$  differential acceleration between the two interferometer signals. The solid trace represents the theoretical signal. The inset (b) is a parametric plot of a typical 16 point scan with the ellipse-specific fit.

monitored and recorded simultaneously with the gradient phase data. The gradient phase shift was not dependent on environmental systematics to within statistical deviations from a collection of data runs ( $< 5 \times 10^{-9}m/s^2$ ). The phase was found to be sensitive to either a trapping/detection laser or a Raman laser coming out of injection lock. This noise source however also produced a strong change in the signal amplitude or contrast, which allowed easy rejection during analysis.

### 8.3.3 Data Weighting and Fitting

Spurious data points (due to laser lock problems) were rejected from the data based on amplitude and contrast cuts. Typical contrast for our interferometer fringes was 25%. The filtered data then was fit with the ellipse-specific routine. The output phases were separated into the two propagation phases and binned into two Pb positions. The phase data was then averaged for each position and propagation and combined to yield a mean chop phase difference for the data run. Standard deviations of the fitted subsets determined the phase uncertainty<sup>4</sup>. Since the acquired data follows Gaussian statistics, the binned data representing different source mass positions and wavevector propagation direction were analyzed with weighted statistics. When combining multiple data sets,  $x_i$ , described by Gaussian statistics,  $\sigma_{x_i}$ , each with a given standard deviation, the weighted mean and weighted uncertainty are given, respectively, by [52]:

$$\bar{x} = \frac{\sum_i \frac{x_i}{(\sigma_{x_i})^2}}{\sum_i \frac{1}{(\sigma_{x_i})^2}} , \quad (8.1)$$

$$\sigma_x = \frac{1}{\sqrt{\sum_i \frac{1}{(\sigma_{x_i})^2}}} . \quad (8.2)$$

A typical series of analyzed phase data is shown in Fig. 8.2. The modulation of the phase with Pb position is clearly visible. The inset figure shows a typical 16 point fringe scan for the two interferometers.

### 8.3.4 Fit Results

To determine a value for G from our differential chopped phase measurement, we modelled the expected signal from the Pb source potential over the trajectory of

---

<sup>4</sup>There is no direct method of using the ellipse fit coefficients to determine a fit uncertainty in a single fringe scan.



the atoms in the two gravimeters. This required accurate knowledge of the atomic trajectories in the two gravimeters as well as their respective distances to the Pb source distribution. The atom velocity was determined by a time of flight (TOF) measurement<sup>5</sup> with the upper detection beam. The timing of the peak atom signal in the upper detection beam in each chamber right after the launch and on their return was measured. This was used to determine the velocity at the time of the first  $\pi/2$  pulse to be  $v_{[\text{lower}, \text{upper}]} = [1.544, 1.539] \pm 0.002$  m/s. We measured the position of the atoms by another TOF technique. This entailed detecting the scatter from the atoms crossing a horizontal near resonant beam whose position was measured with respect to the Pb source. From the Gaussian fit center of the TOF signal, and the knowledge of the launch velocity, we determined the distance of the atoms at the  $\pi/2$  pulse from the Pb source to an uncertainty of 0.3 mm. The same calculations were repeated with the upper gravimeter; the ensemble separation was calculated to be  $1.3469 \pm 0.0005$  m. The atomic trajectory in each chamber could then be calculated taking into account the presence of the local Earth gravitational force.

Using the atom trajectories, we numerically solved for  $\Delta\phi_{Tot} = \Delta\phi_{Laser} + \Delta\phi_{Path} + \Delta\phi_{Sep}$  using the exact potential of the Pb source and the second order Taylor expansion of the Earth potential (including the Earth's gradient)[34, 35]. The gravitational phase contributions of the stainless steel plate and support rods were numerically calculated. As expected, a full calculation which took into account the acceleration due to the Pb source on the atomic trajectories agreed to a ppm with a perturbative calculation integrating only the Pb source potential over the unperturbed trajectory. The differential chop phase shift is proportional to  $G$ . We estimate that any deviation from the path-integral formalism due to the Gaussian wave-packets

---

<sup>5</sup>Doppler sensitive spectroscopy with the Raman beams was attempted but was found to not be accurate at the percent level due to AC Stark shifts

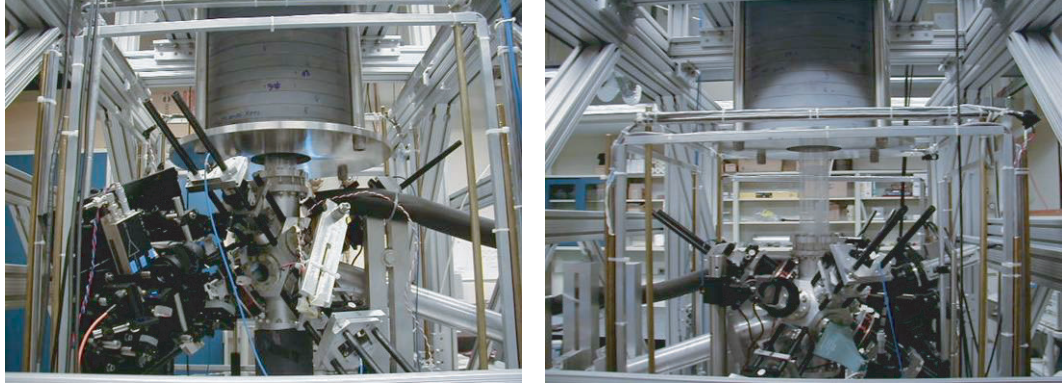


Figure 8.3: Picture of the lower atom interferometer chamber. Shown is the Pb used in the  $G$  measurement at two positions between the two chambers. The stainless steel and aluminum support is visible in the background.

and non-quadratic potential terms from the Pb source is negligible. Rotational couplings to the Pb source were determined to produce negligible phases shifts in the differential source chop phase.

The gravitational phase shift model yielded a value of  $G = (6.696 \pm 0.037) \times 10^{-11} \text{ m}^3/(\text{kg} \cdot \text{s}^2)$  for data run 1. The integration period lasted for 54 data sets ( $\sim 18$  days). After a study of potential systematic sources of error on the interferometer phase shift, discussed below, we performed a repeat measurement. In the latter study we placed the Pb mass 0.635 cm higher than for data run 1, maintaining a 27.940 cm displacement cycle. Furthermore, we reordered the individual Pb discs comprising the source mass. We obtained a value of  $G = (6.691 \pm 0.041) \times 10^{-11} \text{ m}^3/(\text{kg} \cdot \text{s}^2)$  in the second integration period, lasting 39 data sets ( $\sim 13$  days). We performed analysis tests similar to those used on the first data run, with the results from runs 1 and 2 agreeing to within statistics. Combining the two measurements results in a statistical value of  $G = (6.693 \pm 0.027) \times 10^{-11} \text{ m}^3/(\text{kg} \cdot \text{s}^2)$ . The Pb source mass gravitational phase shifts from the two run cycles are represented in Fig. 8.4 and Fig. 8.6. Figure 8.5 shows our data and its agreement with CODATA. Several  $G$  measurements mentioned in the references are listed for comparison [11–14, 16–

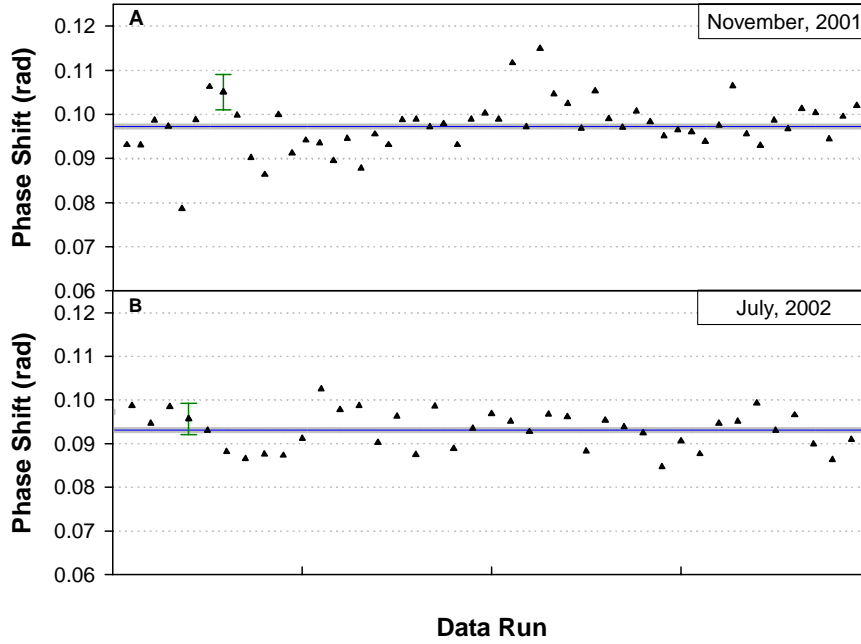


Figure 8.4: Data used in the determination of  $G$ . The top plot shows a data sequence consisting of 51 data sets. Analysis of the phase shifts resulted in a value for the Newtonian gravitational constant,  $G = (6.696 \pm 0.037) \times 10^{-11} \text{ m}^3/\text{kg} \cdot \text{s}^2$ . Plot (b) shows a second measurement of  $G$  with a different initial vertical position of the source mass and a redistribution of the individual discs comprising the Pb stack. The same analysis as the first measurement gave a value of  $G = (6.691 \pm 0.041) \times 10^{-11} \text{ m}^3/\text{kg} \cdot \text{s}^2$ . Combined results of our measurements, plot (c), agree within statistical uncertainties of each other and of the CODATA value, resulting in  $G = (6.693 \pm 0.027 \pm 0.021) \times 10^{-11} \text{ m}^3/\text{kg} \cdot \text{s}^2$ .

18, 53–57].

### 8.3.5 Long Term Statistics

Knowledge of long term stability the vertical gravity gradiometer can be inferred from the compiled one month data run. Figure 8.6 contains each individual gradient phase shift difference between the two source mass positions. The upper figure is a 2-sample Allan standard deviation [58] of the chop phase shifts, obtained by evaluating

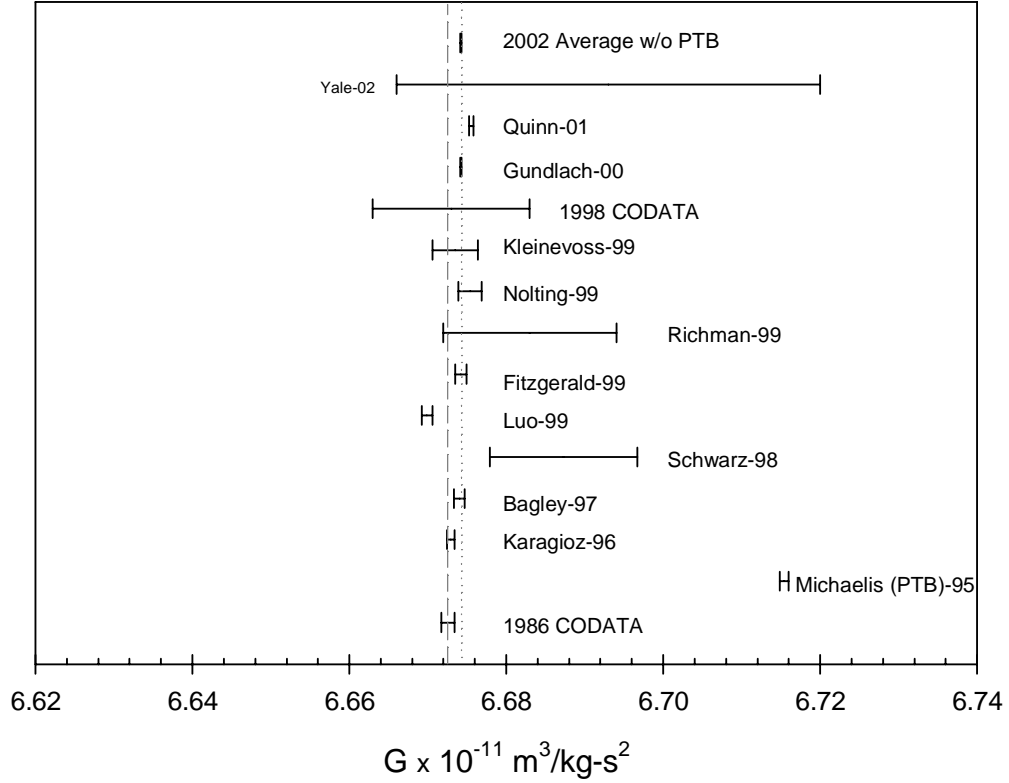


Figure 8.5: Combined results of our measurements agree within statistical uncertainties of each other and of the CODATA value, resulting in  $G = (6.693 \pm 0.027 \pm 0.021) \times 10^{-11} \text{ m}^3/\text{kg} \cdot \text{s}^2$ . The dashed and dotted lines represent the 1986 CODATA value and the 2002 average excluding the PTB results, respectively.

the variance over different sized bins:

$$\sigma_y(t) = \sqrt{\frac{1}{2(M-1)} \sum_{i=1}^{M-1} (y_{i+1} - y_i)^2} \quad (8.3)$$

The Allan deviation is an analysis tool commonly used in determining the stability of a system. Eq. 8.3 measures the variation of successive  $M$  fractional offset measurements spaced in segments of  $t$ . When plotted as a function of integration time,  $t$ , the Allan plot is used to identify different sources of oscillator and measurement noise sources. The slope of the Allan plot at various points indicates the

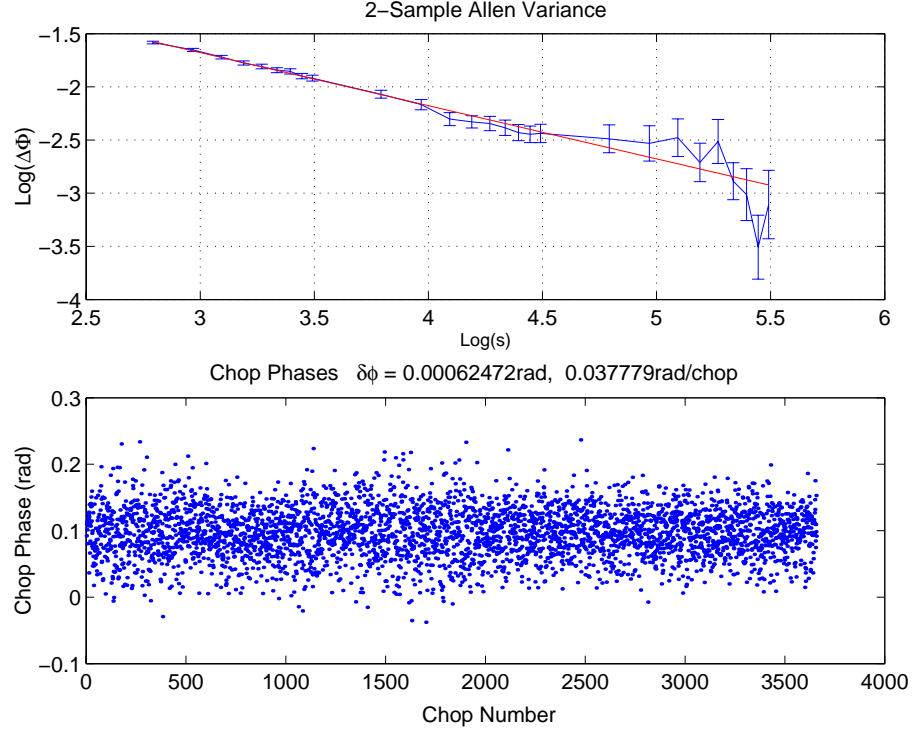


Figure 8.6: Compiled results of the two data runs. The lower figure plots individual gradient phase shift differences between the two source mass positions. The upper figure is a an Allan deviation of the chop phase shifts, with the solid line extrapolating a  $t^{1/2}$  white-noise scaling in time,  $t$ , of the single chop uncertainty.

required scale of averaging to remove a particular source of noise. For example, a slope of  $-1$ , indicates the dominant noise is either white-phase or flicker-phase in origin<sup>6</sup>. A slope of  $-1/2$  shows a white-frequency dominant noise source. Flicker-frequency, or the "flicker floor", has zero slope while a random walk noise source scales the Allan deviation by  $t^{1/2}$ .

Since the gravity gradiometer is measuring the well defined phase of the atomic interference fringe, an Allan deviation analysis of the resultant phase in the time domain could yield useful information about the origin of any noise source. The solid line of the Allan plot is an extrapolation by  $t^{1/2}$  from the single chop uncertainty. The extrapolation demonstrates statistics dominated by white-noise scaling. This

---

<sup>6</sup>Flicker noise is a low frequency noise whose power spectral density is inversely proportional to frequency. Otherwise known as  $1/f$  noise.

implies that we can use Gaussian statistics over all the data sets and integrate over long periods. A long term accuracy of the gradiometer is obtained by comparing the measurement to the 1998 CODATA value for  $G$ . An accuracy of the the gradiometer at 0.65E, for our 1.35m atom ensemble separation, or 0.09E for a 10m device, is observed.

## 8.4 Systematics

Knowledge of how the accuracy of our measurement is affected by environmental and device parameters is crucial for a future precision measurement of  $G$  with our technique. These tests are presented below with the results summarized in Table 8.1. Systematic uncertainties limited our experiment to an accuracy of 3 ppt. The dominant systematics were the accuracy of knowledge of the atom ensemble initial position and launch velocity. These measurements were limited by the existing optical access of the vacuum chamber, an issue easily solved in a next generation experiment.

### 8.4.1 Atomic Ensemble Localization

The largest contribution to the systematics in the determination of the gravitational constant came from the imprecision of the knowledge of each atomic ensembles' position within the fountain as a function of time and of the initial launch velocity the atoms acquired when cooled into a moving frame. As described above, in determining the initial velocity and position information, we independently used imaging and TOF techniques. The resulting velocity uncertainty of  $2 \times 10^{-3} \text{m/s}$  for each chamber and initial position uncertainty of  $3 \times 10^{-4} \text{m}$  corresponds to a fractional  $G$  systematic uncertainty of  $1.88 \times 10^{-3}$  and  $1.85 \times 10^{-3}$ , respectively.

The separation between the atomic ensembles was measured with the atoms located at the position of the first  $\pi/2$  pulse. Initially ccd imaging of the atoms in each chamber was performed to acquire the local positions of the atoms relative to a respective reference point located on the moving source mass support structure. This measurement was verified with a more precise position determination from a horizontal probe beam that scattered light from the atoms in a TOF technique. A spare viewport into the chamber was used in the measurement. Wedge effects from the window (BK7 glass), due to a  $20^\circ$  angle relative to the probe and camera, had to be accounted for. The precision and accuracy of the known dimensions of the moving support frame and the measured steel plate and Pb dimensions were used to couple the two local position reference points. The resulting separation of 1.3469m had an associated uncertainty of  $5 \times 10^{-4}$ m. This value corresponds to a fractional accuracy error of  $1.9 \times 10^{-4}$  in G.

#### 8.4.2 Source Mass Density (Homogeneity)

Determination of the gravitational constant is linearly proportional to the source mass density, assuming no position dependence on density. The source mass was specified as 99.99% pure Pb. We characterized the dimensions of the discs and steel plate to 0.1 – 1ppt with precision calipers and the mass to 40ppm using a calibrated scale and mass standard. The results are listed in figure 8.7.

A pycnometer technique was used to test the density homogeneity of small samples cut from two Pb discs not used in the G measurement. This also was used to verify the mass-volume measurements of density as described above. Density variation was determined to within 260 ppm over the discs used within the experiment. The pycnometer variation was as large as  $5 \times 10^{-3}$  ( $1 \times 10^{-3}$  excluding the one outlier point). Estimating an upper bound of less than 1% radial and longitudinal density

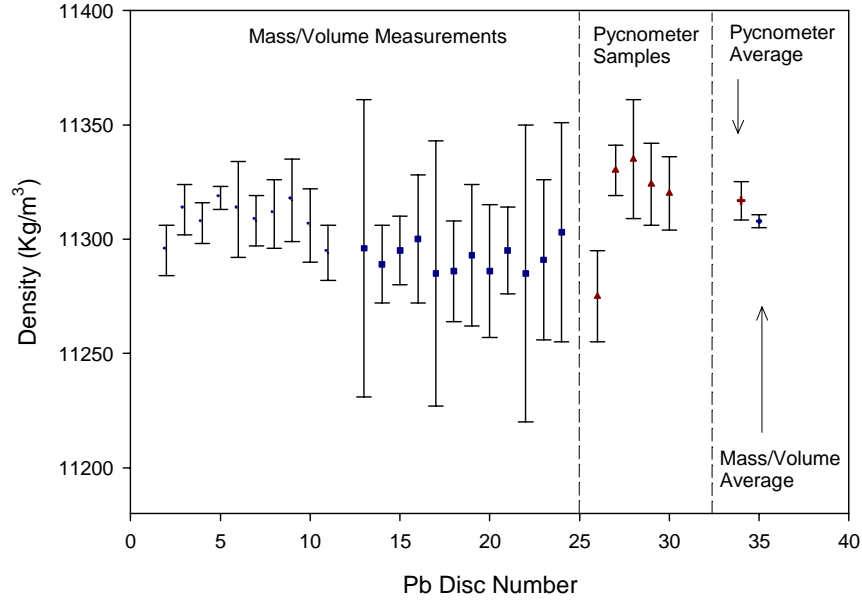


Figure 8.7: Measurements of the Pb density. The first section of the plot shows results from mass/volume measurements of the density. The difference between precision machined (circles) and rough machined (squares) pieces is evident. The middle section contains pycnometer measurements of density. The last section summarizes the two measurements.

inhomogeneities contributes a  $2 \times 10^{-4}$  systematic uncertainty in determining  $G$ .

### 8.4.3 Source Mass Radial/Vertical Displacement

The gravitational potential of the Pb cylindrical geometry afforded us an insensitivity to radial displacements at the 100ppm level ( $1 \times 10^{-5}$  rad) over 5mm of radial translation. However, we initially found a 5 mrad/mm dependence on the position of the Pb in the plane perpendicular to the interferometer axis, Figure 8.8. Measurements using Doppler-free Raman transitions on the magnetically sensitive transitions and a commercial magnetometer near the chamber, as the Pb was displaced, revealed that residual differential eddy current fields caused a less than  $2 \times 10^{-4}$  Gauss change throughout the fountain. This field strength was not enough to account for the ob-



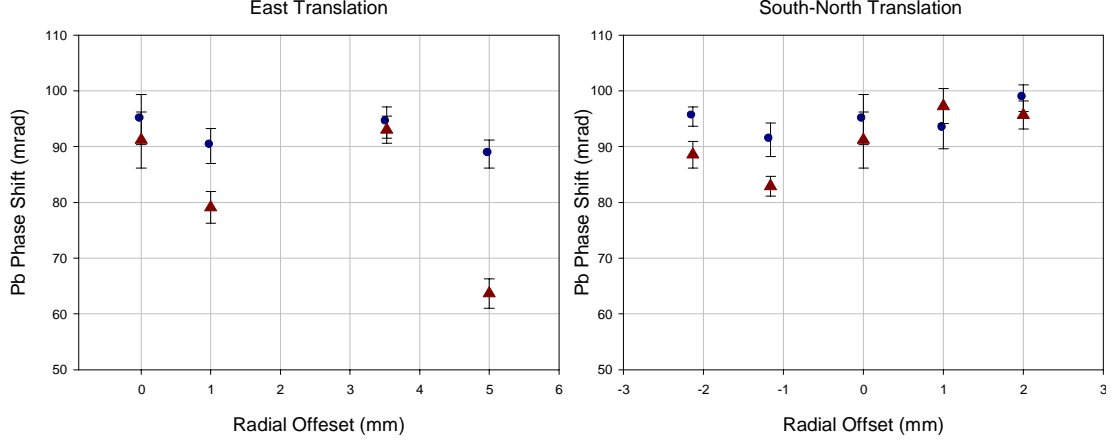


Figure 8.8: Radial position dependence of the source mass phase shift before, triangle, and after, circle, reduction of quadrupole field shutoff induced eddy-currents within the Pb.

served translational dependence. We believe there were transverse magnetic field gradients, beyond the 250Hz bandwidth of the magnetometer, causing a combination of second order Zeeman and Coriolis phase shifts. Magnetic shielding would significantly attenuate the magnetic field gradients from the source assembly.

After we implemented a controlled ramp-down of the quadrupole field to reduce eddy currents in our Al chambers and Pb support plate, we no longer saw a dependence on the transverse positioning of the source. A follow up study of the relationship of the gravitational phase shift to the transverse placement of the source mass indicated no statistical dependence on deviations less than 1cm from the longitudinal axis.

#### 8.4.4 Magnetic Field Gradients

Magnetic fields originating from the source mass and its support structure can cause spurious phase shifts. A differential field gradient, between source mass positions, during the fountain would lead to a second order Zeeman phase shift between the two hyperfine ground-states. This leads to a systematic phase shift in the interferometer.

First order Zeeman shifts have no effect on the interferometer since magnetically insensitive sublevels are used. The full effect of a magnetic field on the ground-state hyperfine splitting,  $\omega_{hfs}$ , is given by the Breit-Rabi formula [59]:

$$\omega_{hfs}(F, m_F) = -\frac{\omega_{hfs}}{2(2I+1)} - \frac{g_I \mu_B B_0 m_f}{\hbar} \pm \frac{\omega_{hfs}}{2} \sqrt{1 + \frac{4m_F}{2I+1}x + x^2} , \quad (8.4)$$

$$x = \frac{(g_J \mu_B + g_I \mu_N) B_0}{\hbar \omega_{hfs}} . \quad (8.5)$$

To second order, a magnetic field causes a potential energy shift on the  $m_f=0$  sublevel  $F=3$  to  $F=4$  hyperfine transition:

$$U_{hfs}^2 = \hbar(427.45 \text{ Hz}/G^2) B^2 , \quad (8.6)$$

causing a phase shift:

$$\Delta\phi_{\nabla B} \approx 2(427.45 \text{ Hz}/G^2) v B \frac{dB}{dz} T^2 , \quad (8.7)$$

where  $v$  is the velocity parallel to the field gradient[60]. Since the induced interferometer phase shift is an even power of the magnetic field, it is easy to assume that a reversal of the Raman wavevector propagation direction for a given field would give the same phase shift while reversing the sign of the gravitational phase shift. However, propagation reversal does not completely isolate against second order Zeeman shifts. This is because there is a slight path difference between propagation reversal, due to the direction of momentum recoil within the interferometer. By combining the second order potential above with the action describing the path phase shift within the path integral formalism, we are able to determine the effect of a magnetic field gradient via the second order Zeeman effect on the  $G$  measurement.

Figure 8.9 depicts the results of an experiment to measure the effect of a magnetic

field gradient applied to the upper interferometer chamber. The magnetic field was mapped using a Doppler free  $\pi$ -pulse on the atoms at various points within the fountain. By scanning the two-photon frequency, we could map out the frequency separation of the magnetic sublevels. Using the first order Zeeman shift between the two hyperfine states,

$$\Delta\nu_{hfs}^1 = m_f(700.8kHz/G)B \quad , \quad (8.8)$$

we were able to use the atoms as a magnetometer by measuring the positions of the  $F=3, m_f = f \rightarrow F=4, m_f = f$  transition peaks. The solid line represents the theoretical phase shift caused by the second order effects, where at each point the vertical component of the magnetic field was mapped throughout the fountain path.

We measured the 3-axis magnetic field of the Pb source mass and its stainless steel support plate using a calibrated fluxgate magnetometer as a function of distance. A field gradient of  $3 \times 10^{-3}G/m$  was measured. This was used as a bound on the uncertainty in determining G caused by the second order Zeeman effect. A systematic fractional uncertainty in G of  $1 \times 10^{-3}$  was obtained.

#### 8.4.5 Coriolis Phase Shift

The presence of a transverse magnetic field during the atom launch, a tilt of the optics table, or a transverse power imbalance in the trapping light will cause a transverse velocity component to be added to the atoms within the fountain. Power balance was obtained with photodiodes at the chamber and the launch verticality was monitored with ccd imaging of the atoms before and after the launch. To explore the effect of transverse magnetic fields, i.e. residual eddy currents in the source mass and support or their magnetization, we applied a magnetic field pulse at various points in the sequence from a coil placed near the chamber. Variation of the transverse

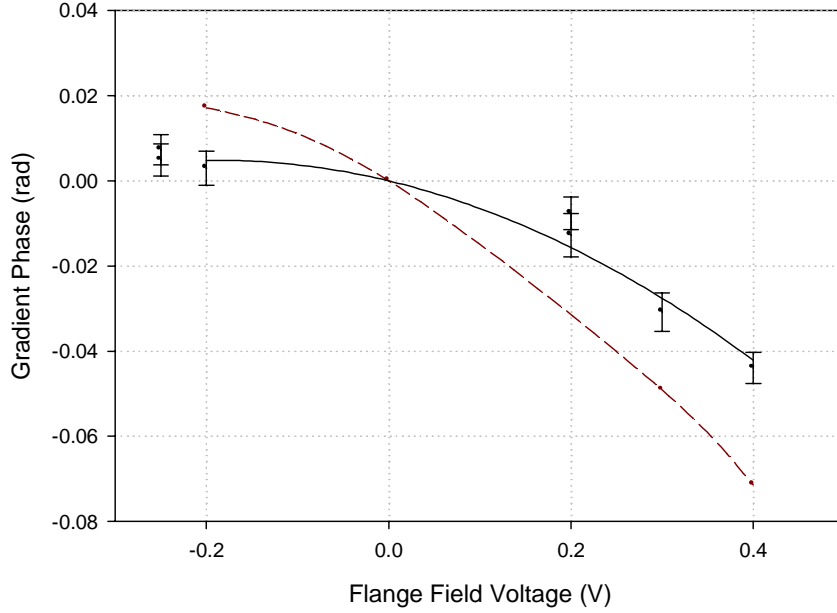


Figure 8.9: Applied static magnetic field gradient-induced phase shift on the upper interferometer chamber. The solid line represents theory based on a second order zeeman shift potential added to the interferometer Lagrangian.

fields from the Helmholtz coil produced no measurable effect on the interferometer phase. The pulse length was always some multiple of the power line cycle (60Hz). We only observed an effect when a transverse pulse was applied to the launch sequence, when the atoms are cooled into a moving frame. This is typically 50ms after the quadrupole fields are shut off and any measurable eddy currents have dissipated. Figure 8.10 depicts the results of this study. Transverse velocity was measured with the imaging described above. The solid line is a model based on the Coriolis phase shift:

$$\Delta\phi_{cor} = 2\Omega \cdot (v_{tran} \times \mathbf{k}_{eff})T^2 \quad , \quad (8.9)$$

where  $\Omega$  is the Earth rotation rate ( $7.29 \times 10^{-5}$  rad/s) and the cross product is taken at our latitude of  $41^\circ$ . We believed the deviation on the positive velocity axis may be due to an existing transverse launch velocity that is negated by the field pulse. We

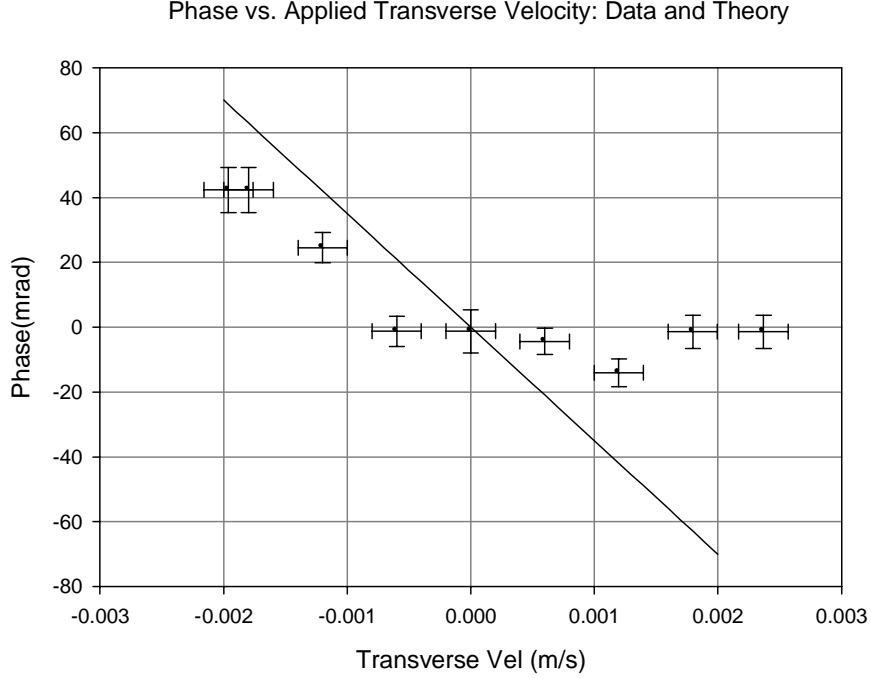


Figure 8.10: Transverse component of the launch velocity effect on the measured phase shift. The solid line is a theoretical model based on Coriolis induced phase shifts.

operated where there was no observed Coriolis phase shift. Taking into account the measured residual  $\sim 0.5\text{mG}$  field from the source mass in its lower position combined with the above observed effect, we estimate an upper bound  $9.8 \times 10^{-4}$  fractional uncertainty in determining  $G$ .

#### 8.4.6 Detection Aperturing

If the atoms entering the detection region are apertured by the probe detection beams, i.e. if the probe light interacts with a portion of the returning cloud of atoms, then we may observe a systematic Coriolis phase shift due to the finite temperature of the ensemble. To test for this effect, we varied the timing of the detection sequence relative to the atom launching and interferometer sequence. By varying this time, we were able to map out the profile of the atoms as they enter the probe beams.

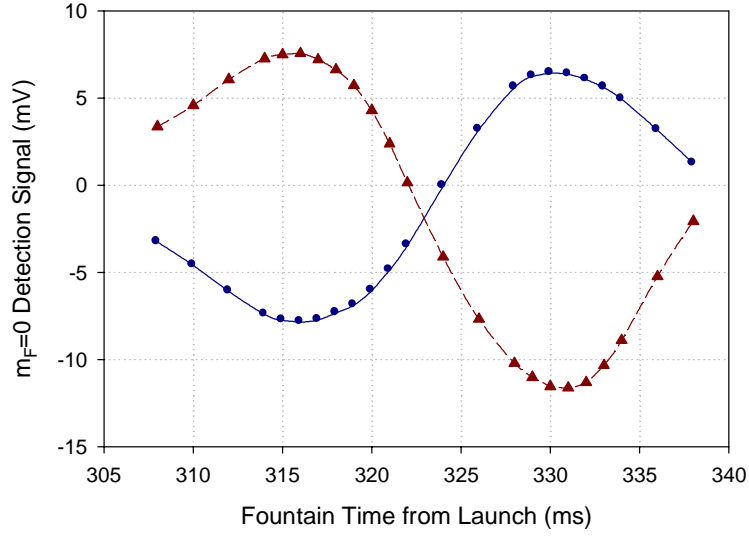


Figure 8.11: Time profile of atoms entering the detection region for the lower and upper chamber, circle and triangle respectively. The peaks represent when the atoms are entirely within either of the two detections probes for a given chamber.

Figure 8.11 depicts a typical detection profile. The two traces are for the different chambers. The sign difference is an artifact of the sign of the balanced detection relative to the two detection setups. From left to right, the first peak depicts atoms in the  $F=4$  state entering the first detection probe. The second peak represents the  $F=4$  atoms entering the second detection probe. Varying the position of the atoms vertically in the detection beams did not cause a statistically significant deviation in the source mass induced differential phase shift. The results are summarized in Figure 8.12, along with other systematic tests.

#### 8.4.7 Cold Atom Collisions

The effect of background vapor pressure on the source mass phase shift was also experimentally studied. In the presence of too much vapor, the ensemble of atoms in the fountain may undergo collisions with the background atoms. It is known that cold collision between atoms in an atomic fountain clock causes a systematic

frequency shift between the hyperfine ground-states [61, 62] ( $-15.8 \pm 1.4$  mHz in cesium for a density of  $(1.0 \pm 0.6)9/\text{cm}^3$ ). Our cesium source is located in a cold finger connected to the interferometer chamber by a valve. The steady state vapor pressure is controlled with this valve. We typically operate at a point  $\sim 10\%$  below the point where the background vapor causes a decrease in the MOT atom number signal. We performed a series of source mass measurements with the valve nearly full open in both chambers, where the state selected signal was as low as 60% of the original signal. No observable dependence on the gradient signal with vapor pressure was found. According to [63], for a single Cs gravimeter with a fountain length of 450ms and  $3 \times 10^6$  atoms after velocity pre-selection, the cold collision frequency shifts amounts to a 0.6mrad systematic phase shift. Our interferometers have the same order of magnitude atom number, but a shorter fountain time by a factor of 2/3. We expect an even smaller collisional effect that is further reduced by the gradiometer difference between interferometers.

#### 8.4.8 Interferometer and State Selection Parameters

We individually offset other parameters to values beyond accepted operating characteristics of the gradiometer, often to the point where the interferometer fringe contrast decreased to an inoperable limit of  $\sim 10\%$ . These are parameters that did not have an observable effect on the phase if they drifted, but required characterization nonetheless. These variables included: Doppler sensitive  $\pi$ - and  $\pi/2$ -pulse lengths, position of atoms in the detection probe beam, detection pump efficiency, launch angle, off-resonant Raman light, initial  $m_f \neq 0$  population, scattering from the background Cs vapor, and Raman light intensity and wavefront quality. These results are summarized in Figure 8.12.

Imperfect  $\pi/2$ -pulses in the interferometer sequence lead to a loss of fringe con-

trast. However, an imperfect  $\pi$ -pulse introduces additional paths in the momentum-recoil diagram. This could introduce additional paths within the interferometer that may interfere, creating additional phase shifts. With a 2-photon recoil velocity of 7mm/s, these additional wavepackets would be separated by about 1-2mm, although they are detuned by 2-4 photon recoils (4.14-8.27kHz) from the final 2-photon Raman transition. We varied the middle  $\pi$ -pulse length by  $\pm 20\%$ . A series of 7.5 hour data runs were performed. The results agreed with each other statistically; no outlying dependence was observed. Larger deviations from  $\pi$  reduced the fringe contrast below the operable limit.

Another concern is the amount of background off-resonant Raman light. The racetrack geometry contains on resonant 2-photon Raman light while the off axis arm consists of the wrong propagation direction, which is out of resonance. If the Pockel's cell is inefficient, then off-axis light may contaminate the on-axis interferometer light. This leads to an increase in spontaneous emission from far detuned light. Pockel cell efficiency was periodically checked every few days and optimized such that there was less than 0.5% of off-axis contamination. Increasing the contamination by an order of magnitude decreased the fringe SNR but did not give a noticeable dependence on the phase.

The D2 transition frequency is well known [64], but the assumption of  $|k_1| = |k_2|$  was used. The difference in values is on the order of 0.1ppm. The Cs hyperfine frequency difference leads to a fractional frequency error of  $3 \times 10^{-5}$ . The resulting fractional uncertainty in determining  $G$  is the same, and is at least two orders of magnitude below the dominant systematics in our experiment.

Misalignment of the Raman beams to verticality enters as a  $\cos(\theta)$  multiplication to the phase shift, for an effect of  $\Delta G/G = 0.001$ , equivalent to the fractional phase uncertainty  $\Delta\phi/\phi$ ,  $\cos(\theta)=0.999$ . In other words the angle of the Raman light has to



be vertical to within  $2.56^\circ$  (45mrad). This translates to a transverse MOT separation of approximately 6.3cm. Our knowledge of the MOT alignment is known much better than 6.3cm, so vertical Raman beam misalignment at the above level is not a concern.

By creating imperfect microwave  $\pi$  pulses in the state selection sequence, we explored the possibility of contaminating the interferometer with atoms in the  $m_f \neq 0$  states. This was performed by using only a single microwave pulse and a blue detuned clearing pulse. The normal procedure used two microwave pulses and a repumper. Only a few data sets were collected but nothing outside of the normal distribution was observed.

We tested the effect of clipped Raman beams. We did not measure any change in the diameter of the light when the Pb was translated. An index card was placed before a polarizing beam splitting cube that split the two Raman frequencies into the racetrack. The card obscured about 25% of the Raman light. This was a concern because with the 2cm diameter Raman beams and the 7.0cm inner diameter of the Pb, the off and on axis raman were nearly tangent to each other. The predominant effect is to reduce the contrast of the interferometer as the reduced optical power creates imperfect pulse areas. No outlying effect was observed beyond the statistics.

The other systematic offsets were explored in a similar fashion. The integration of the data runs typically resulted in a sensitivity of less than 4mrad ( $< 12 \times 10^{-9} m/s^2$ ). Due to the large systematic offsets, we observed no outlying points consistent with the statistics of our measurement. We were able to conclude that these parameters do not contribute toward a systematic uncertainty given our integrated statistics.

#### 8.4.9 Detection Normalization Coefficients

We looked for systematic effects in our analysis by varying the analysis procedures. This was performed to study the dependence of the fit results on the input parameters

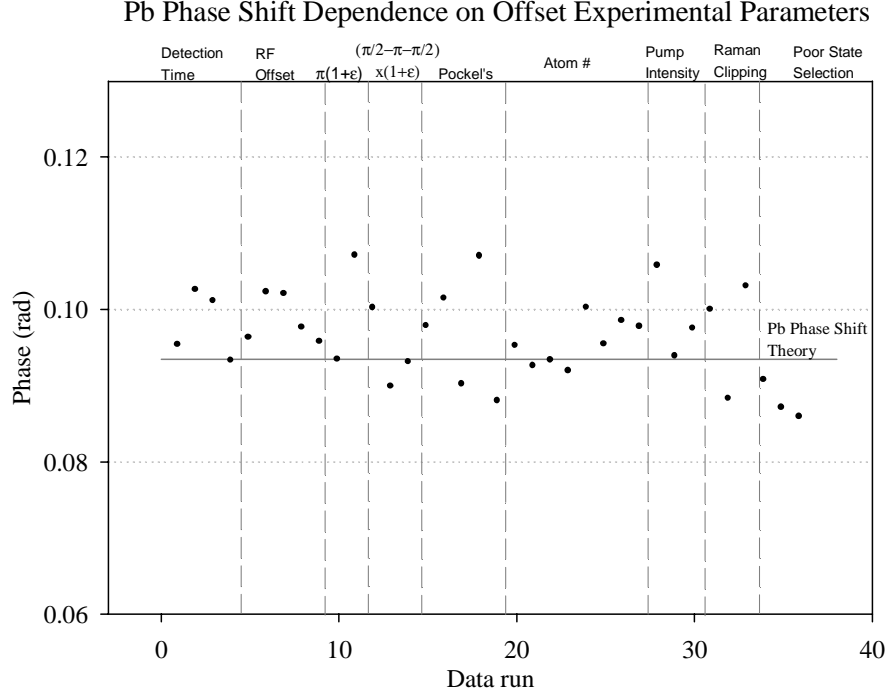


Figure 8.12: Test of varying interferometer parameters on the Pb induced gravity gradient signal. Each point is a single data run. Parameter detunings included the time of detection, Raman 2-photon detuning, inefficient Raman pulse areas, off-axis light contamination, variation in trapped atom number, and inefficient  $m_f = 0$  state selection.

and to test for any bias introduced into the analysis.

The data sets were analyzed by looking at both the consecutive source mass position interferometer phase shifts and by collecting the results into bins based on position. The results were statistically consistent. Figure 8.6 contains a plot of all differential phase shifts for the first data run. A spectral analysis of the chop by chop data did not show any evidence of high or low frequency noise in the data above the background. Presence of a low frequency component would imply the presence of a systematic drift. Furthermore, the data is normally distributed, consistent with Gaussian statistics, Figure 8.13.

We varied the amount of data filtered by varying what was defined to be an acceptable fringe contrast level and outlying fit phase (e.g.  $2\sigma$ ,  $3\sigma$ , etc... ). We found

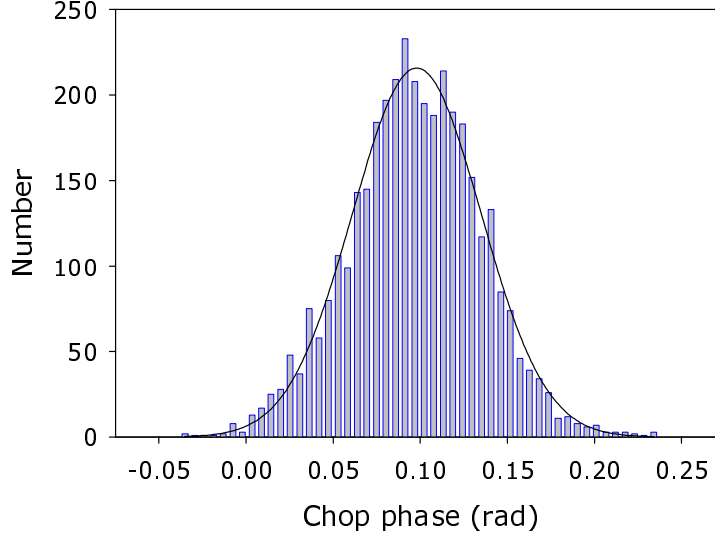


Figure 8.13: Histogram of data run number 1 of the individual source mass differential phase shifts. The solid line is a Gaussian fit to the distribution. The histogram is formed from 3657 Pb phase shifts divided into 50 bins.

that for both the 54 data sets of run 1 and 39 data sets of run 2, the mean phase agreed within the statistics.

We also studied the effect of the scaling parameters used within the normalized detection scheme (Chapter 6) to look for any bias. These normalization coefficients reflect the detection efficiency. They also reflect the efficiency of successive detection of  $F=4$  atoms, between the two detection pulses, and the efficiency of detecting atoms in the  $F=3$  state in the second pulse. These values are not continuously measured but only determined periodically. Detection laser powers were periodically adjusted to optimize the detected atom number and the signal to noise ratio, which may result in a slight change of the normalization coefficients,  $\alpha_{L,U}$ . The normalized  $|4,0\rangle$  population is given by  $S_1/(S_1 - \alpha_{L,U} S_2)$ , with  $S_{1,2}$  proportional to the  $|4,0\rangle$  and  $|4,0\rangle - |3,0\rangle$  signal, respectively. A blind analysis was performed on both data runs over the 2-d parameter space, where each parameter is for a given interferometer detector. Figure 8.14 lists a cross section of the results. The resultant phase shifts had no

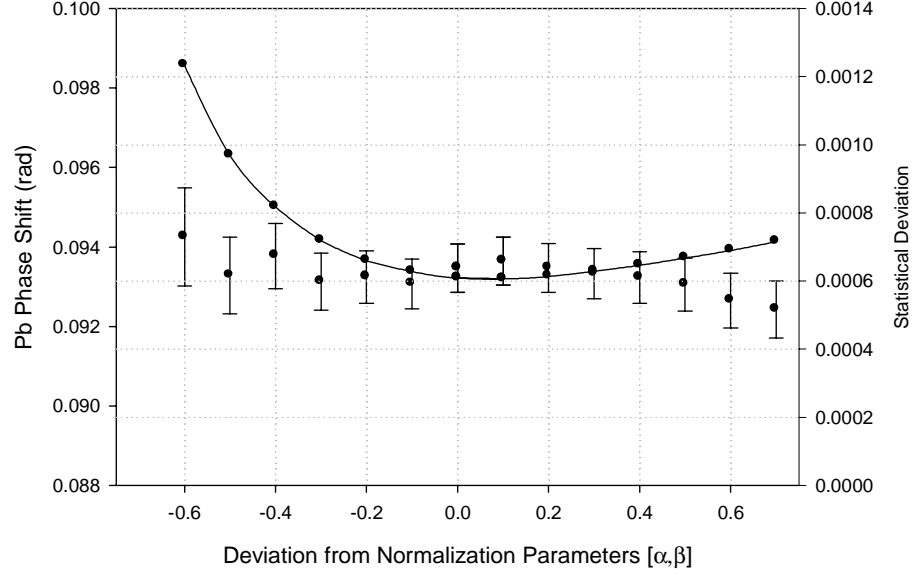


Figure 8.14: Cross section profile of a blind analysis of the second data run as a function of the detection parameters for the two interferometers. The left axis represents the fit phase results over the data run while the right axis represents the weighted fit uncertainty, denoted by the line.

discernable dependence on the fit parameters beyond the statistics. The uncertainties demonstrated a dependence on the normalization parameters, where the data became noisier for large detection parameter deviations (i.e. poor normalization). A global minimum occurred around the system parameters used over the period of the two data runs.

#### 8.4.10 Deviation from Quadratic Lagrangian

Plane waves and a quadratic Lagrangian are assumed in the path integral approach in determining  $\phi_{path}$ <sup>7</sup>. However, the Pb potential

$$U_z = -G \frac{dm}{\phi} = -2\pi G \rho \int_{H_1-z(t)}^{H_2-z(t)} \int_{R_1}^{R_2} \frac{z(t)}{\sqrt{z^2 + r^2}} dz dr, \quad (8.10)$$

<sup>7</sup>The effect on  $\phi_{sep}$  is negligible since the spread of gaussian wavefunctions on the scale of the separation distance at time 2T approximates a plane wave very well.

contains terms higher than quadratic in a Taylor expansion. Numerical solution of the time-dependent Schroedinger equation over the interferometer would be sufficient, however it is also computationally intractable. Some approximations can be made. For sufficiently slow variations of the potential over the atomic wave packet, the above path integral approach remains valid [35, 65].

To determine at what level the theory deviates we evolved a Gaussian wavepacket propagating in an exaggerated, stronger potential, at a period of the trajectory closest to the source mass potential, and on an exaggerated shorter time scale using the split-operator technique of [66]<sup>8</sup>. This technique computes the evolution of a wavefunction after interaction with series of potentials using a fast Fourier transform (fft) technique. Since this approach may prove useful for future examination of deviations from quadratic Lagrangians in the path integral formalism, below is an outline of the split-operator method.

In the split-operator solution of the time-dependent Schroedinger equation, the normal propagator:

$$e^{-i(\frac{\hat{p}^2}{2m}+V(x))\Delta t} , \quad (8.11)$$

is replaced by

$$e^{-i(\frac{\hat{p}^2\Delta t}{4m})}e^{-iV(x)\Delta t}e^{-i(\frac{\hat{p}^2\Delta t}{4m})} . \quad (8.12)$$

This is an approximation because  $V(x)$  and  $\hat{p}$  do not commute. The error is  $O((\Delta t)^3)$  and is sufficient for small  $\Delta t$ . The wavefunction at time  $\Delta t$  later is therefore approximated by:

$$|\Psi(\Delta t)\rangle \approx e^{-i(\frac{\hat{p}^2\Delta t}{4m})}e^{-iV(x)\Delta t}e^{-i(\frac{\hat{p}^2\Delta t}{4m})}|\Psi(0)\rangle . \quad (8.13)$$

As usual, this is evaluated from right to left on the input wave function. The first

---

<sup>8</sup>Full analysis with the real potential and Earth's gravity in real time was numerically too intensive.

operation is performed by transforming to the momentum-space representation by using the fft:

$$|\Phi(p)\rangle = \frac{1}{\sqrt{2\pi}} \int_{-\infty}^{+\infty} |\Psi(x)\rangle e^{-ipx} dx , \quad (8.14)$$

and then acting from the left by the first momentum operator. To evaluate the next term, which is a function of position through the potential, the inverse fft is first performed to transform back to position-space and is then operated on from the left by the potential propagator,

$$e^{-iV(x)\Delta t} |\Psi'(x)\rangle = \frac{1}{\sqrt{2\pi}} e^{-iV(x)\Delta t} \int_{-\infty}^{+\infty} e^{\frac{-ip^2\Delta t}{4m}} |\Phi(p)\rangle e^{ipx} dp . \quad (8.15)$$

This technique is repeated by performing a fft into momentum-space on the resulting wavefunction and acting on the left by the last momentum propagator, giving a wavefunction in momentum-space that is now propagated by  $\Delta t$ . For some time  $T$  later, this is repeated  $N$  times for sufficiently small incremental steps,  $T=N\Delta t$ .

A program such as Matlab is suitable for performing the above numerical calculation. However, as mentioned, the problem is too numerically intensive to follow the propagation of a wavefunction with our gravitational potentials over the 300ms interferometer. Using the above approximations, the split-operator calculations imply that the path integral theory for a single wavepacket path will deviate by less than 0.04% from the quantum propagation, a scale our experiment cannot resolve. Effects are further suppressed since the two wave-packets follow similar, roughly symmetric trajectories and we operate as a gradiometer.

#### 8.4.11 Systematics Results

The results of the experiments listed above that observed a dependence on environmental or operational parameters are listed in Table 8.1, resulting in a systematic

Systematic	$\delta G/G$
Initial Atom Velocity	$1.88 \times 10^{-3}$
Initial Atom Position	$1.85 \times 10^{-3}$
Pb Magnetic Field Gradients	$1.00 \times 10^{-3}$
Rotations	$0.98 \times 10^{-3}$
Source Positioning	$0.82 \times 10^{-3}$
Source Mass Density	$0.36 \times 10^{-3}$
Source Mass Dimensions	$0.34 \times 10^{-3}$
Gravimeter Separation	$0.19 \times 10^{-3}$
Source Mass Density Inhomogeneity	$0.16 \times 10^{-3}$
TOTAL	$3.15 \times 10^{-3}$

Table 8.1: Uncertainty Limits.

uncertainty of 3ppt ( $(6.693 \pm 0.021) \times 10^{-11} \text{m}^3/(\text{kg} \cdot \text{s}^2)$ ). The limiting systematics were dominated by knowledge of the ensemble position and velocity, which could be reduced with better optical access to the chamber. A next generation precision measurement will require further investigation into the possible systematic sources presented in this work.

## 8.5 Conclusion

In conclusion, we have demonstrated a proof of principle measurement of the Newtonian gravitational constant with a value of  $G = (6.693 \pm 0.027 \pm 0.021) \times 10^{-11} \text{ m}^3/\text{kg} \cdot \text{s}^2$  (4ppt statistics and 3ppt systematics, respectively), based on atom interferometric measurement of gravitational induced phase shifts in a fountain of Cs atoms. Our technique for measuring the gravitational constant differs considerably from previous measurements of  $G$  in that we use atoms as the test mass and the measurement is based upon a quantum mechanical interaction. This technique provides a measurement of  $G$  not subjected to the known and hidden systematics of prior measurements. Proven modifications incorporated into a next generation

experiment can increase the gravitational sensitivity while dramatically reducing the known systematics reported above.

Existing optical access to the atoms in the vacuum chamber limited our distance and velocity measurements. An all quartz or zerodur chamber, for example, would provide ample imaging access to the atoms and eliminate susceptibility to eddy currents. Furthermore, an extension of the interferometer pulse sequence would increase the sensitivity of the gradiometer. For instance, a 10-fold increase in sensitivity would be achieved with a  $T = 475\text{ms}$  interferometer using the  $\pi - \pi/2 - \pi$  sequence. A similar enhancement could be obtained with multiple pulse sequences where a  $\pi$ -pulse is replaced by  $(2n+1)$ -multiple  $\pi$ -pulses of alternating propagation direction to achieve  $(4n+2)\hbar k$  momentum transfer [67]. An enhanced experiment could also substitute tungsten for Pb, increasing the atomic phase shift by a factor of 1.7. An extension of the state preparation to select  $m_f = \pm 3$  atoms will allow exploration of spin dependence on  $G$  manifested as a spin-gravity,  $\sigma \cdot \mathbf{g}$ , coupling. The above techniques are already proven and in combination would make an atom interferometer based  $G$  measurement competitive with current state of the art experiments [11–15].



# Chapter 9

## Horizontal ( $T_{x,z}$ ) Gradiometer

This chapter details the demonstration of an atom interferometer based horizontal gravity gradiometer measuring the  $T_{z,x}$  component of the gravitational gradient tensor. The horizontal configuration is maximally sensitive to angular accelerations of the platform. A proof of principle angular acceleration sensitivity of  $6.6 \times 10^{-5} \frac{\text{rad}}{\text{s}^2} / \sqrt{Hz}$  is observed for a  $T = 15\text{ms}$  interferometer time. Measurement statistics were limited by structurally dependent non-common vibration induced phase noise. With increased structural engineering, it is possible to extend the interferometer time and sensitivity to achieve  $10^{-8} \frac{\text{rad}}{\text{s}^2} / \sqrt{Hz}$  angular acceleration sensitivity levels. In an integrated comparison, the atom interferometer gyroscope [68] has a short term sensitivity of  $6 \times 10^{-10} \frac{\text{rad}}{\text{s}} / \sqrt{Hz}$ . A  $T_{z,x}$  has the potential to aid in inertial navigation, especially on the long term time scale where the atomic gyroscope suffers from drift.

### 9.1 Horizontal Gradiometry

The off-axis vertical components of the gravity gradient tensor contribute information about the spatial change of the vertical component of the gravity field. The

measurement axis is along the vertical, and pitch rate of the platform will appear as a differential vertical acceleration between the two interferometers. Effectively, the  $T_{z,x}$  configuration is a gyroscope sensitive to rotations about the horizontal.

### 9.1.1 Setup

The experimental setup is similar to that of the vertical gravity gradiometer, with the main differences in the interferometer layout and interferometer laser propagation. The interferometer light was used in a racetrack configuration through the chambers, routed by two penta-prisms and a cornercube retroreflector. The penta-prisms altered the path of the Raman laser light while ensuring the input and output light remain perpendicular when the prisms are tilted. Any tilt of the prism does not deviate the output beam angle greater than 3 arcminutes. This helps to maintain collinearity of the Raman light. Tilts of the optical table will result in a small change in the Raman path length, negligible compared to the 4.5m effective path length, and Raman position, also negligible as compared to the Raman beam waist.

The penta-prisms were antireflection coated with a  $\lambda/10$  surface quality. They were rigidly coupled together and to the optical table with aluminum extrusion framing. If the prisms are not well coupled then they may exhibit different vibrations from noise on the optics platform. Differential accelerations of the penta-prism pair creates differential Doppler shifts between the two interferometers. This results in a non-common phase noise that can not be rejected through common effects on the interferometer fringes. This prism acceleration noise was the dominant noise source in our experiment and was sensitive to the amount of cross structural support and coupling. We operated with a 79ms, 3.0 cm atomic fountain height to increase the detection signal, compensating for a slight loss when the detection system was realigned in the horizontal gradiometer setup. Operation past  $T = 70$ ms proved to be

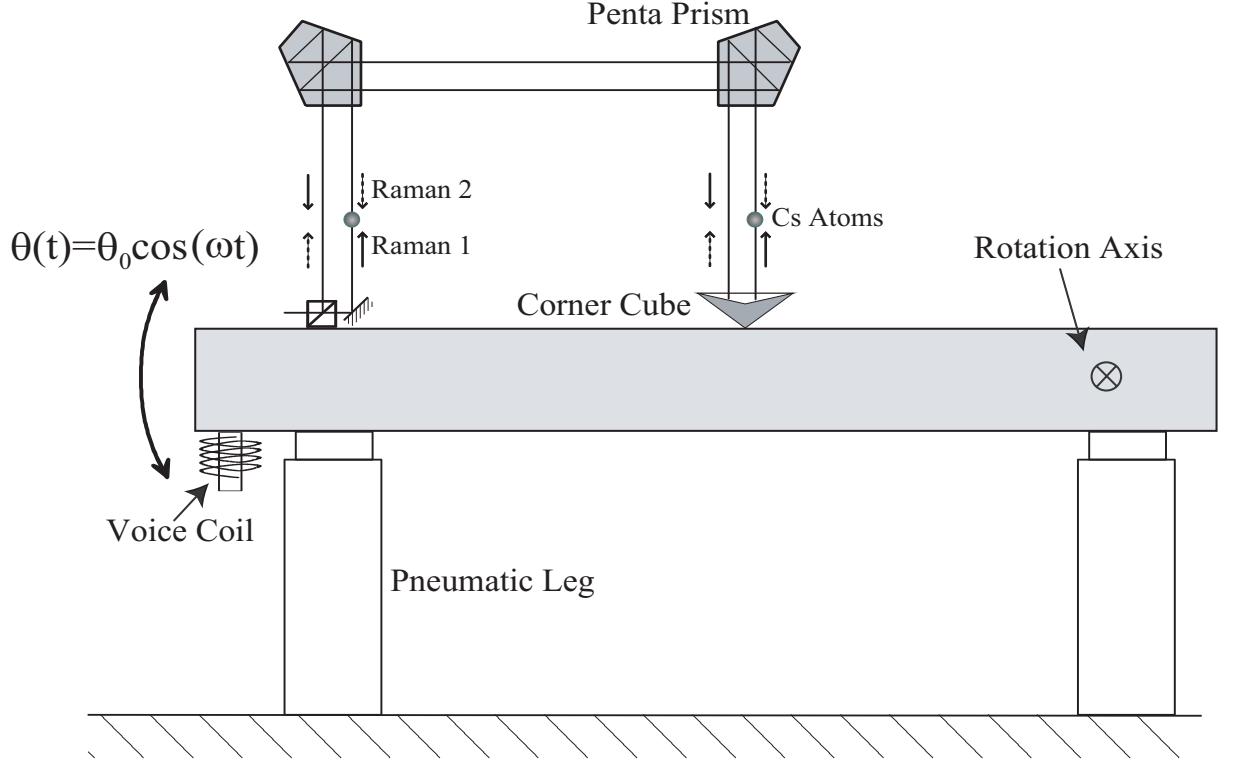


Figure 9.1: Schematic diagram of the configuration used in the horizontal,  $T_{x,z}$  gravity gradiometer. The reference platform was pneumatically supported and actuated with a sinusoidally driven voice coil. The Raman interferometer light propagated along a racetrack design comprised of penta prisms to change the propagation direction by  $90^\circ$ .

difficult due to the amount of non-common acceleration noise.

Accelerometers (Teledyne) were rigidly placed above each penta prism to monitor the differential acceleration during the rotational tests. Each accelerometer has a sensitivity of  $2 \times 10^{-6} m/s^2$  over a 100 Hz bandwidth. We observed a maximal differential signal of  $4.58 \times 10^{-4} m/s^2$  for an induced  $1.69 \times 10^{-5} rad$  tilt over 1Hz. This value is consistent with a “lever arm” inertial effect describing the differential accelerations,  $\dot{\Omega}$ , experienced by two accelerometers separated by a distance,  $R$

$$a = R\dot{\Omega} . \quad (9.1)$$

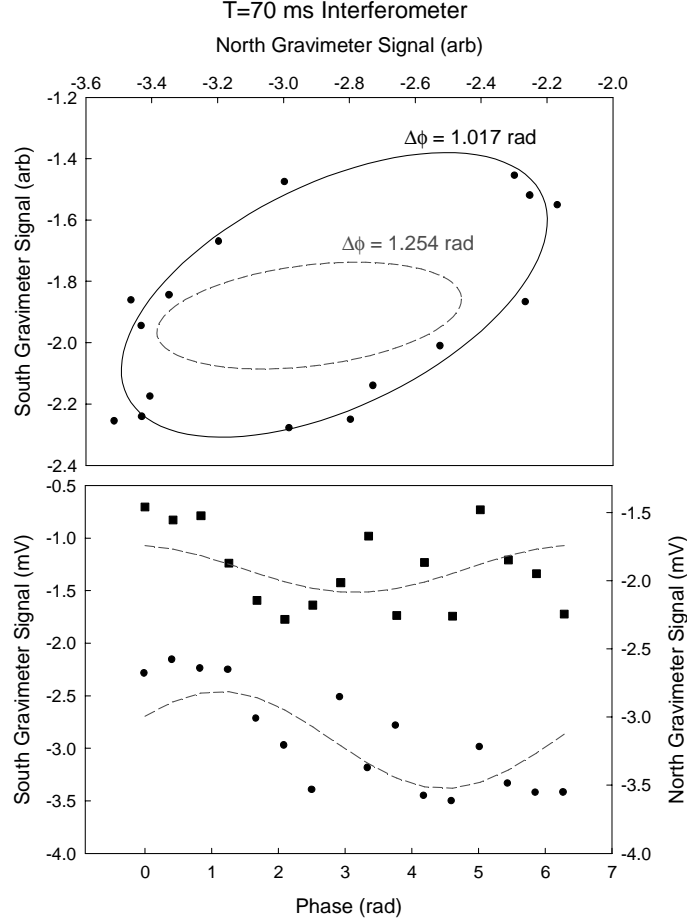


Figure 9.2: Typical 70 ms interferometer fringes in the horizontal gradiometer. Common-mode vibration noise is still evident and eliminated with ellipse fitting. However, the non-common vibration noise is fairly large. To guide the eye, the two fringes were least-squares fit with sinusoidal functions.

This confirmed the source of the non-common phase noise to originate from weak structural cross-coupling of the penta-prism optics.

A voice coil actuated the reference platform with a sinusoidal motion,  $\theta = \theta_0 \cos(\omega t)$ . The rotational acceleration is given by

$$a_r = R \frac{d^2\theta}{dt^2} , \quad (9.2)$$

with  $R$  the relative distance between the two interferometers. The voice coil was

driven by an HP current source (Agilent E3640A) slaved to a function generator. The function generator was triggered to the start of the atom loading cycle, with a period commensurate to the cycle time. A (Applied Geomechanics Series 755-1129) tilt sensor ( $1\mu\text{rad}$  sensitivity) was used to calibrate the tilt range. With an interferometer time of 15ms between pulses the peak of the start of the sinusoidal drive coincided 0.74 radians from the interferometer sequence. Tilt rates of up to  $33\mu\text{rad}/\text{s}$  were applied.

The relative phase shift of the current gradiometer configuration for the Earth vertical-horizontal gradient is practically a null signal, not permitting use of ellipse-specific fitting for our noise levels<sup>1</sup>. A magnetic bias field was applied to one gravimeter during the interferometer sequence. The magnetic field was applied 1ms after the start of the interferometer and lasted for a duration of 16.667ms (1PLC). This creates a relative phase shift through the second order Zeeman effect, allowing ellipse-specific fitting and analysis of the gravimeter signals. In the tilt experiments, an approximate 2 radian phase shift was applied. This permitted ellipse fitting of the data to reject common mode vibration noise.

Angular acceleration induced phase shifts for the above operating conditions are shown in Figure 9.4. A rotational angular sensitivity of  $6.6 \times 10^{-5} \frac{\text{rad}}{\text{s}^2} / \sqrt{\text{Hz}}$  for the 15ms interferometer was observed. This value falls within 8% of the observed phase shift for up to  $248\mu\text{rad}/\text{s}^2$ . Excluding the last point, the agreement is within 3% for up to  $187\mu\text{rad}/\text{s}^2$ . At this level, it is possible that the optics table began exhibiting oscillations of multiple frequency from the drive signal, increasing the amount of non-common vibration noise, such that it became difficult to obtain an accurate ellipse fit of the data. This may also introduce a systematic gravity gradient phase shift.

---

<sup>1</sup>A Txx configuration with similar baseline to that used in the Tzz configuration would give a phase shift of  $\Delta\Phi_{xx} = \Delta\Phi_{zz}/2 \sim 750\text{ mrad}$ , measurable with ellipse fitting.

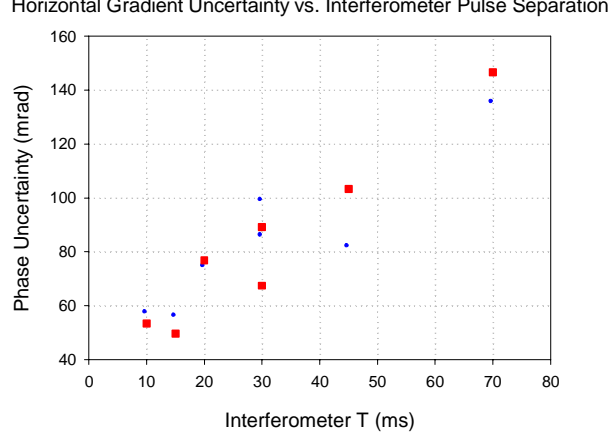


Figure 9.3: Phase uncertainty scaling with interferometer time,  $T$ , shown for the two “positive” and “negative” propagations of the Raman wavevector, denoted by circles and squares respectively.

The observed phase shifts are too large to have originated from Coriolis or centrifugal effects. Centrifugal effects scale as  $\omega^2$  and are expected to enter at the  $10^{-6}$  radian level. Coriolis effects are proportional to both  $\omega$  and the relative transverse velocity of the atoms in the fountain. For our experimental parameters, a maximal coriolis phase shift would enter at approximately  $8 \times 10^{-4}$  radians. This is still at least 3 orders of magnitude smaller than the observed tilt rate signals.

Generalizations to longer interferometer times are permissible. With greater structural rigidity, it is possible to operate with a  $T=150$  ms interferometer time. Assuming a tilt rate response observed above with the same noise level, we would expect a sensitivity of  $\sigma_{150ms} = 6.6 \times 10^{-8} \frac{rad}{s^2} / \sqrt{Hz}$ . With the noise scaling as  $T^2$ , the rotational sensitivity at  $T=150ms$  would be  $\sigma_{150ms} = 3.3 \times 10^{-7} \frac{rad}{s^2} / \sqrt{Hz}$ .

Horizontal configurations of gradiometers have the potential to aid in inertial navigation. The horizontal gradiometer could be used as the equivalent of a gyroscope with potential high long term sensitivity. Previous work demonstrated a sensitivity to signal contrast as a function of tilt rate for a vertical gravity gradiometer configuration. Differential Coriolis phase shifts in such an environment affect the accuracy

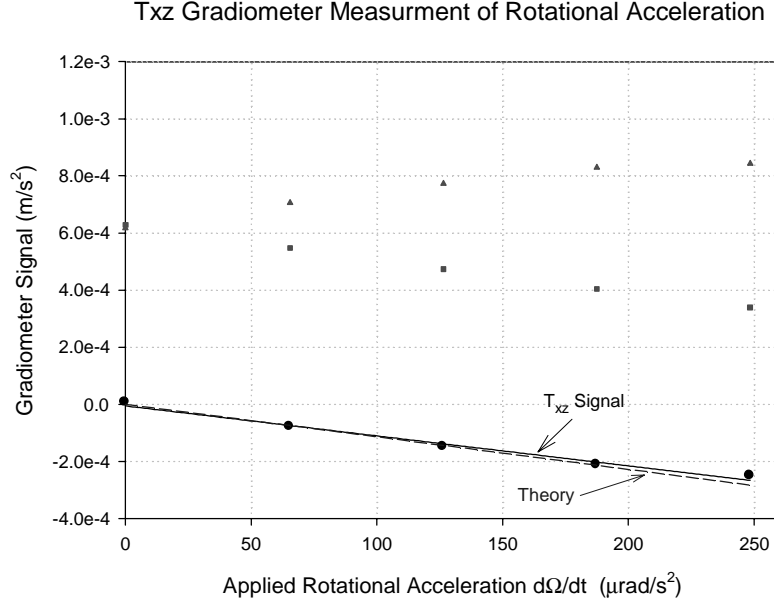


Figure 9.4: Sensitivity to rotations. The square and circle represent different Raman k-vector propagations, respectively. Subtraction of the two signals reveals inertial dependent phase shifts, diamond. Summation produces non-inertial induced phase shifts, such as the applied magnetic bias field over one of the gravimeters, diamond.

of the device. A solution would utilize a configuration of a vertical and horizontal gradiometer system, sharing a common gravimeter chamber and interferometer light.

# Chapter 10

## Conclusion

### 10.1 Summary

We have developed a gravity gradiometer with demonstrated sensitivity to the on-axis vertical component of the gravity gradient tensor and an off-axis  $\{z,j\}$  component as well. The instrument is capable of a vertical sensitivity of  $4 \times 10^{-9} \text{g}/\sqrt{Hz}$  over a baseline of 1.35m and a rotational sensitivity of  $13.7 \times 10^{-6} \text{rad/s}/\sqrt{Hz}$  with a 1m horizontal baseline. An accuracy of 0.65E was determined from a precision measurement of the Newtonian gravitational constant at 4 parts per thousand:  $6.693 \pm 0.027 \times 10^{-11} \text{m}^3/\text{kg} \cdot \text{s}^2$ .

Our detection system was improved using a balanced detection between the atomic hyperfine groundstates, allowing rejection of background vapor atoms and technical noise on the detection light, and a modulation transfer spectroscopy, allowing sensitivity to only a cold velocity class of atoms. Atomic shot-noise (quantum projection) limited detection was observed using this technique. A signal to noise ratio in excess of 2000:1 was observed on our laser cooled atoms. Insensitivity to vibrational induced phase noise was employed with a robust technique in paramet-



rically analyzing the interferometer fringes.

## 10.2 Future Improvements

The demonstrated sensitivity level of the vertical gravity gradiometer can be improved through a number of techniques. With atom shot-noise limited detection, adding more atoms to the fountain will increase the gradiometer signal and thus will directly enhance of the sensitivity. Optical pumping schemes and multiple pulse sequences, both for microwave and velocity selective transitions, offer promising enhancement to the number of atoms entering the interferometer. Improving the laser cooling of the atoms would improve the interferometer fringe contrast. Currently, our contrast is limited due to imperfect Rabi transitions caused by the finite temperature of the atoms and the current Raman beam waist. Insensitivity to spatial inhomogeneities in the Rabi frequency can be achieved by using a combination of composite microwave state selection and composite Raman transitions within the interferometer sequence.

Enhancements in the interferometer pulse sequence in the form of additional Raman  $\pi$  pulses would lead to a direct increase to the gradient sensitivity. For example, an interferometer with  $6\hbar k$  momentum separation was demonstrated by inserting 3 optical  $\pi$  pulses, of alternating propagation direction, near the top of the fountain [67]. This resulted in a factor of 3 increase in the phase sensitivity.

## 10.3 Future Measurements

A gradiometer of our demonstrated sensitivity, utilizing possible improvements listed above, is suited for a number of precision measurement experiments. A new preci-

sion measurement of Newton’s constant could be performed with at least an order of magnitude increase in sensitivity. This could be accomplished by using a multiple and composite pulse sequence beginning with a larger source of atoms in the MOT, coupled with a larger fountain height and a denser source mass. With these improvements, at least an order of magnitude, if not more, can be obtained, thereby becoming a precision  $G$  measurement comparable to recent state of the art torsion balance measurements.

An experiment is currently under development to use our gradiometer technique to measure the gravitational phase shift difference between two atomic species, rubidium and cesium, coexisting in the same interferometer setup. This precision measurement will be a test of the weak equivalence principle of gravity.

## 10.4 Next Generation

A next generation atom interferometer gravity gradiometer is currently under development. This instrument will be capable of measuring simultaneously, or near simultaneously, a number of components of the gradient tensor. This instrument is based on an all optical chamber of Zerodur. The baselines of the gradiometer instrument will be machined out of one chamber, creating a monolithic device. Existing electronics for laser and RF control are being incorporated into a miniaturized portable form factor. This instrumentation and new chamber is already near completion and it’s robustness was initially characterized through the creation of both a 3-D conventional MOT and a 2-D MOT [69, 70].

The above instrument will find a number of uses in the measuring terrain gravity gradient signals in search for geological deposits and features. Such an instrument would be an aid to inertial navigation.

# Appendix A

## Cs Properties

Listed below is a table of cesium values commonly used in the experiment.

Quantity	Symbol	Value (SI)	Ref
Atomic Number	Z	55	
Atomic Mass	m	132.905 451 931 (27) u	[71]
Nuclear Spin	I	$2.206\,946\,50\,(17)\times 10^{-25}\text{kg}$ 7/2	
Frequency	$\omega$	$2\pi \cdot 351.725\,718\,50(11)\text{THz}$	[64]
Wavelength	$\lambda$	852.347 275 82(27)nm	[72]
Lifetime	$\tau$	30.517(57)ns	
Natural Line Width	$\Gamma$	$2\pi \cdot 5.2152(98)\text{MHz}$	
Hyperfine Frequency	$\omega_{hf}$	9.192 631 770GHz (exact)	
Doppler Temperature	$T_D$	124.39 $\mu\text{K}$	[29]
Doppler Velocity	$v_D$	8.82 cm/s	
Recoil Temperature	$T_{rec}$	198 nK	
Recoil Velocity	$v_r$	3.5225mm/s	
Recoil Doppler Shift	$\Delta\omega_{dr}$	$2\pi \cdot 4.1372\text{kHz}$	
Scattering Cross Section	$\sigma_{ge}$	$346.876 \times 10^{-15}\text{m}^2$	
Saturation Intensity	$I_{sat}$	1.10 mW/cm <sup>2</sup>	

Table A.1: Table of Cesium properties. All values are quoted for the D<sub>2</sub> transition,  $6^2\text{S}_{1/2} \rightarrow 6^2\text{P}_{3/2}$ , on the cooling line  $F=4 \rightarrow F'=5$ . Quantities in parentheses represent uncertainty in the last digit. The two photon Raman recoil frequency and velocity are increased by a factor of 2 from the above.

# Appendix B

## Optics Layout and Laser Frequencies

Below is the level diagram of the laser frequencies used in our gravity gradiometer. Depicted also is the schematic arrangement of the laser-optical components used in generating and delivering the laser light in our experiment.

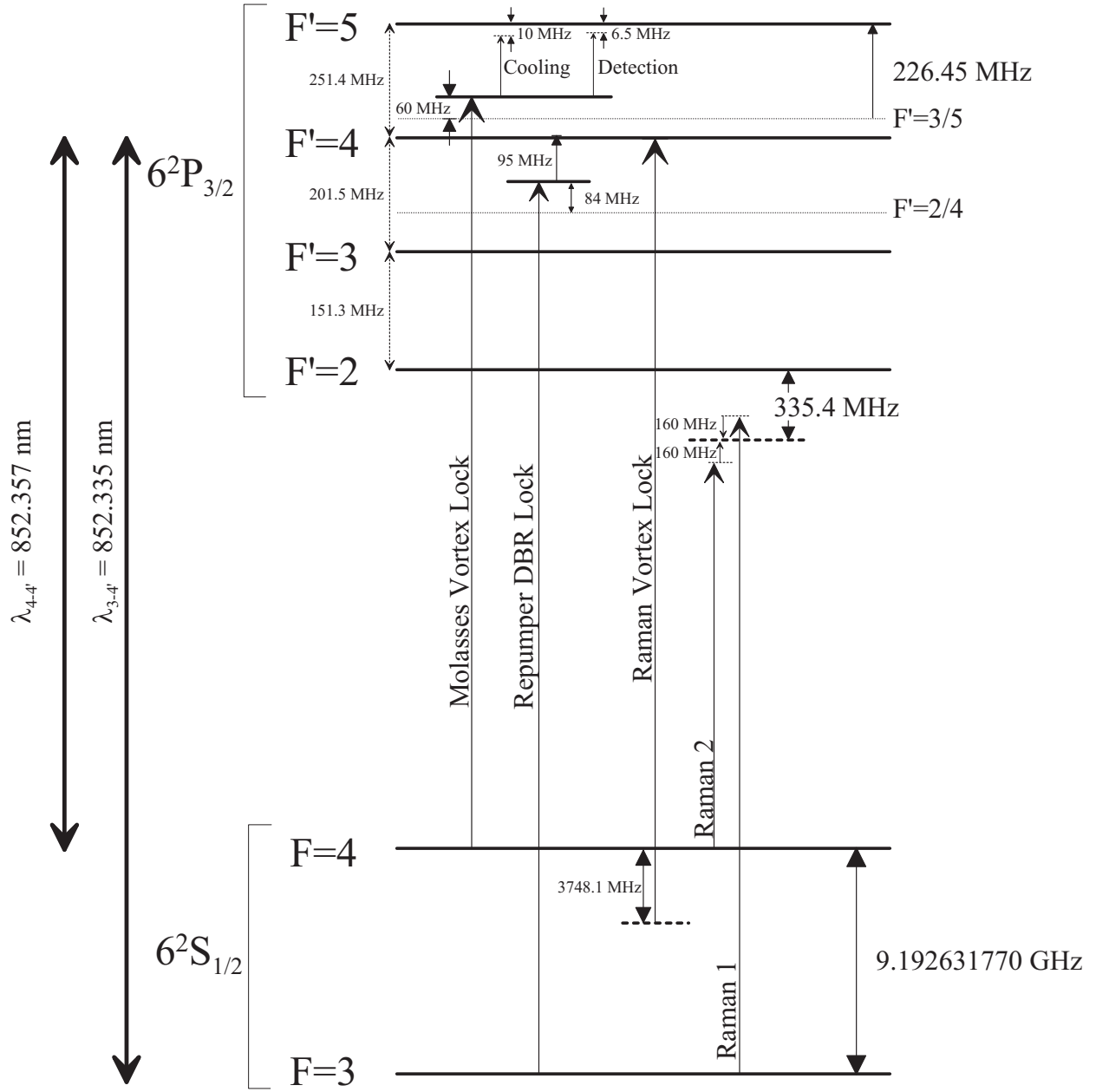


Figure B.1: Cs D2 level diagram and frequency detunings used within the gradiometer apparatus.

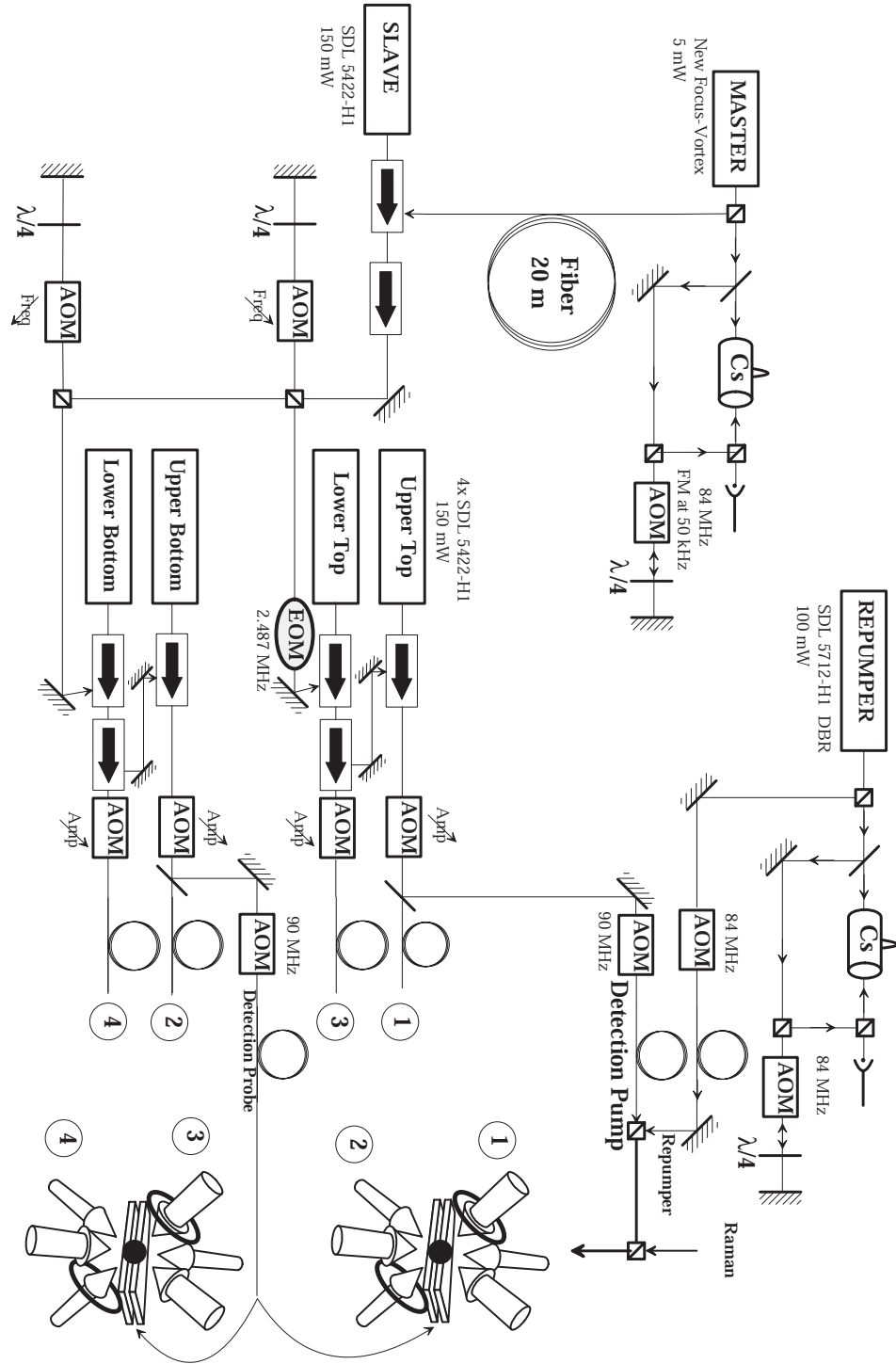


Figure B.2: Laser cooling, repumper, and detection optics layout. All light is fiber coupled to the experiment. Acousto-optic modulator (AOM), electro-optic modulator (EOM), cesium cell (Cs).

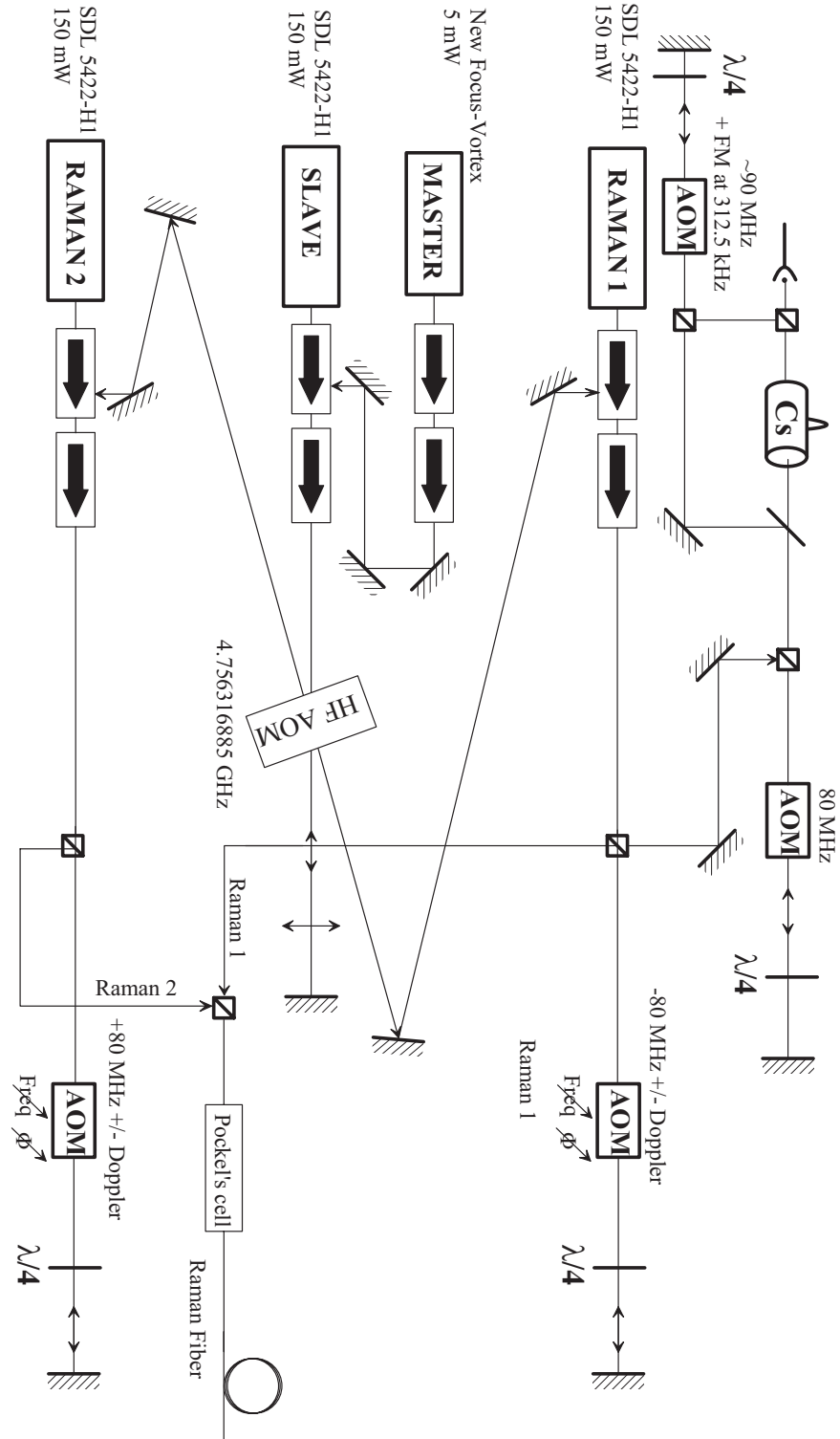


Figure B.3: Raman optics layout. The two Raman frequencies are overlapped, sent through a Pockel's cell, then fiber coupled to the gradiometer. Acousto-optic modulator (AOM), high frequency AOM (HF AOM), cesium cell (Cs).

# Bibliography

- [1] J. Dalibard and W. Phillips. “Stability and damping of radiation pressure traps.”. *Bull. Am. Phys. Soc.*, 30:748, 1985.
- [2] S. Chu, L. Hollberg, J. Bjorkholm, A. Cable, and A. Ashkin. “Three-dimensional viscous confinement and cooling of atoms by resonance radiation pressure.”. *Phys. Rev. Lett.*, 55:48, 1985.
- [3] P.D. Lett, R.N. Watts, C.E. Tanner, S.L. Rolston, W.D. Phillips, and C.I. Westbrook. “Optical Mollases.”. *J. Opt. Am. Soc. B*, 6:2084–2107, 1989.
- [4] A. Peters, K.Y. Chung, and S. Chu. “High-precision gravity measurements using atom interferometry”. *Metrologia*, 38:25–61, 2001.
- [5] J.M. McGuirk, G.T. Foster, J.B. Fixler, M.J. Snadden, and M.A. Kasevich. “Sensitive absolute-gravity gradiometry using atom interferometry”. *Phys. Rev. A*, 65:033608, 2002.
- [6] T.L. Gustavson, P. Bouyer, and M.A. Kasevich. “Precision rotation measurements with an atom interferometer gyroscope”. *Phys. Rev. Lett.*, 78:2046–49, 1997.
- [7] J.M. Hensley. “*A precision measurement of the fine structure constant*”. PhD thesis, Stanford University, Stanford, 2001.



- [8] Mark Helm Dransfield. “*Airborne Gravity Gradiometry*”. PhD thesis, The University of Western Australia, 1994.
- [9] Christopher Jekeli. *Inertial Navigation Systems with Geodetic Applications*. Walter de Gruyter, New York, 2000.
- [10] A.J. Romaides, J.C. Battis, R.W. Sands, A. Zorn, D.O. Benson Jr, and D.J. DiFrancesco. “A comparison of gravimetric techniques for measuring subsurface void signals”. *J. Phys. D: Appl. Phys.*, 34:433–443, 2001.
- [11] P.J. Mohr and B.N. Taylor. “CODATA recommended values of the fundamental physical constants: 1998”. *Rev. Mod. Phys.*, 72:351–495, 2000.
- [12] U. Kleinevoss, H. Meyer, A. Schumacher, and S. Hartmann. “Absolute measurement of the Newtonian force and a determination of  $G$ ”. *Meas. Sci. Technol.*, 10:492–494, 1999.
- [13] F Nolting, J Schurr, St Schlamming, and W. Kündig. “A value for  $G$  from beam-balance experiments”. *Meas. Sci. Technol.*, 10:487–491, 1999.
- [14] J.P. Schwarz, D.S. Robertson, T.M. Niebauer, and J.E. Faller. “A new determination of the Newtonian constant of gravity using the free fall method”. *Meas. Sci. Technol.*, 10:478–486, 1999.
- [15] C.V. Boys. “On the Newtonian constant of gravitation”. *Phil. Trans. R. Soc.*, 186:1–72, 1895.
- [16] J.H. Gundlach and S.M. Merkowitz. “Measurement of Newton’s constant using a torsion balance with angular acceleration feedback”. *Phys. Rev. Lett.*, 85:2869–72, 2000.

- [17] T.J. Quinn, C.C. Speake, S.J. Richman, R.S. Davis, and A. Picard. “A new determination of  $G$  using two methods”. *Phys. Rev. Lett.*, 87:111101, 2001.
- [18] W. Michaelis, H. Haars, and R. Augustin. “A new precise determination of Newton’s gravitational constant”. *Metrologia*, 32:267–76, 1996.
- [19] K. Kazuaki. “Anelasticity in  $G$  experiments”. *Meas. Sci. Technol.*, 10:435–438, 1999.
- [20] Wicht A, Hensley JM, Sarajlic E, and Chu S. “A preliminary measurement of the fine structure constant based on atom interferometry”. *Physica Scripta*, T102:82–88, 2002.
- [21] C. Jekeli. “A review of gravity gradiometer survey system data analyses”. *Geophys.*, 58:508–514, 1993.
- [22] J. M. McGuirk. “*High precision absolute gravity gradiometry with atom interferometry*”. PhD thesis, Stanford University, Stanford, 2001.
- [23] E. van Leeuwen. “BHP develops airborne gravity gradiometer for mineral exploration”. *Leading Edge*, 19:1296–1297, 2000.
- [24] M. Ryan. “Memphis uses gravity to reach new navigational heights”. *Undersea Warfare*, 1:22–22, 1998.
- [25] Moody M V, Chan H A, and Paik H J. “Superconducting gravity gradiometer for space and terrestrial applications”. *J. Appl. Phys.*, 60:4308–4315, 1986.
- [26] Moody M V and Paik H J. “Gauss law test of gravity at short-range”. *Phys. Rev. Lett.*, 70:1195–1198, 1993.

- [27] T.M. Niebauer, G.S. Sasagawa, J.E. Faller, R. Hilt, and F. Klopping. “A portable apparatus for absolute measurement of the Earth’s gravity”. *Metrologia*, 32:159–180, 1995.
- [28] J.M. Brown, T.M. Niebauer, F.J. Klopping, and A.T. Herring. “A new fiberoptic gradiometer for 4-D absolute differential gravity”. *Geophysical Research Letters*, 27:33–36, 2000.
- [29] C.S. Adams and E. Riis. “Laser cooling and trapping of neutral atoms”. *Prog. Quant. Electr.*, 21:1–79, 1997.
- [30] H.J Metcalf and P. van der Straten. *Laser Cooling and Trapping*. Springer-Verlag, New York, 1999.
- [31] J. Dalibard and C. Cohen-Tannoudji. “Laser cooling below the Doppler limit by polarization gradients - simple theoretical methods”. *Prog. Quant. Electr.*, 6:2023–2045, 1989.
- [32] J.M. McGuirk, G.T. Foster, J.B. Fixler, and M.A. Kasevich. “Low-noise detection of ultracold atoms”. *Opt. Lett.*, 26:364–366, 2001.
- [33] *edited by* P. Berman. *Atom Interferometry*. Academic Press, New York, 1996.
- [34] K. Bongs, R. Launay, and M.A. Kasevich. “High-order inertial phase shifts for time-domain atom interferometers”. <http://xxx.lanl.gov>, *Submitted to Phys. Rev. A*, pages quant-ph/0204102, 2002.
- [35] P. Storey and C. Cohen-Tannoudji. “The Feynman path integral approach to atomic interferometry - A tutorial”. *Journal de Physique II*, 4:1999–2027, 1994.

- [36] M. Kasevich, D.S. Weiss, E. Riis, K. Moller, S. Kasapi, and S. Chu. “Atomic velocity selection using stimulated Raman transitions”. *Phys. Rev. Lett.*, 66:2297, 1991.
- [37] P. Bouyer, T.L. Gustavson, K.G. Haritos, and M.A. Kasevich. “Microwave signal generation with optical injection locking”. *Opt. Lett.*, 21:1502–1504, 1996.
- [38] R.P. Feynman and A.R. Hibbs. *Quantum Mechanics and Path Integrals*. McGraw-Hill Higher Education, 1965.
- [39] M.J. Snadden, J.M. McGuirk, P. Bouyer, K.G. Haritos, and M.A. Kasevich. “Measurement of the Earth’s gravity gradient with an atom interferometer-based gravity gradiometer”. *Phys. Rev. Lett.*, 81:971–974, 1998.
- [40] J.P. Bouyer. “Spectral stabilization of an InGaAsP semiconductor-laser by injection-locking”. *Annales de Physique*, 18:89–239, 1993.
- [41] L. Goldberg, H.F. Taylor, A. Dandridge, J.F. Weller, and R.O. Miles. “Spectral characteristics of semiconductor lasers with optical feedback”. *IEEE Journal of Quantum Electronics*, QE-18:555–563, 1982.
- [42] G.K. Woodgate. *Elementary atomic structure*. Oxford, 1980.
- [43] M.H. Levitt. “Composite pulses”. *Prog. NMR Spect.*, 18:61–122, 1986.
- [44] A.Peters, J.M. Hensley, and S. Chu. “Active low frequency vibration isolation”. *Rev. Sci. Instr.*, 70:2735–2741, 1999.
- [45] G. Santarelli, P. Laurent, and P. Lemonde *et al.* “Quantum projection noise in an atomic fountain: a high stability cesium frequency standard”. *Phys. Rev. Lett.*, 82:4619–22, 1999.

- [46] J.H. Shirley. “Modulation transfer processes in optical heterodyne saturation spectroscopy”. *Opt. Lett.*, 7:537–539, 1982.
- [47] J.J. Synder, R.K. Raj, D. Bloch, and M. Ducloy. “High-sensitivity non-linear spectroscopy using a frequency-offset pump”. *Opt. Lett.*, 5:163–5, 1980.
- [48] A. Fitzgibbon, M. Pilu, and R. Fisher. “Direct least squares fitting of ellipses”. *IEEE Transactions On Pattern Analysis and Machine Intelligence*, 21:476–480, 1999.
- [49] W. Gander, G. Golub, and R. Strebel. “Least-squares fitting of circles and ellipses”. *BIT*, 34:558–578, 1994.
- [50] J.D. Prestage, R.L. Tjoelker, and L Maleki. “Atomic clocks and variation of the fine-structure constant”. *Phys. Rev. Lett.*, 74:3511–3514, 1995.
- [51] D.S. Weiss, B.C. Young, and S. Chu. “Precision-measurement of the photon recoil of an atom using atomic interferometry”. *Phys. Rev. Lett.*, 70:2706–2709, 1995.
- [52] P.R. Bevington and D.K. Robinson. *Data Reduction and Error Analysis for the Physical Sciences*. McGraw-Hill Science, 2002.
- [53] S.J. Richman, T.J. Quinn, C.C. Speake, and R.S. Davis. “Preliminary determination of G using the BIPM torsion balance.”. *Meas. Sci. and Tech.*, 10:460–466, 1999.
- [54] M.P. Fitzgerald and T.R. Armstrong. “The measurement of G using the MFS torsion balance”. *Meas. Sci. and Tech.*, 10:439–444, 1999.
- [55] J. Luo, Z.K. Hu, X.H. Fu, S.H. Fan, and M.X. Tang. “Determination of the

- Newtonian gravitational constant  $G$  with a nonlinear fitting method”. *Phys. Rev. D*, 59:042001, 1999.
- [56] O.V. Karagioz and V.P. Izmailov. “Measurement of the gravitational constant with a torsion balance.”. *Meas. Tech.*, 39:979–987, 1996.
- [57] C.H. Bagley and G.G. Luther. “Preliminary results of a determination of the Newtonian constant of gravitation: A test of the Kuroda hypothesis.”. *Phys. Rev. Lett.*, 78:3047–3050, 1997.
- [58] D.W. Allan. “Time and frequency (time-domain) characterization, estimation, and prediction of precision clocks and oscillators”. *IEEE Trans. Ultrasonics Ferr. and Freq. Control*, 34:647–654, 1987.
- [59] J. Vanier and C. Audoin. *The Quantum Physics of Atomic Frequency Standards*. Adam Hilger Ltd., Bristol, 1989.
- [60] M.A. Kasevich. “*Atom Interferometry in an Atomic Fountain*”. PhD thesis, Stanford University, Stanford, 1992.
- [61] K. Gibble and S. Chu. “Laser-cooled Cs frequency standard and a measurement of the frequency-shift due to ultracold collisions”. *Phys. Rev. Lett.*, 70:1771–1774, 1993.
- [62] C. Fertig and K. Gibble. “Measurement and cancellation of the cold collision frequency shift in an Rb-87 fountain clock ”. *Phys. Rev. Lett.*, 85:1622–1625, 2000.
- [63] A. Peters. “*High precision gravity measurements using atom interferometry*”. PhD thesis, Stanford University, Stanford, 1998.

- [64] Th. Udem, J. Reichert, T.W. Hänsch, and M. Kourogi. “Absolute optical frequency measurement of the cesium D<sub>2</sub> line”. *Phys. Rev. A*, 62:031801, 2000.
- [65] E.J. Heller. “Time dependent approach to semiclassical dynamics”. *J. Chem. Phys.*, 62:1544–1555, 1975.
- [66] M.D. Feit, J.A. Fleck Jr., and A. Steiger. “Solution of the Schrodinger-equation by a spectral method”. *J. Comput. Phys.*, 47:412–433, 1982.
- [67] J.M. McGuirk, M.J. Snadden, and M.A. Kasevich. “Large area light-pulse atom interferometry”. *Phys. Rev. Lett.*, 85:4498–4501, 2000.
- [68] T. L. Gustavson. “*Precision rotation sensing using atom interferometry*”. PhD thesis, Stanford University, Stanford, 2000.
- [69] K. Dieckmann, R.J.C. Spreeuw, M. Weidemuller, and J.T.M Walraven. “Two-dimensional magneto-optical trap as a source of slow atoms”. *Phys. Rev. A*, 59:3891–3895, 1998.
- [70] J. Schoser, A. Batar, R. Low, V. Schweikhard, A. Grabowski, Yu. B. Ovchinnikov, and T. Pfau. “Intense source of cold Rb atoms from a pure two-dimensional magneto-optical trap”. *Phys. Rev. A*, 66:023410, 2002.
- [71] M.P. Bradley, J.V. Porto, S. Rainville, J.K. Thompson, and D.E. Pritchard. “Penning trap measurements of the masses of <sup>133</sup>Cs, <sup>87,85</sup>Rb, and <sup>23</sup>Na with uncertainties  $\leq 0.2$  ppb”. *Phys. Rev. Lett.*, 83:4510–4513, 1999.
- [72] L. Young, W.T. Hill III, S.J. Sibener, S.D. Price, C.E. Tanner, C.E. Wieman, and S.R. Leone. “Precision lifetime measurements of Cs 6p<sup>2</sup>P<sub>1/2</sub> and 6p<sup>2</sup>P<sub>3/2</sub> levels by single-photon counting”. *Phys. Rev. A*, 50:2174–2181, 1994.